U.PORTO

FEUP FACULDADE DE ENGENHARIA
UNIVERSIDADE DO PORTO

Fatigue behaviour of cold-rolled profiles

Simulation and characterization studies

Maria João Marques Correia

Dissertation submitted to
Faculdade de Engenharia da Universidade do Porto
for the degree of:

Mestre em Engenharia Mecânica

Supervisor:
Prof. Abílio de Jesus

Co-supervisors:
Eng. Vitor Gomes
Dr. José Correia

Departamento de Engenharia Mecânica
Faculdade de Engenharia da Universidade do Porto

Porto, 2019

The work presented in this dissertation was performed at the
Department of Mechanical Engineering
Faculty of Engineering
University of Porto
Porto, Portugal.

Maria João Marques Correia
E-mail: em11076@fe.up.pt

Faculdade de Engenharia da Universidade do Porto
Departamento de Engenharia Mecânica
Rua Dr. Roberto Frias s/n
4200-465 Porto
Portugal

Abstract

Cold roll forming is a widely used manufacturing process that allows the production of profiles with various sections in an array of materials. Thin-walled cold formed products obtained through this process are commonly used in the Logistic Industry in Racking & Shelving Systems where they are used as rails for the passage of shuttles. Residual stresses induced during the manufacturing process when combined with service loading stresses, consequence of the shuttle movement, can affect fatigue life of these profiles. FASTCOLD is an European project that aims to solve a lack of design rules at an European level referring to cold rolled formed steel members. The objective of this dissertation, that is included in the FASTCOLD project, is to analyse the stresses induced by roll forming and the effect of external cyclic loads on fatigue life of these components.

Experimental work was done to study the mechanical and geometrical characteristics of a Z-section rail profile. In order to know the mechanical properties of the profiles produced through the cold roll forming process, tensile tests and microstructure analysis were performed. Contact and optical methodologies were adopted to analyse the three-dimensional deffects on Z-section profiles induced by the manufacturing process.

Finite Element Analysis was performed using COPRA® FEA RF software with the aim of studying the residual stresses and three-dimensional defects induced on the material during the roll forming process. A local stress-based approach was used to estimate fatigue life of the Z-section profile when subjected to cyclic loading. The results obtained in the simulations performed were compared to previous simulations executed in the scope of the FASTCOLD project in order to understand the effects of using kinematic hardening instead of isotropic hardening in the results.

Numerical and experimental results of this study demonstrate the existence of three-dimensional geometric defects on roll-formed profiles such as edge waviness, bow and twist. Tensile tests performed revealed material anisotropy. Analysis to the microstructure of material samples showed that the surface of outer corner regions may present poor quality after the manufacturing process. The fatigue analysis identified the corner regions as the critical areas where fatigue cracks tend to nucleate, something already verified by preliminary experimental tests performed on the rail profiles by partners of the FASTCOLD project. Furthermore, results show that the use of a kinematic hardening rule instead of an isotropic hardening rule does not have significant impact on the residual stresses induced by the roll forming simulation. However, geometry features such as springback are influenced by this parameter. Fatigue life prediction using kinematic hardening led to higher values of maximum loads allowed for the same number o cycles. The results of experimental tests performed revealed that the numerical analyis tends to overestimate the geometry distortions of the profile.

Keywords: Cold Roll Forming, Fatigue Analysis, FEA, Residual Stresses, Three-dimensional Defects, FASTCOLD

Resumo

Perfilagem a frio é um processo de produção vastamente usado que permite a criação de perfis com variadas secções num diverso leque de materiais. Perfis de espessura de parede fina obtidos através deste processo de produção são comummente usados como carris para passagem de vagões de transporte de cargas na Indústria da Logística em sistemas de armazenamento conhecidos como *Racking & Shelving*. As tensões residuais induzidas durante o processo de produção quando combinadas com tensões induzidas pelas cargas cíclicas externas de serviço, resultantes do movimento dos vagões, podem afetar a vida à fadiga destes perfis. O projeto Europeu FASTCOLD tem como objetivo suprimir a lacuna de informação e de normas europeias para projeto à fadiga destas estruturas. O objetivo desta dissertação, que está incluída no projeto FASTCOLD, é analisar as tensões induzidas durante a perfilagem a frio dos perfis e o efeito das cargas cíclicas externas na vida à fadiga destes componentes.

Ensaios experimentais foram realizados com o propósito de analisar as propriedades mecânicas e as características geométricas do perfil em Z. De forma a determinar as propriedades mecânicas, foram realizados testes à tração e análises à microestrutura em provetes extraídos de um perfil produzido pelo processo de perfilagem a frio. Metodologias de medição por contacto e ótica foram usadas para caracterizar a geometria do perfil e analisar os defeitos tridimensionais induzidos pelo processo de produção.

Uma análise usando o Método dos Elementos Finitos foi feita usando o *software* COPRA® FEA RF com o objetivo de estudar as tensões residuais e os defeitos tridimensionais induzidos no material durante o processo de produção. Uma abordagem que tem como base as tensões locais foi usada para estimar o número de ciclos até à rutura da estrutura quando submetida a cargas cíclicas externas. Os resultados obtidos nas simulações foram comparados com resultados obtidos anteriormente em simulações realizadas no âmbito do projeto FASTCOLD a fim de determinar o impacto da escolha da regra de endurecimento (cinemático ou isotrópico) nos resultados finais obtidos.

Os resultados experimentais e numéricos demonstraram a existência de defeitos geométricos tridimensionais derivados do processo de perfilagem. Testes à tração realizados em amostras retiradas do perfil tornaram evidente a anisotropia do material. O estudo da microestrutura do aço S355MC mostrou que a superfície exterior na região dos cantos apresenta baixa qualidade após o processo de perfilagem. A análise á fadiga permitiu identificar os raios como as zonas críticas onde se podem formar as fendas de fadiga, algo já verificado por testes experimentais preliminares levados a cabo por parceiros do projeto FASTCOLD. Conclui-se ainda que o uso de endurecimento cinemático em vez de endurecimento isotrópico não tem impacto significativo nas tensões residuais induzidas pelo processo de produção. No entanto, a geometria do perfil, nomeadamente no que toca ao retorno elástico, é influenciada pela escolha da regra de endurecimento. O estudo de vida à fadiga do perfil quando usado o endurecimento cinemático, prevê uma maior carga para o mesmo número de ciclos quando se compara com os resultados obtidos usando endurecimento isotrópico. A realização de testes experimentais permitiu concluir que a

simulação numérica faz uma sobre-estimativa das distorções geométricos da estrutura.

Keywords: Conformação a frio, Perfilagem a frio, Análise à fadiga, Tensões residuais, Defeitos tridimensionais

'You cannot hope to build a better world without improving the individuals. To that end, each of us must work for our own improvement and, at the same time, share a general responsibility for all humanity, our particular duty being to aid those to whom we think can be most useful.'

Marie Curie

Acknowledgements

I would like to thank Professor Abílio de Jesus for allowing me to be part of this project, for the availability demonstrated and the support provided thoughout its course.

I would also like to thank Vitor Gomes for the support and patience demonstrated throughout the entire semester and for always being available to clarify any doubts or helping me decide the best direction for this project.

The European Comission, through the Research Fund for Coal & Steel is acknowledged and in particular the project FASTCOLD.

I would like to thank DataM for providing the software necessary to develop the present work.

Finally, I would like to thank my parents and my sister for their support and for believing in me and my abilities and for encouraging me to pursue new challenges.

Contents

Abstract i

resumo ii

Acknowledgements vii

1 Introduction 1
- 1.1 Background . . . 1
- 1.2 FASTCOLD . . . 2
- 1.3 Objectives of the dissertation . . . 3
- 1.4 Planning and Methodology . . . 4
- 1.5 Layout of the dissertation . . . 4

2 Literature Review 7
- 2.1 Roll Forming . . . 7
  - 2.1.1 Deformation modes . . . 8
  - 2.1.2 Causes of redundant deformations . . . 10
  - 2.1.3 Effects of redundant deformations on product defects . . . 12
- 2.2 Residual Stresses . . . 16
- 2.3 Fatigue analysis . . . 18
  - 2.3.1 Definitions . . . 18
  - 2.3.2 Fatigue analysis of cold formed steel profiles . . . 23
- 2.4 Finite element method analysis . . . 25
- 2.5 Previous FASTCOLD research . . . 26

3 Z-Profile characterization 29
- 3.1 Z-section profile . . . 29
- 3.2 Mechanical properties . . . 31
  - 3.2.1 Tensile tests . . . 31
  - 3.2.2 Material microstructure analysis . . . 37
- 3.3 Geometrical Analysis . . . 42
  - 3.3.1 LVDT Analysis . . . 42
  - 3.3.2 GOM Analysis . . . 48

4 COPRA FEA Simulations 53
- 4.1 Model definition . . . 53
  - 4.1.1 Modelling concepts . . . 53
  - 4.1.2 Geometry and flower . . . 53
  - 4.1.3 Boundary conditions . . . 54
  - 4.1.4 Element type . . . 56

4.1.5 Mesh definition 56
4.1.6 Material model 57
4.2 Measurement of residual stresses along xx direction 57
4.2.1 Measurement of bow and springback 59
4.3 Analysis of the effect of kinematic hardening 59
4.3.1 Simulation results and discussion 61
4.3.2 Fatigue analysis of the Z-section profile 69

5 Conclusion **79**
5.1 Conclusions 79
5.2 Future Work 80

References **81**

A Appendix 1 **85**

List of Figures

1.1 R&S systems with shuttle [Aceally, 2018]. 2

2.1 Schematics of the roll forming process [Tsa, 2018]. 8
2.2 Transversal bending of metal strip during roll forming [Halmos, 2006]. . . . 9
2.3 Additive redundant deformations of metal strip during roll forming [Halmos, 2006]. 10
2.4 Mechanism of occurrence of longitudinal bending of metal strip [Halmos, 2006]. 10
2.5 Mechanism of occurrence of longitudinal elongation and shrinkage of metal strip [Halmos, 2006]. 11
2.6 Longitudinal bow and twist of the product [Halmos, 2006]. 13
2.7 Schematic illustration of edge buckling (edge waviness) [Halmos, 2006]. . . 13
2.8 Springback [Abvabi et al., 2015]. 15
2.9 Flare of cutoff ends [Halmos, 2006]. 16
2.10 Fatigue strength curves for direct stress ranges (EN 1993-1-9 2015) 21
2.11 Design process of a roll forming line; in blue is the traditional process of trial and error; in orange, the upgraded process with virtual testing; dashed lines represent the connection between the cycles [Ferreira, 2016]. 26

3.1 Cold rolled rail profile. 29
3.2 Dimensions of the Z-section profile. 30
3.3 Nomenclature used to describe the Z-section profile [Martins, 2018]. 30
3.4 Dimensions and location of longitudinal specimens. 31
3.5 Dimensions and location of transversal specimens. 32
3.6 Machined samples from the Z-section profile on the longitudinal direction (before the tensile test). 32
3.7 Setup for the tensile test. 33
3.8 Specimens after tensile tests. 34
3.9 Results of the tensile tests on the longitudinal (L) and transversal (T) specimens. 34
3.10 Comparison of stress-strain curves between the engineering curve, true curve and Swift's hardening law curve referring to the longitudinal direction. . . . 36
3.11 Comparison of stress-strain curves between the engineering curve, true curve and Swift's hardening law curve referring to the transversal direction. . . . 37
3.12 Locations of the samples cut from the Z-profile for the microstructure analysis. 38
3.13 Images obtained from the microstructure analysis of material from point 2, outer radius region. 38
3.14 Point 2, interior radius: no sign of cracks. 39

3.15 Images obtained from the microstructure analysis of material from exterior radius of points 1, 3 and 4. 40
3.16 Images obtained from the microstructure analysis of material from point 1, 3 and 4: smooth surface appearence. 41
3.17 Sample extracted from point 5 exhibits longitudinal lines hut no visible signs of crack initiation. 42
3.18 Experimental setup and supports used to place the profile. 43
3.19 Paths used in the LVDT analysis. 43
3.20 Experimental setup of shape deffects measurement with a LVDT. 44
3.21 Results with LVDT analsysis for the web using the values measured in paths V1, V2, V3, V4, V5 and V6 (displacements shown in mm). 45
3.22 Results with LVDT analsysis for the small flange using the values measured in paths V7 and V8 (displacements shown in mm). 46
3.23 Results with LVDT analsysis for the large flange using the values measured in paths V9 and V10 (displacements shown in mm). 46
3.24 Comparison of the data points collected from the web region with the LVDT analysis with a plane created through polynomial regression. Deviations from the plane are presented. 47
3.25 Comparison of the data points collected from the small flange with the LVDT analysis with a plane created through polynomial regression. Deviations from the plane are presented. 48
3.26 Comparison of the data points collected from the large flange with the LVDT analysis with a plane created through polynomial regression. Deviations from the plane are presented. 48
3.27 Results of the GOM analsysis, displacements (in mm) in the flanges 49
3.28 Results of the GOM analsysis for the Z rail profile (displacements shown in mm). 50
3.29 Results of the GOM analsysis, small flange with displacements shown in mm. 50
3.30 Results of the GOM analsysis (displacements shown in mm). 51

4.1 Stations and rolls used in the simulation of the Z-section profile [Martins, 2018]. 54
4.2 Flower diagram of the Z-section profile [Martins, 2018]. 54
4.3 Boundary conditions in x and y-directions applied in three nodes in the middle of the tail end of the profile [Martins, 2018]. 55
4.4 Boundary conditions to restrain the nodes in the extremities along z-direction to simulate the continuous existence of the strip [Martins, 2018]. 55
4.5 Boundary conditions related to the free cut process [Martins, 2018]. 56
4.6 Mesh definition of the Z-section profile [Martins, 2018]. 57
4.7 Location of the planes in the profile for residual stresses measurement [Martins, 2018]. 58
4.8 Representation of the top path [Martins, 2018]. 58
4.9 Location of the paths where through thickness residual stresses were measured [Martins, 2018]. 59
4.10 Hardening models. 60
4.11 Bauschinger effect, σ_{Y0}^{T} is the tensile yield stress and σ_{Y0}^{C} is the compressive yield stress [Natal Jorge and Dinis, 2004]. 61
4.12 Comparison of results regarding residual stresses along xx direction in the top (t/2) surface between the 3 paths. 61

4.13 Comparison of results regarding residual stresses along the xx direction in the bottom (-t/2) surface between the 3 paths. 62
4.14 Comparison of results regarding residual stresses along xx direction between the top and bottom surface of path 1. 62
4.15 Comparison of results regarding residual stresses along xx direction for the top surface of path 1 between isotropic and kinematic hardening. 63
4.16 Comparison of results regarding residual stresses along xx direction for the bottom surface of path 1 between isotropic and kinematic hardening. . . . 63
4.17 Comparison of equivalent plastic strain along xx direction between the top and the bottom surface for path 1. 64
4.18 Comparison of equivalent plastic strain along xx direction for the top surface of path 1 between isotropic and kinematic hardening. 64
4.19 Comparison of equivalent plastic strain along xx direction for the top surface of path 1 between isotropic and kinematic hardening. 65
4.20 Through thickness resiual stresses between the 5 paths for plane ii. 65
4.21 Comparison of through thickness residual stresses between isotropic and kinematic hardening for each of the five paths. 66
4.22 Edge position of the large flange for the top surface for both istropic and kinematic hardening. 67
4.23 Edge position of the large flange for the bottom surface for both istropic and kinematic hardening. 67
4.24 Comparison of longitudinal bow measured on the bottom surface of the web between isotropic and kinematic hardening. 68
4.25 Comparison of springback in the large flange between simulations with isotropic and kinematic hardening. 68
4.26 Comparison between COPRA estimation for final geometry of the profile after the roll-forming process and the one verified in the profile samples. . . 69
4.27 Cracks in tested rails initiating in the inner corner regions. 71
4.28 Paths used for fatigue analysis [Martins, 2018]. 71
4.29 Stresses in the inner corner of the Z-section profile for an applied load of 9 kN in the top surface. 72
4.30 Stresses for an applied load of 9 kN in the bottom surface of the Z-section profile. 73
4.31 Comparison of stresses in xx direction for an applied load of 2 kN in the top surface for the critical node between isotropic and kinematic hardening. 74
4.32 Comparison of stresses in xx direction for an applied load of 4,5 kN in the top surface for the critical node between isotropic and kinematic hardening. 74
4.33 Comparison of stresses in xx direction for an applied load of 9 kN in the top surface for the critical node between isotropic and kinematic hardening. 75
4.34 Comparison of stresses in xx direction for an applied load of 2 kN in the bottom surface for the critical node between isotropic and kinematic hardening. 75
4.35 Comparison of stresses in xx direction for an applied load of 4.5 kN in the bottom surface for the critical node between isotropic and kinematic hardening. 76
4.36 Comparison of stresses in xx direction for an applied load of 9 kN in the bottom surface for the critical node between isotropic and kinematic hardening. 76

4.37 Number of cycles for maximum loads of 2 kN, 4,5 kN and 9 kN in a logarithmic scale, for simulations with kinematic hardening. 77
4.38 Number of cycles for maximum loads of 2 kN, 4,5 kN and 9 kN in a logarithmic scale, for simulations with isotropic hardening [Martins, 2018]. . . . 78

List of Tables

1.1 Timeline for execution of tasks. 4

2.1 Cyclic elastoplastic and fatigue properties of S355 structural steel [Jesus et al., 2012] 22
2.2 Klippstein's Fatigue Design Categories [LaBoube and wen Yu, 1999] 24
2.3 Intercept for mean fatigue curves [LaBoube and wen Yu, 1999] 25

3.1 Chemical composition (weight %) of S355MC according to UNI EN 10149-2. 31
3.2 Mechanical properties of S355MC according to UNI EN 10149-2. 31
3.3 Mechanical properties obtained experimentally of the two materials used. . 35
3.4 Swift's Law constants. 36

4.1 Information regarding shuttles and pallets typical masses [Martins, 2018] . . 70
4.2 Estimated number of cycles for three different cyclic loads applied in the top surface of the large flange of the Z-section profile using the local S-N based approach. 76
4.3 Estimated number of cycles for three different cyclic loads applied in the bottom surface of the large flange of the Z-section profile using the local S-N based approach. 77

A.1 Stresses [MPa] along the xx direction of the element coordinate system for the inner corner of the profile. Comparison between the initial state and results (in step 26 and 76) after application of 2 kN, 4,5 kN and 9 kN. . . . 85
A.2 Stresses [MPa] along the xx direction of the element coordinate system for the inner corner of the profile. Comparison between the initial state and results (in step 51 and 100) after application of 2 kN, 4,5 kN and 9 kN. . . 86
A.3 Stresses [MPa] along the xx direction of the element coordinate system for the outter corner of the profile. Comparison between the initial state and results (in step 26 and 76) after application of 2 kN, 4,5 kN and 9 kN. . . . 87
A.4 Stresses [MPa] along the xx direction of the element coordinate system for the outter corner of the profile. Comparison between the initial state and results (in step 51 and 100) after application of 2 kN, 4,5 kN and 9 kN. . . 88

Chapter 1

Introduction

1.1 Background

Cold roll forming is a flexible metal forming process that requires continuous bending of sheet metal using stations with rotating rolls without changing the thickness of the material. There are records of this process being used with silver and gold applications that date back to the fourteenth century. Leonardo da Vinci designed the first known forming mill in 1480. Later, in the eighteenth century, steel firstly started being cold formed which became widely used in the nineteenth century. Materials such as aluminum, copper, titanium and alloys were being cold formed and made commercially available in the late nineteenth century [Halmos, 2006].

Nowadays, cold formed products are used in a variety of applications that range from the automotive sector to airplanes or even furniture and home appliances. Auxiliary operations such as punching, weldind and clenching can be included in this process, resulting in profiles that are ready to use after just one process, making this the main advantage of cold roll forming.

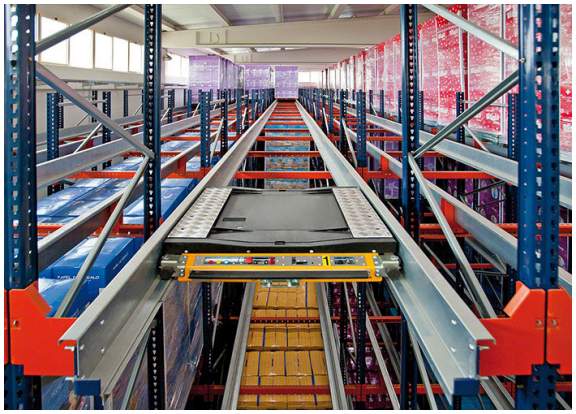
Many industries have become attracted to the flexibility of this process, resulting in higher quality requirements. Tighter material tolerances, increased flexibility and improved efficiency of the process reducing the number of operators and consequently the cost of production are the new chanllenges that this process is facing. All these demands can be successfully accomplished if the proper equipment, the right material, a good design and knowledgeable and motivated workforce are used.

Tool design is another crucial step on the cold roll forming process and computer aided engineering (CAE) has a vital role on this step. There are numerous available softwares that allow the user to design and study the various steps involved in the roll forming process such as designing the roll tool and the flower and decide what the forming sequence should be. COPRA RF is a Data M software that allows the user to develop the whole process chain of roll forming. Flower design, roll tool design, part lists and tool production are just some of the steps that can be studied in this software [DataM, 2018].

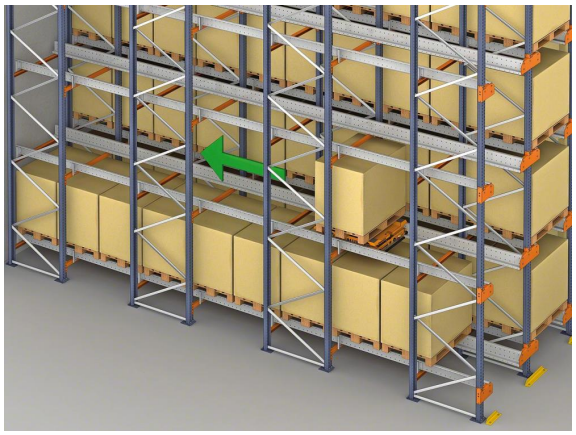
Numerical analysis of the formed products was one of the most important technological advances. Before this, the development of new machines was very dependent on the experience of the developer and frequently resort to trial and error approaches which required the production of rolls, machine setup and ensuing evaluation of the product that could lead to modifications if there were any weaknesses ocurring. This approach was very time-consuming, costly and some times ineffective. DataM also offers a finite element analysis software for roll forming, COPRA FEA RF [DataM, 2018].

One of the most significant applications of cold roll formed products is in racking

and shelving (R&S) systems used in the Logisctics Industry, figures 1.1a and 1.1b show Z-section profiles that support the shuttles. The process allows for the production of thin-walled tailor-made sections that help to reduce the material consumption and to produce light weight and high quality profiles. Every client has specific requirements and logistics concepts for its warehouse, which requires a flexible and always evolving Logistic Industry.



(a) Shuttles used in the racking systems, Z-section profiles where the shuttle travels can be seen.



(b) Racking and Shelving System.

Figure 1.1: R&S systems with shuttle [Aceally, 2018].

1.2 FASTCOLD

FASTCOLD is an European research project that focuses on the study of the FAtigue STrength of COLD-formed structural steel details. Cold formed steel sections are largely used in rack structures of warehouses; they are the most flexible, economic and sustainable option for this kind of application. The Logistic Industry in Europe is fast growing and has a huge importance on the competiveness of the European market. In order to fulfil the customer's demands, the features and sizes of the warehouses are continuously evolving and expanding [FASTCOLD, 2018].

Minimizing the time of sheltering storage goods and transport operations is one of the main concerns in this industry. Management systems and machines used for storage and retrieval (S/R) of goods have to be design to be efficient: the S/R machines are required to work fast and carry higher loads continuously. The changes in the economy led to changes

in the requirements of the warehouses, the steel rack structures are now under dynamic load conditions due to the high amounts of load cycles and dynamic loads that result of the movement of the S/R machines. Due to this repeated dynamic loads, fatigue failure may exist and, in the recent past, fatigue cracks were detected and fatigue failure of rack structures occurred [FASTCOLD, 2018].

On an European level, there are no available design rules that allow for a reliable fatigue assessment of cold formed steel sections. EN 1993-1-3 focuses on cold-formed thin-walled sections but only covers the design under static loads. EN 1993-1-9, covers only the fatigue design of thick-walled hot rolled steel details. This gap of information is becoming problematic for the European rack industries, putting this sector at risk of loosing competitiveness[FASTCOLD, 2018].

FASTCOLD may be considered a "pre-normative" research: although focusing on the problems of the Logistic Industry it will also create technical knowledge related to fatigue design of cold-formed structural steel details. The validity of the EC3-1-9 fatigue design approach will be examined when applied to cold-formed steel. FASTCOLD also aims at creating a classification of cold-formed steel structural details according to their fatigue strength which will be implemented in relevant parts of Eurocodes [FASTCOLD, 2018].

1.3 Objectives of the dissertation

The main purpose of the present work is to understand the impact of the roll forming process in fatigue resistance of cold formed profiles. In order to achieve this goal, several other objectives must be fulfilled:

- Understand the fundamental principles of cold roll forming as a manufacturing process, which means understanding the influence of geometrical and process parameters and material properties on residual stresses and on three-dimensional defects;
- Evaluate the distribution and magnitude of residual stresses in a Z-section profile, especially in corner regions, since these areas tend to present the highest values of residual stresses;
- Identify the critical areas (as far as residual stresses are concerned), as well as evaluate the development of three-dimensional defects and springback;;
- Implement mechanical cyclic loads on a Z rail profile with S350GD steel in the simulation models in order to study the influence of existing residual stresses (due to the roll forming process) combined with cyclic load on the fatigue resistance of the profiles;
- Compare the performance of plasticity models with isotropic and kinematic hardening;
- Characterize the material properties in different areas of the profile in a non-loaded specimen.
- Evaluate alternative techniques for the profile geometric tolerances assessment;
- Evaluate material microstructures after roll forming process of the Z profile made of S355MC steel.

To achieve these goals, experimental tests as well as numerical simulations were performed. From previous numerical simulations executed in the scope of the FASTCOLD Project, experimental tests could be designed taking into account informations already available and the results obtained through the numerical simulations could be compared to the experimental results and validated.

1.4 Planning and Methodology

The planning and methodology adopted for the execution of the project tasks took into consideration the time available for the development of the dissertation and the needs and requirements of the FASTCOLD project.

Table 1.1: Timeline for execution of tasks.

	September	October	November	December	January	February
State of art review						
Software Learning						
Experimental Tests						
Numerical simulations						
MSc dissertation writing and presentation preparations						

1.5 Layout of the dissertation

This dissertation is divided into 5 chapters. The first chapter, where this section is included, presents a brief introduction to the roll forming process and to the FASTCOLD project as well as the objectives and methodology adopted.

The second chapter provides a literature review referring to the roll forming process including typical three-dimensional defects and the prevalence of residual stresses and strains in roll formed products; basic rules for fatigue design of steel members and an introduction to finite element method analysis and its importance in the design of cold formed steel members are also presented.

The third chapter is dedicated to the characterization of the Z-section profile. Experimental tests performed to analyse mechanical and geometrical properties are described and the results are shown and analysed.

In the fourth chapter a comparative analysis is made to understand the effects of kinematic hardening on the numerical study of the cold forming and fatigue life prediction. A comparative analysis is presented for the material S350GD using previous results attained with isotropic hardening.

The final chapter exhibits the relevant conclusions of the study and suggestions for future work.

Chapter 2

Literature Review

In this chapter, an analysis of the available literature regarding roll forming processes will be performed. The main topics presented will be:

- The roll forming process: an introduction to the differents steps of the process in order to better understand the effects of the roll forming on the material. Special attention will be given to deformation modes, defects and residual stresses;
- Fatigue analysis: understand the behaviour of cold formed profiles when subjected to cyclic loads;
- Finite Element Method analysis: how numerical simulations can simplify the study of a process;
- Previous research done in the scope of the FASTCOLD project relevant for the formulation of this report.

2.1 Roll Forming

Cold forming is a metal forming process that happens below the recrystallization temperature [Güner, 2007]. In steels, this process takes place at room temperature. There are two ways of cold forming: press breaking and roll forming. While press breaking is normally used to obtain simple cross sections where the material is pressed and folded until the final section is obtained, the cold forming process resorts to various steps that continuously bend a long strip of metal by using consecutive rolls (figure 2.1) [Lindgren, 2009].

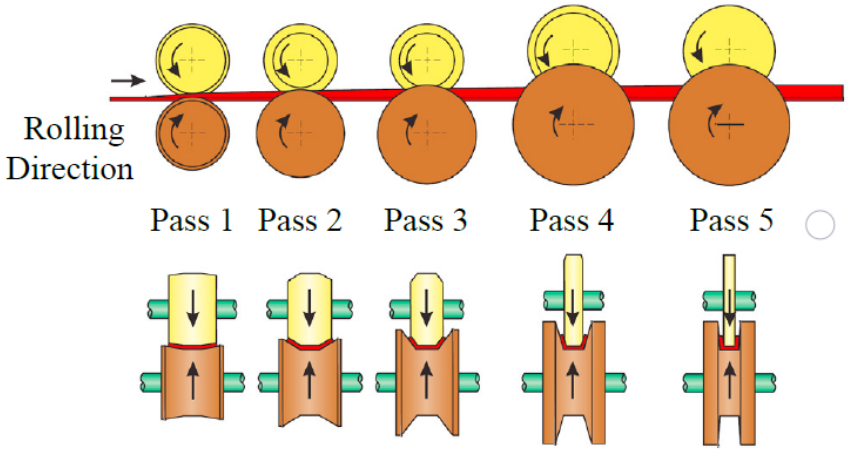


Figure 2.1: Schematics of the roll forming process [Tsa, 2018].

Roll forming is well suited to produce large quantities of constant profile products with a high section complexity [Lindgren, 2009]. The high strength, good dimension accuracy and good surface finish of the final products as well as less material waste are some advantages of this process. On the other hand, high forming loads are required and the ductility and formability of the material at low temperature is limited [Güner, 2007].

When it comes to the materials that can be used in this process, all the materials that can be bent can also be roll-formed. Carbon steel, stainless steel, aluminum and copper are some of the materials suited. Profile steel products can also be obtained from pre-painted or pre-coated as well as uncoated steel sheets attained through hot rolled or cold rolled flat strips or coils. The available machinery and facilities usually limit the thickness and length of the final product (there is no actual limit for the length) however the thickness of the roll formed material usually varies between 0.1 mm and 19 mm [Güner, 2007].

Cold roll forming being a continuous process, allows for high production speeds. The most common range of speed used is 25-30 m/min, but it can go from 0.5 to 240 m/min [Güner, 2007].

Some advantages that can be met when using the cold roll forming process are [Güner, 2007]:

- High speed of production that leads to high production of profiles (1500-1800 m of profile per hour is a common used rate);
- Higher strength to weight ratio (when compared to hot rolled or extruded sections);
- Surface finish of the raw material intact after forming;
- Auxiliary operations (piercing, notching, welding and peforation) can be incorporated in the roll forming process.

2.1.1 Deformation modes

The roll forming process is accomplished through the gradual deformation of a strip that passes between rotating contoured rolls. To obtain the required shape using the least amount of incremental steps is the goal of the designer. If a strip is formed with too few steps, the material will be subjected to an unacceptable level of stress that will result

in distortion. On the other hand, using too many passes will lead to an economically non-viable process.

To avoid deffects on the final product it is important to know and understand the various types of deformation that the material experiences during the process.

Transversal bending

Tranversal bending, as seen in figure 2.2, is a crucial deformation that allows the metal strip to be transformed into the final product with the desired cross-section [Halmos, 2006].

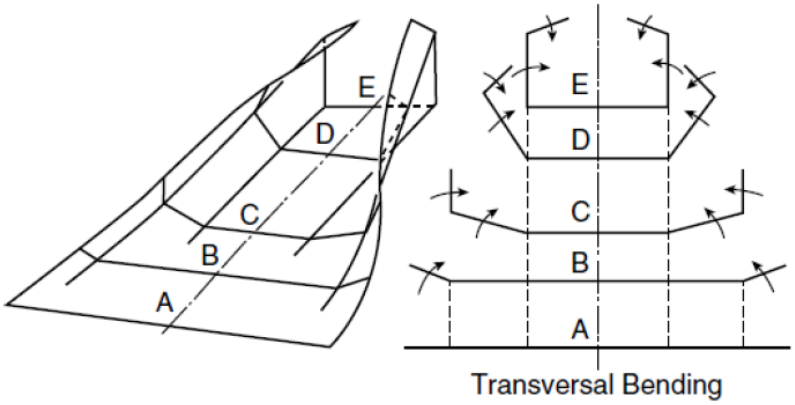


Figure 2.2: Transversal bending of metal strip during roll forming [Halmos, 2006].

Redundant deformations

Given the characteristics of the roll forming process where a metal strip (precut or in coil form) enters the roll forming mill and is gradually deformed into three-dimensional shapes by various contoured rolls, it is inevitable for the material to undergo other deformations besides tranversal bending. This additive redundant deformations are represented in figure 2.3 and are:

- Longitudinal bending and bending back
- Longitudinal elongation and/or shrinkage
- Transversal elongation and/or shrinkage
- Shear in the metal's plane
- Shear in the direction of the metal's thickness
- Different combinations of the above

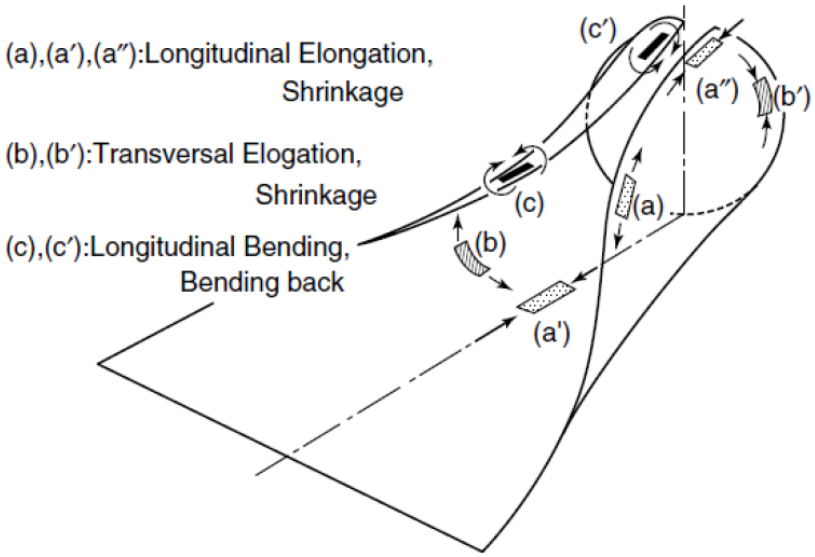


Figure 2.3: Additive redundant deformations of metal strip during roll forming [Halmos, 2006].

These deformations greatly impact the final shape of the product being responsable for many problems that occurr in roll forming processes [Halmos, 2006].

2.1.2 Causes of redundant deformations

Longitudinal bending or bending back

The movement of the metal strip during the cold roll forming process is such that each portion of the strip moves in individual spatial flow lines. Before entering the roll gap, each portion of the strip is bent in the longitudinal direction. When exiting the roll gap or at the center of the roll, the strip portions are bent back to a longitudinal straight shape.

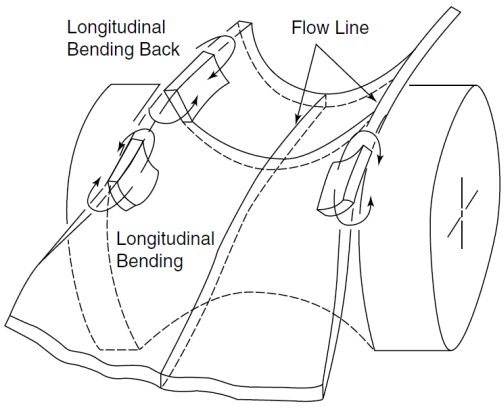


Figure 2.4: Mechanism of occurrence of longitudinal bending of metal strip [Halmos, 2006].

The repeated longitudinal bending and bending back under the longitudinal tensile force is usually particularly high at the edge portion of the strip, as seen in figure 2.4,

which contributes to the longitudinal elongation [Halmos, 2006].

Longitudinal elongation or shrinkage

During the roll forming process, the height of the cross-section of semiformed products increases from the initial height (that is equal to the thickness of the material) to the height of the cross-section in the final product. On the other hand, the width decreases from the initial strip width to the product's cross-section width. The variations of the height and width of the cross-section occurrs because the strip moves and deforms in both vertical and horizontal directions.

While the center part of the strip usually moves in a straight line, the edge portions rise vertically and shift horizontally towards the center of the cross-section. Due to this two way movements, the edge portions usually elongate while the center and intermediate portions shrink in the longitudinal direction. Figure 2.5 represents the mechanism of occurence of longitudinal elongation and shrinkage, the flow line of each portion have different lengths when compared to each other, causing tensile and compressive stresses that lead to material defects.

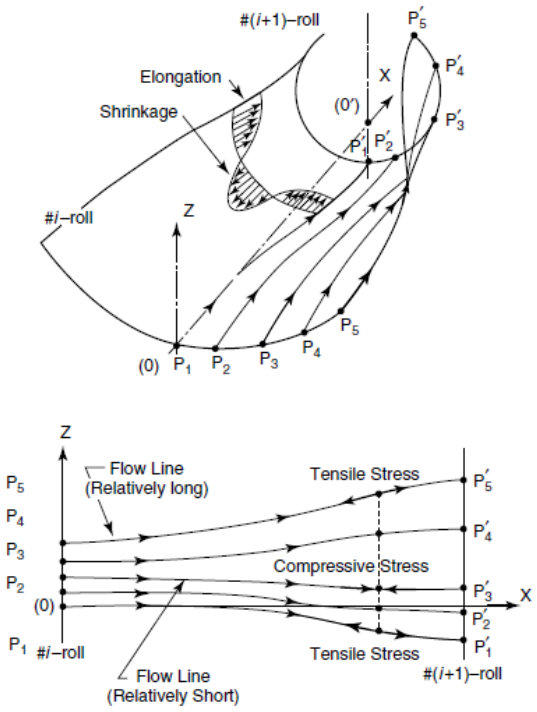


Figure 2.5: Mechanism of occurrence of longitudinal elongation and shrinkage of metal strip [Halmos, 2006].

The technical features of the flow line (such as the length, number of rolls, roll profiles, roll positions and horizontal distance between stands) may cause the opposite effect. The flow line length of the edge portion may be shorter than that of the center part. In that case, the center portion tends to elongate and the edge portion tends to shrink in the longitudinal direction [Halmos, 2006].

Transversal elongation and shear in metal's plane

On products formed from wide metal coils, the edge portions (and intermediate portions on a lesser degree) are pulled towards the center in the transversal direction. Usually this transversal movement originates from the transversal bending of center portions of the coils [Halmos, 2006].

The wider the coils, the larger the force required to pull the edge and intermediate portions toward the center and shift the flat portions in the transversal direction. Due to the large transversal tensile force required, transversal elongation occurs in the strip [Halmos, 2006].

In the bending corners, both transversal and longitudinal elongation may occur if the convex rolls excert excessive force in the inside surface of the strip. This excessive force may alter the thickness of the material and a bulging deformation takes place at the bend lines which leads to appreciable elongation [Halmos, 2006].

The shear deformations that result from the shifts in the transversal direction have a great impact on the shape of the corner (bend line) as well as on the springback deformation of the cutoff end (flare) causing serious deffects on the final product [Halmos, 2006].

2.1.3 Effects of redundant deformations on product defects

All the redundant deformations described above cause various defects in the product, such as: longitudinal bow, edge waviness, flare and dimensional innacuracy. Some of the deffects and their occurrence mechanisms will be presented in the following sections.

Longitudinal bow and twist

The cause for longitudinal bow and twist (figure 2.6) is the nonuniform transversal distribution of the longitudinal membrane strain (longitudinal elongation and shrinkage of the strip). The transversal nonuniformity of the longitudinal membrane strain occurs whenever a flat strip is formed into a cross-section having heights and widths that differ from those of the original flat metal strip, which is inevitable to occur in roll forming [Halmos, 2006].

The magnitude of longitudinal membrane strain can be, nonetheless, reduced if the roll forming conditions are optimized. If the number of passes used is too small, the amount of transversal bending deformation caused by each pair of rolls will likely be excessive. Also, the roll profiles and roll positions can impair the process because if the flow of each portion of the strip is not smooth, the magnitude and nonuniformity of longitudinal membrane strain tend to increase. At last, entry guides and intermediate guides can also be used to minimize the longitudinal membrane strain [Halmos, 2006].

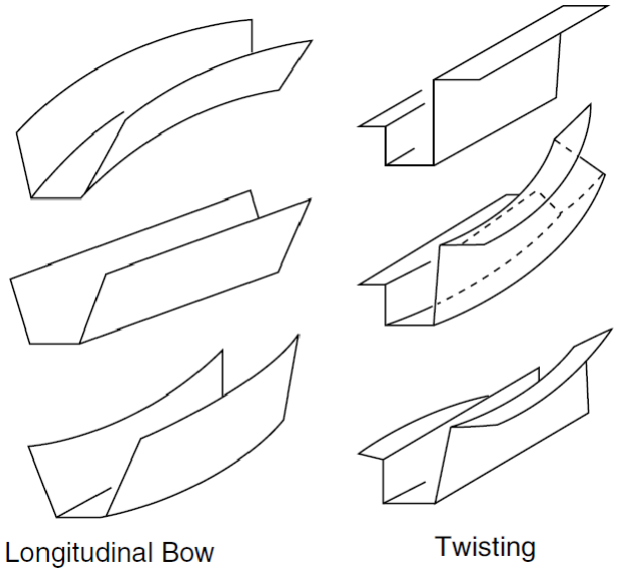


Figure 2.6: Longitudinal bow and twist of the product [Halmos, 2006].

Edge waviness

The edge waviness is caused by elastic or elastoplastic buckling. Due to the simultaneous vertical and horizontal movement of the edge of the strip that takes place in the initial stage of forming, longitudinal elongation occurs. Longitudinal elongation also happens when the edge portion enters the roll gap. However, when the elongated edge portion leaves the roll gap, it has to shrink again in order to mantain the strip straight (for that, each portion of the semi-formed strip has to have the same length). If the edge portion reaches a critical value of elongation, the shrinking process will not be smooth and the edge waviness occurs [Halmos, 2006].

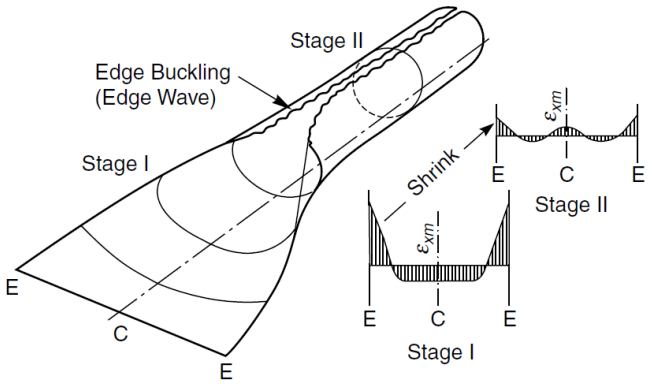


Figure 2.7: Schematic illustration of edge buckling (edge waviness) [Halmos, 2006].

Using a sufficient number of rolls, roll profiles, roll positions, guides and a correct pass line are some ways to minimize and prevent edge waviness [Halmos, 2006].

Center wave

Center wave occurs primarily at webs, flanges and other portions of the cross-section that are not bent. It frequently occurs in products that have wide cross-section with low material thickness. There are two main mechanisms of occurrence of pocket wave [Halmos, 2006].

During the roll forming process, when the edges are pulled in the trasversal direction, the transversal tensile stress induced in the centre portion is larger than that at the intermediate and edge portions. The bend lines (corners), especially when located in the centre of the strip, are significantly elongated in the transversal direction and shrink in the longitudinal direction. When the shrinkage happens, the compressive stresses are induced in webs, flanges and other flat areas. Elastic buckling (that results in pocket waves) occurs when the compressive stress exceeds each portion's stiffness [Halmos, 2006].

Besides this first mechanism, there is a second that also contributes to the existence of center waves. The corners, when bent transversally elongate both in the transversal and longitudinal direction. Yet, when the semiformed strip exits from the roll gap, the corners that are longitudinally elongated have to shrink back so all the portions of the cross-section have the same length. The shrinkage leads to longitudinal compressive stress induced in flat portions. If this compressive stress exceeds the critical value, longitudinal center waviness occurs [Halmos, 2006].

To minimize the occurence of center waviness some measures might be taken, such as [Halmos, 2006]:

- Increase the gap between rolls in order to reduce tranversal shifting (and, therefore, transversal elongation);
- Optimize the corner bending sequence; bend the center portion first and then intermediate and edge portions; divide the bending appropriately into different steps;
- Use of guide roll and shoes;
- Gardually reduce the radii of convex corners.

Corner buckling

When products have wide cross-section and small material thickness, localized longitudinal elongation tends to occur at the corners. This phenomenon originates small waves that appear periodically along the corners in a sort of plastic shear buckling [Halmos, 2006].

There are ways to prevent corner buckling, the aim is to prevent excessive longitudinal elongation at the corners. Increasing the gap between rolls reduces the longitudinal elongation of each portion and is an effective way of preventing this deffect [Halmos, 2006].

Edge cracking and splitting

Edge cracking happens when the tranversal tensile stress or elongation exceeds the critical value. This usually happens in products with wide coils, thin material and sharp corners. Low formability of the material is also an aggravating factor. Preventing measures are the same as for center wave [Halmos, 2006].

Springback

Springback is the elastic recovery that occurs during unloading of the metal strip. Release of residual stresses after the forming force is cleared leads to geometric deviations in the

work piece cross-section. In figure 2.8 the bending angle differs from the final angle that the material acquires after the release of the loads. On cold roll formed products, springback occurs oftenly. Part geometry, manufacturing process condition and tensile properties of the blank material have great influence on the material behaviour.

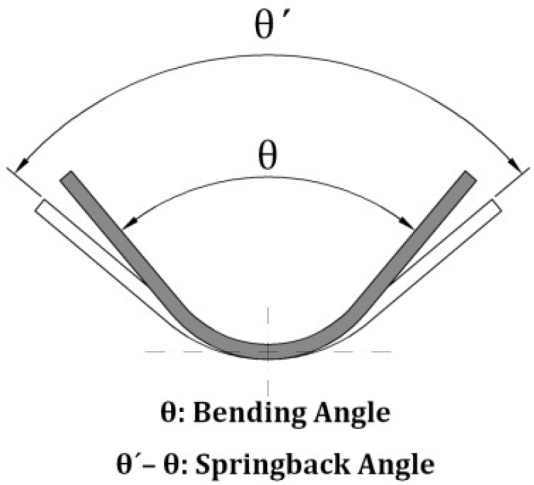


Figure 2.8: Springback [Abvabi et al., 2015].

The magnitude of this defect is associated with the ratio between the residual stresses and the Young's modulus [Abvabi et al., 2014]. Increasing the yield strength and tensile strength of the material leads to higher springback since an increase in yield strength and tensile strength leads to an increase of the elastic limit of the material. On the other hand, an increase in Young's modulus causes the elastic recovery of the material to decrease. Also, greater bending radius or thickness leads to higher springback [Abeyrathna, 2014].

The predominance of springback is greater at the intermediate and edge portions of the profile than at the center of the profile which leads to nonuniform springback deformation along the transversal direction. This causes dimensional innacuracy on the final product [Halmos, 2006].

End Flare

End flare occurs when the formed product is cut off into pieces. The realease of residual shear stress leads to product distortion on the entry and exit ends of the final product. Usually, the ends distort in opposite directions: the profile flairs in at the front and flares out at the end, as seen in figure 2.9 [Halmos, 2006].

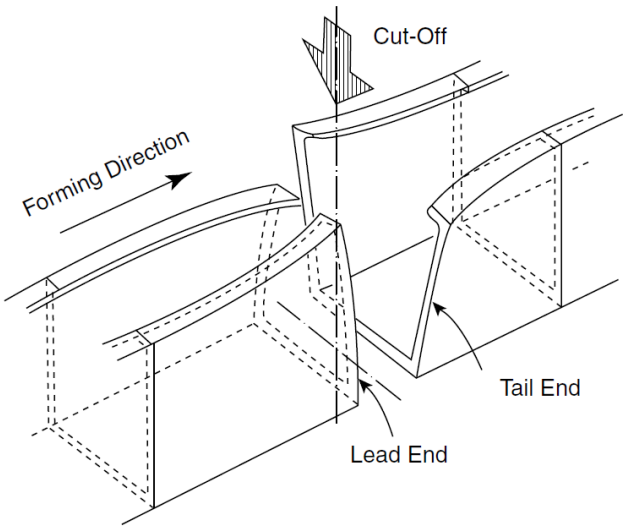


Figure 2.9: Flare of cutoff ends [Halmos, 2006].

2.2 Residual Stresses

Every manufacturing process leads to residual stresses into the materials. When it comes to the products obtained through cold roll-forming, they go through different stages of manufacturing until the final product is achieved. Thin cold-formed steel members, usually start as slabs of the material that have to be melt, hot-rolled, cold-reduced and annealed. The material in sheet form is then coiled and shiped to the producers of roll-formed products. Previously to the cold roll-form process, the thin sheets are uncoiled and flattened. Only then, they are cold roll-formed into the final shape. This complex process generates plastic strains and residual stresses through the sheet thickness that influence the load-displacement response and ultimate strenght of cold-formed steel members [Moen et al., 2008].

This residual stresses are such that they may be responsible for the failure of a structure because they influence fatigue behaviour, fracture strength and even corrosion resistance of mechanical parts. Löhe et al., 2002 state that these residual stresses can either improve fatigue behaviour (for compressive stress, fatigue limit increases) or worsen fatigue behaviour (in the case of tensile stress).

Residual stresses may be considered as a sum of two types of stresses: flexural and membrane. In cold-formed steel members, the stresses through thickness are mainly flexural. Membrane residual stresses are more prevalent in roll-formed members than press-braked ones. Compressive strength decreases with membrane stresses and these exist mostly in corner regions. To counterbalance this effect, yield stress is elevated in the corners as a result of the significant cold work of forming [Schafer and Peköz, 1998].

An extensive experimental investigation of the residual stresses in cold-formed steel members was presented by Weng and Pekoz, 1990. The authors characterized the magnitude and distribution of the residual stresses in order to better understand the behaviour of these stresses in steel members.

Abvabi et al., 2015 investigated the effects of residual stresses on the final shape in roll forming; for that numerical and experimental approaches were applied. Two different metal strips were used: one that was directly applied in roll forming and the second that was previously rolled in order to reduce thickness. The results of the experimental approach

were then compared to those of the FEA. The following conclusions were presented by the authors [Abvabi et al., 2015]:

- An increase of the yield strength as a result of thickness reduction, reduces the difference between the final longitudinal strain at the edge and the middle of the strip. Bow prediction can be improved if pre-existing stresses are taken into account in numerical models;

- Variaton on springback angle happens mainly due to material strength variation which is a result of plastic deformation during thickness reduction. Including these stresses in the FEA analys does not affect significantly the accuracy of springback prediction;

- End flare in the metal strip occurs as a combination of an increasing material strength (due to plastic deformation during thickness reduction rolling) and the degree of residual stresses after roll forming in the front of the strip. Increasing material strength reduces end flare while higher degrees of logitudinal stress at the front of the strip increase end flare. Better accuracy in the numerical model can be achieved when residual stress information is included.

Amouzegar et al., 2016 proposed a comprehensive incremental numerical method to calculate residual stresses and strains in cold formed members, both in the flat parts and in corner regions. This method was developed in a way that it simulates the cold-working process including coiling, uncoiling, flattening and cold-forming (either by press-breaking or roll-forming). In order to obtain the algorithm, the authors assumed that the steel sheet is free from residual stresses prior to coiling. Also, the strains perpendicular to the bending direction were ignored and it was assumed that strain hardening is isotropic. The main conclusions of this study were:

- Residual stresses in corner regions are marginally affected by the specifications of the cold-formed steel member;

- In flat regions, residual stresses can be significant depending on the coil radius, yield stress and sheet thickness;

- In flat regions, strain hardening has a negligible contribution to the variability of residual stresses;

- For particular values of sheet thickness and coil radius, depending on the value of yield stress, no residual stresses will develop;

- Corner radius greatly affects the equivalent plastic strain and variations of section thinning in corner regions.

Moen et al., 2008 proposed a general method for predicting the manufacturing residual stresses and plastic strains in cold-formed steel members. This method considered through-thickness residual stress and strain distributions caused by coiling, uncoiling, flattening of the steel sheet and cross-section cold-forming. Quach et al., 2004 had already proposed an analytical solution on the effects of coiling and uncoiling on sheet metal strips.

Ma et al., 2015 performed an experimental study on material properties and residual stress distribution of cold-formed high strength steel hollow sections. Previous studies on residual stresses in tubes were made by Kato and Aoki, 1978.

2.3 Fatigue analysis

Fatigue is a process that causes failure or permanent damage to components subjected to repeated loading. The loads applied have maximum values lower than the tensile strength of the material; this means that a structure may fail at a stress level inferior to the one required to cause failure under static conditions. Fatigue failure is a multi-stage process that begins with the initiation of cracks which, as a result of continued cyclic loading, propagate leading to the rupture of the component [Boardman, 1990], [Ellyin, 1997]. For fatigue damage to occur cyclic stress, tensile stress and plastic strain have to be present. Platic strain resultant of cyclic stress initiates the crack; crack propagation is then promoted by tensile stress. Even though compressive stresses will not cause fatigue, compressive loads may be responsible for local tensile stresses [Boardman, 1990].

The behavior of a metal subjected to cyclic loading is highly influenced by processing, fabrication, heat treatment, surface treatments, finishing and service environment. Manufacturing procedures as cold forming, welding, brazing and plating as well as surface roughness and residual stresses also play an important role on the fatigue resistance of structures [Boardman, 1990].

Besides material properties, load type (uniaxial, bending or torsional), loading pattern (periodic loading with constant or variable amplitude or random loading), magnitude of peak stress and overall size of part should also be taken into account when performing a fatigue analysis [Boardman, 1990].

Crack initiation usually occurs on the surface of the material because that is the area where the maximum effect of the accumulated stresses is felt. On the other hand, surface crystals are less constrained when it comes to deformation (when compared to the crystals located on the inner parts of the material) which promotes plastic strain under stress. Lastly, surface region is also the most exposed to the environmental effects [Tavares de Castro, 2017].

In order to prevent fatigue failure some methods may be applied. The most effective and economical way to do so is improving the design. The following procedures may be taken into account [Boardman, 1990]:

- Simplify the part so that stress is reduced or even eliminated;
- Avoid sharp surface notches;
- During processing or heat treatment, prevent decarburizing or surface discontinuities;
- Reduce or eliminate tensile residual stresses that may result from manufacturing, heat treatment and welding;
- Protect against corrosion, erosion, chemical attack or service induced cracks.

2.3.1 Definitions

Tensile stresses are, usually, considered positive while compressive ones are considered negative. Stress ratio R is commonly used to describe the loading type. R is given by Eq. (2.1):

$$R = \frac{\sigma_{min}}{\sigma_{max}} \tag{2.1}$$

R can range from -1 to 1 and its value can define the loading conditions [Boardman, 1990]:

- R=-1: stresses are fully reversed;
- R=]-1,0[: stresses are partially reversed;
- R=0: stress is cycled between a maximum stress and null stress (pulsating load);
- R=]0,1[stress is cycled between two tensile stresses;
- R=1: no variation in stress (sustained-load, creep rather than fatigue)

The mean stress σ_m is given by Eq. (2.2):

$$\sigma_m = \frac{\sigma_{min} + \sigma_{max}}{2} \tag{2.2}$$

The range of stress σ_r is given by Eq. (2.3):

$$\sigma_r = \sigma_{max} - \sigma_{min} \tag{2.3}$$

The stress amplitude σ_a is half of the stress range:

$$\sigma_a = \frac{\sigma_r}{2} \tag{2.4}$$

S-N curves diagrams are used to represent the results of fatigue tests which are usually plotted as maximum stress or stress amplitude versus the number of cycles (N) to fracture. A logarithmic scale is used to plot the number of cycles and stress may be plotted in either a logarithmic or linear scale [Boardman, 1990]. In ferrous alloys, the S-N curve flattens out so that below a certain endurance limit σ_{fo} failure does not occur regardless of the number of cycles applied. The designer should develop the structure in order to keep the stresses below σ_{fo} by a suitable safety factor.

When it comes to fatigue design, there are different approaches that may be used taking into account the specificities of the strucuture. There are several models for fatigue design being the most widely used one of the following [Stephens et al., 2001], [Pereira, 2006]:

- Nominal stress-life model (S-N) also known as Wöhler method: this method relates nominal stresses with fatigue strength for notched and unnotched members. The material is assumed to deform in a nominally elastic manner, local plastic strains are neglected. This approach is useful only if the consideration that all stresses are essentially elastic is valid. These models usually describe the total life of the component and are based on the Wöhler curves (S-N curves).

- The local strain-life (ϵ-N) model or Coffin-Manson method: this method focuses on the local strains at a notch and relates them with smooth-specimen strain-controlled fatigue behaviour. It takes into account both elastic and plastic responses to applied loadings and it is commonly applied in components subjected to high plastic stresses/strains. This method is used to predict crack initiation. Log-log plots are used to represent the data. In the abscissa is the number of strain reversals (twice the number of cycles) to failure and the ordinate is the strain amplitude (half the strain range). The local stress-strain relation features an hysteresis loop that is caused by the presence of plastic strain; for pure elastic loading the loop becomes a straight line with the slope representing Young's modulus, E.

- The fatigue crack growth (*da/dN-ΔK)* or Paris method: Fracture Mechanics is used to predict the number of cycles required to grow a crack from initial pre-existing deffects to cracks that may be responsible for failure. This method is commonly used in addition to the local strain-life method for a more complete analysis.

Criteria for fatigue design have evolved and, depending on the application, each of the developed criteria may be applied. Infinite-life criterion was the first used for fatigue design and requires local stresses or strains to be essentially elastic and safely below the pertinent fatigue limit. It is still currently used for parts subjected to millions of cycles (like engine valve springs) however variable amplitude loading is common and pertinent fatigue limit is difficult to define. This criterion may not be economical or practical. Safe-life design is used to develop parts with an expected finite life. A safety margin is included to atone for any unkonown factors and for the scatter of fatigue results. Stress-life, strain-life or crack growth relations may be used to base the calculations on. Fail-safe design admits that fatigue cracks may occur but structures have to be designed in such way that cracks can not lead to failure before being detected and repaired. Damage-tolerant design assumes that cracks will exist and are caused either by processing or by fatigue and resorts to fracture mechanics to determine if the cracks will grow large enough to lead to failure before they are detected by periodic inspection [Stephens et al., 2001].

EN 1993-1-9 (2005), part of the Eurocode 3 which provides guidelines for the design of steel structures, gives methods for the assessment of fatigue resistence of members, connections and joints subjected to fatigue loading. These methods are applicable to all grades of structural steels, stainless steels and unprotected weathering steels with the few exceptions specified in the European Standard. Fatigue assessment methods presented in EN 1993-1-9 (2005) are based on S-N curves (notch strain and fracture mechanics methods are not included).

EN 1993-1-9 (2015) specifies that fatigue strength for constant amplitude stress ranges and a maximum number of cycles $N = 5 \times 10^6$ with $m = 3$, can be obtained using Eq. (2.5):

$$\Delta\sigma_R^m N_R = \Delta\sigma_C^m \times 2 \times 10^6 \tag{2.5}$$

where m is the slope of fatigue strength curve, N_R is the design life time expressed as a number of cycles related to a constant stress range and $\Delta\sigma_C$ is the reference value of fatigue strength at $N_c = 2$ million cycles. For direct stress ranges, fatigue strength curves as shown in figure 2.10 can be used.

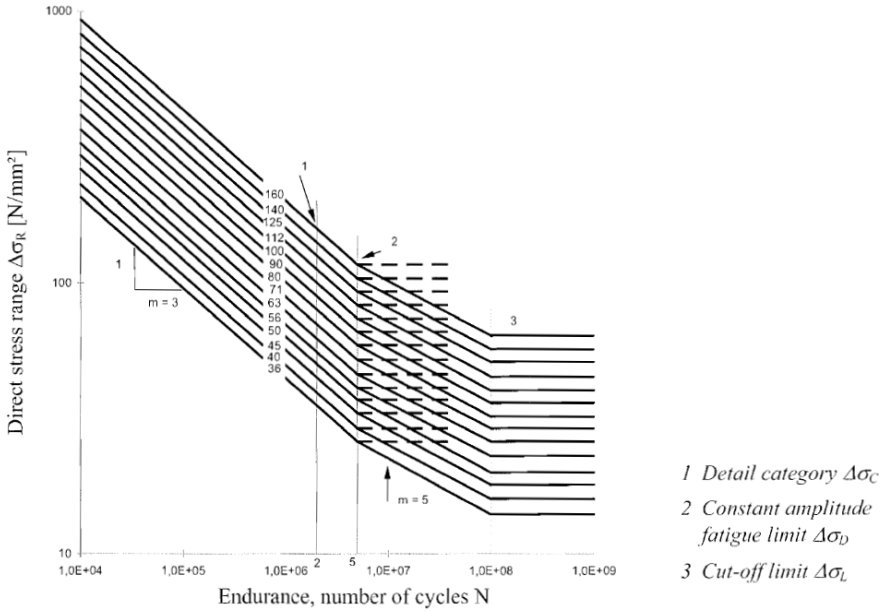


Figure 2.10: Fatigue strength curves for direct stress ranges (EN 1993-1-9 2015)

Each fatigue curve expresses the quantitive relationship between stress range and number of cycles to fatigue failure, used for the fatigue assessment of a specific category of structural detail. Curve identified as 160 represents rolled or extruded products. This category is the one with better fatigue strength at any number of cycles.

The S-N global approach suggested by EN 1993-1-9 (2005) has some limitations. It only provides information about fatigue life without any indication about necessary cycles for crack initiation and propagation. This approach also doesn't take into account the effects of specimen size and geometry. Therefore, local approaches to fatigue and Fracture Mechanics emerged, that allow for more comprehensive studies on the behavior of certain specimens.

"The local approaches, recognizing the localized nature of the fatigue damage, propose the correlation of a local damage parameter (e.g. strain, energy) with the number of cycles required to initiate a macroscopic crack" [Jesus et al., 2012].

Basquin, 1910 presented a stress based law, most applicable in high cycle fatigue regime:

$$\frac{\Delta\sigma}{2} = \sigma'_f(2N_f)^b \tag{2.6}$$

where $\Delta\sigma$ is the stress range, σ'_f is the fatigue strength coefficient, $2N_f$ is the number of reversals to failure and b is the fatigue strength exponent.

A Law for cumulative damage under stress cycles with varying magnitudes was established by Miner [1990] in the mathematical form of:

$$\sum\nolimits_{Di} = \sum \frac{n_i}{N_i} \tag{2.7}$$

n is the number of applied cycles and N is the number of cycles required to cause failure when the same load i is applied. Failure occurs for $\sum_{Di} = 1$. Miner states that this Law is more accurate for alluminium alloys than it is for steel alloys.

Coffin and Manson, 1954 developed methodologies for low-cycle fatigue regime in terms

of plastic strain range, as seen in Eq. (2.8):

$$\frac{\Delta\epsilon^p}{2} = \epsilon'_f(2N_f)^c \tag{2.8}$$

with $\frac{\Delta\epsilon^p}{2}$ being the plastic strain amplitude, ϵ'_f the fatigue ductility coefficient and c the fatigue ductility exponent.

Morrow, 1965 also developed a relation as expressed in Eq. (2.9):

$$\frac{\Delta\epsilon}{2} = \frac{\Delta\epsilon^E}{2} + \frac{\Delta\epsilon^P}{2} = \frac{\sigma'_f}{E} \times (2N_f)^b + \epsilon'_f(2N_f)^c \tag{2.9}$$

$\Delta\epsilon$, $\Delta\epsilon^E$ and $\Delta\epsilon^P$ are, respectively, the total, the elastic and the plastic strain ranges.

Fatigue tests of smooth specimens under strain-controlled conditions are performed in order to determine the constants in these relations. Furthermore, these tests can be used to identify the cyclic curve of the material which relates the stress amplitude with the strain amplitude.

Eq. (2.6) is only valid for $R = -1$. Morrow suggested a modification to the Basquin relation in order to include the effects of mean stresses:

$$\frac{\Delta\sigma}{2} = (\sigma'_f - \sigma_m)(2N_f)^b \tag{2.10}$$

Smith et al., 1970 also proposed an alternative to (2.9) in order to account for the effects of mean stresses:

$$\sigma_{max}\frac{\Delta\epsilon}{2}E = (\sigma'_f)^2(2N_f)^{2b} + \sigma'_f\epsilon'_f E(2N_f)^{b+c} \tag{2.11}$$

where σ_{max} is the maximum stress of the cycle.

Another alternative approach to the S-N curves is based on the fatigue crack propagation phenomena: Fracture Mechanics. The most widely used crack propagation law is the Paris' law ([Paris et al., 1961]) expressed in Eq. (2.12):

$$da/dN = C(\Delta K)^m \tag{2.12}$$

where da/dN is the fatigue crack growth rate, C and m are material constants and ΔK is the stress intensity factor range.

Fatigue properties of an S355 mild steel were studied by Jesus et al. [2012] who performed an experimental program that included fatigue tests of smooth specimen as well as fatigue crack propagation tests. The fatigue tests were performed with a strain ratio, R_ϵ of -1. Cyclic constants obtained by the experimental work in addition to other fatigue parameters are shown in Table 2.1. Despite the steel considered in this study was S350GD grade (preliminary assumption for the rail steel) and S355MC grade (used in the production of the sections) being slightly different it is not expected that they show significantly different fatigue and elastoplastic properties.

Table 2.1: Cyclic elastoplastic and fatigue properties of S355 structural steel [Jesus et al., 2012]

Material	K' [MPa]	n'	σ'_f [MPa]	b	ϵ'_f	c	$2N_f$
S355	598,85	0,0757	952,2	-0,089	0,7371	-0,664	7095

2.3.2 Fatigue analysis of cold formed steel profiles

Although fatigue design guidelines for hot-rolled steel structural members and connections exist, there are no acceptable fatigue design guidelines for cold-formed steel members or connections. The aim of the FASTCOLD project is, therefore, to develop general design rules for the design of cold formed steel members and connections subjected to fatigue loading. Available data and previous studies on the matter are very limited.

Klippstein performed an extensive research project, between 1980 and 1988, with the objective of evaluating the fatigue behavior of cold-formed steel members and connections. The research was primarily focused on the application of cold-formed steel members and connections in the ground-transportation and agricultural equipment industries [LaBoube and wen Yu, 1999]. The study included several types of beam details and steels with different yield strengths and different welding processes. The tests were conducted on 24 steel sheet beam specimens exposed to constant amplitude as well as limited variable-amplitude stress cycles was presented. Conservative fatigue-design curves developed in previous studies on similar details in welded beams produced from plate steels or in hot-rolled beams were compared to the results obtained by Klippstein. With this, the author concluded that conservative fatigue-design curves used for fatigue design of large details were suitable for small details fabricated from steels sheets used in the ground transportation and agricultural-equipment industries [Klippstein, 1980].

In the 1981 report, Klippstein tested 77 welded cold-formed steel sheets specimens on a constant amplitude stress cycle. The test specimens had varying yield strengths and different beam types were used [LaBoube and wen Yu, 1999].

Experimental studies that compiled 163 tests were reported in 1985. Constant amplitude fatigue tests with stress ratios that varied from -1 to 0 were used. Klippstein compiled all of the studies until then and suggested a design methodology based on S-N curves.

Klippstein continued his research and in 1988 proposed a classification system for various stress ranges (see Table 2.2). This classification was built based on the relation between stress range and life cycle presented by Fisher (Eq. 2.13):

$$\log(N) = C_f - m\log(F_{SR}) \tag{2.13}$$

with

$$C_f = b - (n \times s) \tag{2.14}$$

N is the number of full cycles, m is the slope of the mean fatigue analysis curve, F_{SR} is the effective stress range, b is the intercept of the mean fatigue analysis curve, n is the number of standard deviations to obtain a desired confidence level and s is the approximate standard deviation of the fatigue data. Klippstein recommended that $n = 3$ and $s = 0.25$ [LaBoube and wen Yu, 1999].

A paper regarding fatigue tests results performed on 52 cold-formed steel members was presented by Polyzois et al. [1994]. The main goal of Polyzois et al. [1994] research was to study the possible consequences of varying winds on transmission towers. Wind was considered a time-variant load that led to fatigue damage in the transmission towers. The research was carried out through the study of axial fatigue behavior of full-size cold formed steel members commonly used in the construction of the towers. Similar conditions to those encountered in service (loading and environment) were assured during the tests. The experimental program included 52 constant amplitude fatigue tests with a load ratio of -1. Polyzois et al., 1994 concluded that the stress range was the dominant stress variable influencing the fatigue behavior of the tested cold-formed steel sections. Variables such as minimum and maximum stress and stress range did not show significant effect

Table 2.2: Klippstein's Fatigue Design Categories [LaBoube and wen Yu, 1999]

Description	Stress Category	Constant C_f
Base metal and components with as received surfaces, including sheared edges and cold-formed corners.	A	$3,16 \times 10^{10}$
Base metal and weld metal in members connected by continuous longitudinal fillet welds.	B	$1,0 \times 10^{10}$
Continuously welded attachments to a plate or a beam, transverse web stiffeners, transverse fillet welds, weld washers with outside diameter less than 2 inches and continuous longitudinal welds in regions of cold-forming and subsequent welding.	C	$3,16 \times 10^{9}$
Weld washers with diameter ranging from 2 to 4 inches. Any welded attachment with a length of 2 to 4 inches parallel to the direction of the applied stress. Transverse welds in regions of cold-forming.	D	$1,0 \times 10^{9}$
Attachments longer than 4 inches parallel to the direction of the applied stress and intermittent welds parallel to the direction of the applied stress.	E	$3,16 \times 10^{8}$
Bolt and screw holes in connections and other punched and drilled holes, spot welds and shear connectors.	F	$1,0 \times 10^{10}$

on the sections. Most fatigue failures appeared at the extremity of the end hole of the specimens. Cycle-dependent softening (stiffnes reduction) was observed for all specimens. Fractures asssociated with very short crack size were attributed to large reductions in fracture toughness and ductility associated with low temperatures.

Gustavsson et al. [1997] presented a paper aiming to compare constant amplitude fatigue properties of six low carbon sheet steels used in automotive pressed structural members. The research included fatigue test experiments both on smooth specimens and on a laboratory pressed sheet specimen. Fatigue life prediction using the local strain approach as well as fatigue crack growth analysis was also part of the study. The authors showed that fatigue life prediction using local strain approach was overly conservative and suggested the accounting for prestraining of the sheet material or fatigue crack growth consideration to improve predictions. They also concluded that increasing the tensile strength of the material generally causes an increase on the fatigue strength both in the case of fully reversed strain controlled fatigue testing of smooth specimens and fully reversed bending test of a pressed sheet specimen.

Table 2.3: Intercept for mean fatigue curves [LaBoube and wen Yu, 1999]

Stress Category	b
A	11,0
B	10,5
C	10,0
D	9,5
E	9,0
F	10,5

2.4 Finite element method analysis

"Finite element method is a technique in which a given domain is represented as a collection of simple domains, called finite elements, so that it is possible to systematically construct the approximation functions needed in a variational or weighted-residual approximation of the solution of a problem over each element." [Reddy, 1993]. The method has three basic features:

- Division of whole into parts: that allows for the simplified representation of complex domains as a group of simpler domains enabling a systematic derivation of the approximation funtions.
- Derivation of approximation functions over each element.
- Assembly of elements: based on the continuity of the solution and balance of internal fluxes.

Numerical methods transform mathematical expressions into a set of algebraic equations that depend on a finite set of parameters [Oñate, 2009]. The geometry of the elements used to represent the domain of a problem and the number and location of the nodes influence greatly the resultant approximation functions [Reddy, 1993]. When applied in real problems, these equations involve a large number of unknowns and, for that reason, computers are used to solve the final system of algebraic equations. In structural engineering problems, these methods incorporate mathematics, material modelling and computer science. FEM allows the computing of stresses, strains and displacements in a structure under a set of loads [Oñate, 2009].

The roll forming industry has improved in part quality and lowered costs since the introduction of finite element analysis (see figure 2.11). Every step of the design process can be analysed before any manufacturing takes place. Changes and improvements are simple and fast to apply. Before the simulation models were used, the roll forming know-how was based on the designer experience and machine operator and design evaluation of resultant products. Tools were produced right after the inital design and a trial and error process would follow in order to attain the desired quality of the final product. Re-tooling or re-engineering made this process very time consuming and cost inefficient.

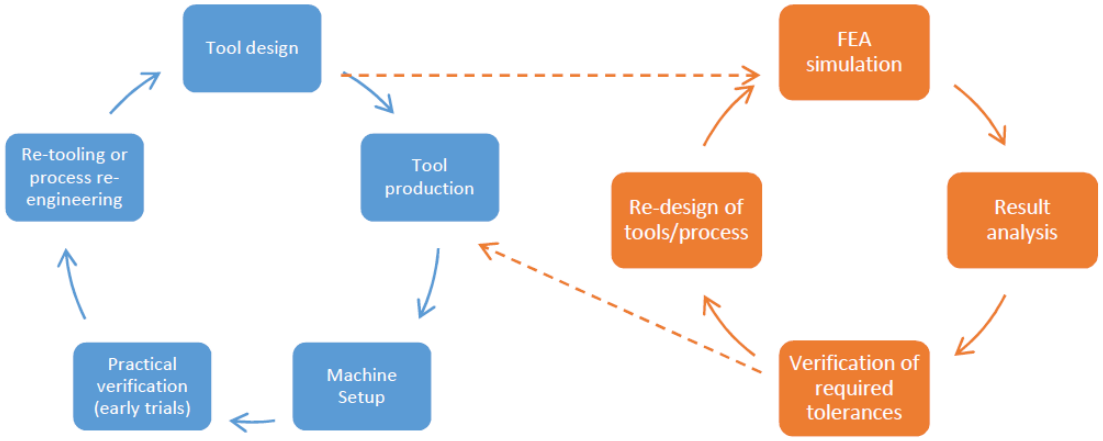


Figure 2.11: Design process of a roll forming line; in blue is the traditional process of trial and error; in orange, the upgraded process with virtual testing; dashed lines represent the connection between the cycles [Ferreira, 2016].

The integration of FEA software during the design process allowed for extreme reductions in simulation preparation time and enabled designed to setup virtual roll forming lines where the whole process can be carried out and analysed in a cost efficient manner. The application and use of FEA software should not eliminate the need for experienced and knowledgeable designers, though. It should instead improve the process by enabling engineers to detect problems before the manufacturing process starts. By introducing the use of FE simulation of roll forming, the company aims to [Abe, 2010]:

- increase process stability;
- improve the understanding of the roll forming process;
- predict achievable geometrical tolerances;
- optimize the process by reducing forces, roll tool wear, material load and energy comsumption;
- predict and optimize product quality.

2.5 Previous FASTCOLD research

The simulation models analysed in the present work were developed using the COPRA® FEA RF package that automatically prepares the simulation based on the roll design developed in COPRA® RF. The simulation and analyses presented in this research are a continuation of the work developed by Martins [2018] in the scope of the FASTCOLD project.

Martins [2018] performed a parametric study comprised of nine simulations of a U-channel profile to analyse the influence of several parameters on the final shape of cold rolled formed steel profiles. An evaluation of residual stresses distribution across the thickness and along the surface of the strip width was carried out. For fatigue life prediction of the studied components when subjected to cyclic loading, a local stress-based approach was used. The stress range calculated included the stresses after roll forming and the stresses induced by external loading. For a Z-section profile, an identical fatigue analysis

was performed. In addition, a roll forming numerical simulation was conducted for the Z-profile in order to analyse the three-dimensional effects of the manufacturing process.

The major conclusions of Martins [2018] report are the following:

- Residual stresses across the thickness displayed differences in stress distribution from the theoretical solution of press-braked profiles, as a result of the existence of three-dimensional effects that cannot be neglected.
- The fatigue analysis results showed that bending regions are the critical areas where fatigue cracks initiate.
- A kinematic hardening rule should be more suitable than and isotropic one since the Bauschinger effect needs to be reproduced. However, this simulation was not considered in her study and left as a suggestion of future works.

Chapter 3

Z-Profile characterization

In this chapter, the experimental work performed in order to characterize a cold rolled rail profile is presented and explained. Various tests were performed on cold roll-formed Z-section profiles provided by Schäffer. Mechanical properties were studied both through tensile tests performed in 9 samples extracted from different areas/directions aiming at evaluating the geometry deviations from the nominal geometry of the profiles as well as through microstrucutre analysis done in 5 samples of material extracted from various regions of the Z-section. A geometric analysis of the profiles was also accomplished using a contact probe (LVDT) and an optical (GOM) methodology.

The experimental results obtained will be compared with the results of numerical simulations.

3.1 Z-section profile

The Z-section profile provided by Schäffer and studied in this dissertation can be seen in figure 3.1 and its dimensions are shown in figure 3.2.

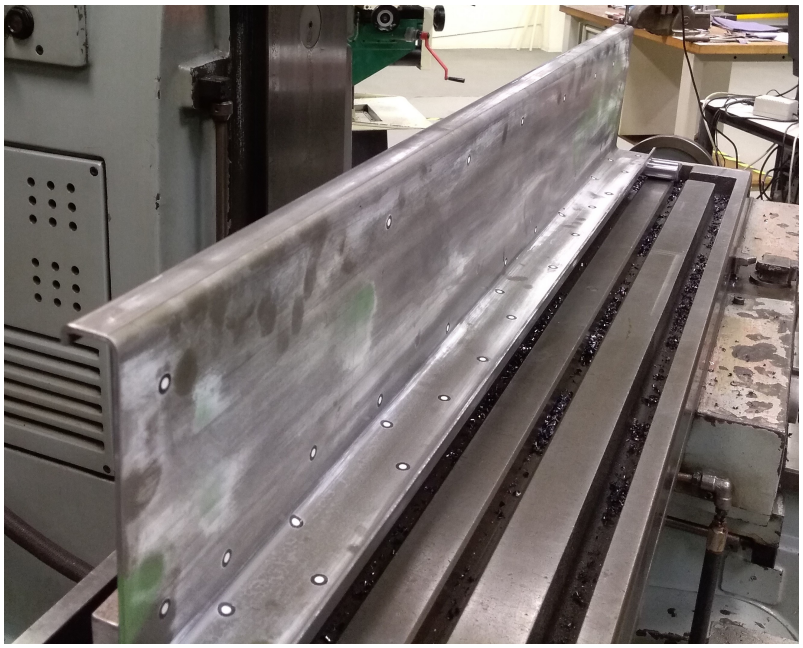


Figure 3.1: Cold rolled rail profile.

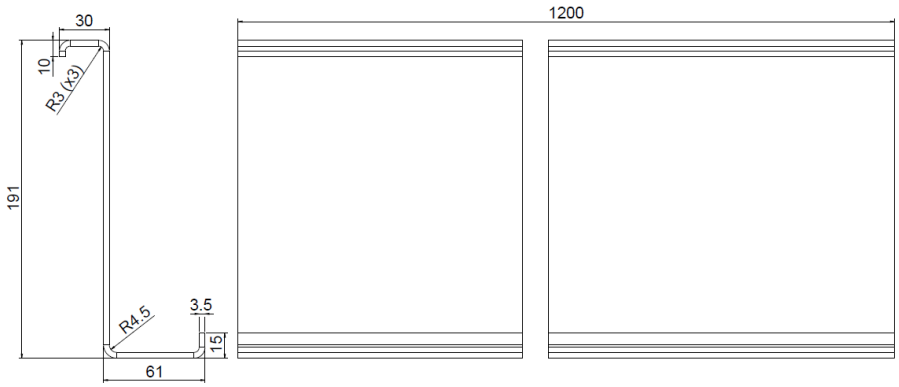


Figure 3.2: Dimensions of the Z-section profile.

The nomenclature used to refer to the different aspects of the profile will be the same adopted by Martins [2018] as shown in figure 3.3.

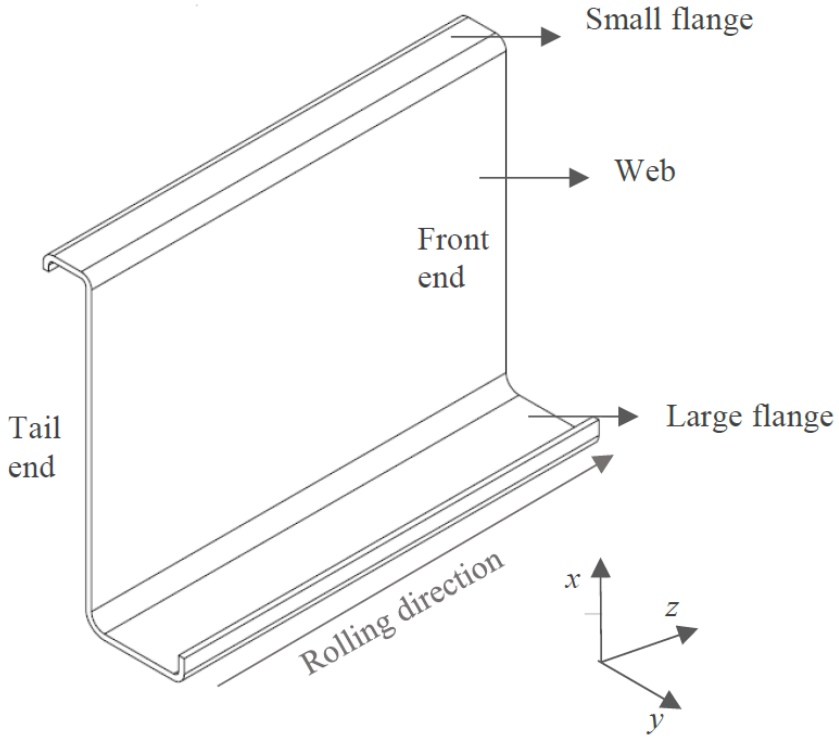


Figure 3.3: Nomenclature used to describe the Z-section profile [Martins, 2018].

The Z rail profile was produced using S355MC steel without any surface coating. The material is used in a variety of applications including structural beams, frames and as cold rolled steel sections. The steel benefits from good weldability but heat treatment should be avoided as this is known to reduce the yield strength of the material.

The chemical composition of S355MC High Yield Steel according to the norm EN10149-2 are summarised in table 3.1 and its mechanical properties can be seen in table 3.2.

The material was supplied in a coil that was uncoiled prior entering the roll forming machine.

Informations about the roll forming machine used to produced the Z rail profile were

Table 3.1: Chemical composition (weight %) of S355MC according to UNI EN 10149-2.

Element	**Fe**	**Al**	**C**	**Mn**	**Nb**	**P**	**S**	**Si**	**Ti**	**V**
Min.	97,17	0,015								
Max.	99,98		0,12	1,50	0,09	0,025	0,020	0,50	0,15	0,2

Table 3.2: Mechanical properties of S355MC according to UNI EN 10149-2.

Yield Strength $R_{p0,2}$ **[MPa]**	$\geqslant 355$
Ultimate Tensile Strength R_m **[MPa]**	430 - 550
Elongation at Ultimate Tensile Strength A_{80} [%]	$\geqslant 19$

not provided in time to be included in this study, they should however be part of future studies performed in the scope of the FASTCOLD project in order to obtain more realistic simulation results of the manufacturing process.

3.2 Mechanical properties

3.2.1 Tensile tests

In order to determine the experimental engineering stress-strain curve of the material, tensile tests were performed according to NP EN ISO 6892-1. A total of 9 specimens were machined: 6 on the longitudinal/roll forming direction and 3 on the transversal direction. The location of the extracted samples and their dimensions can be seen in figures 3.4 and 3.5.

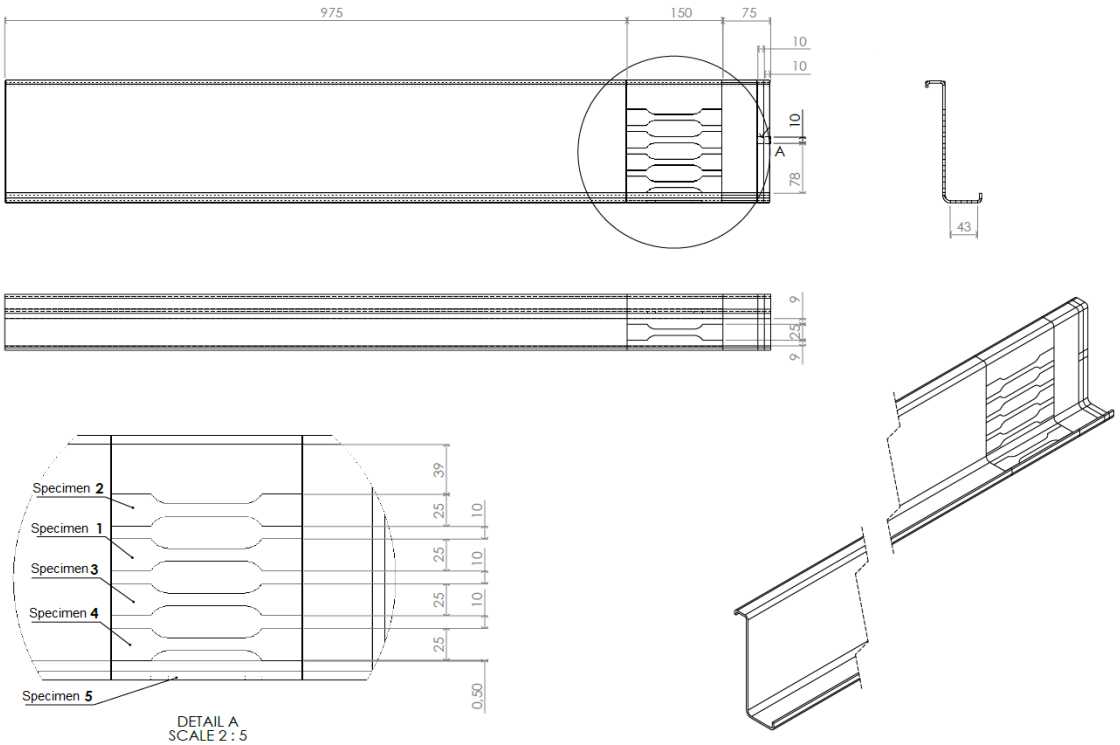


Figure 3.4: Dimensions and location of longitudinal specimens.

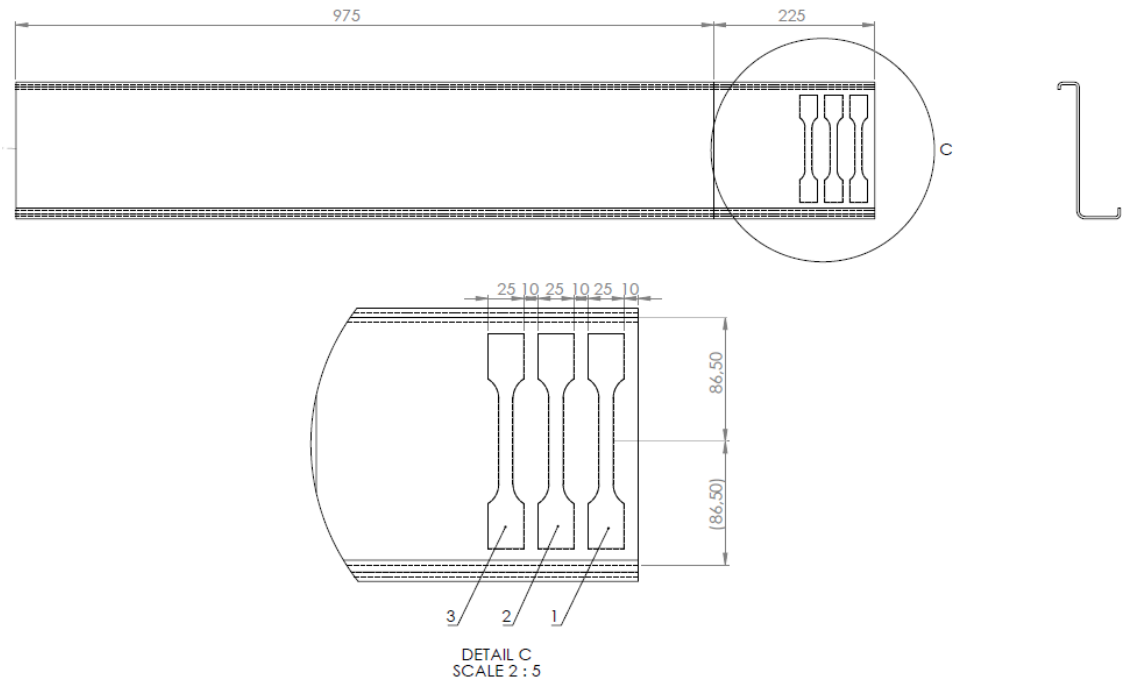


Figure 3.5: Dimensions and location of transversal specimens.

The samples were machined from different areas to verify if the effects of the roll forming process in the mechanical properties of the material were similar throughout the whole section. As shown in figure 3.6 the sample with the number 1 was engraved with the Schäffer logo, something to take into account when evaluating the results.

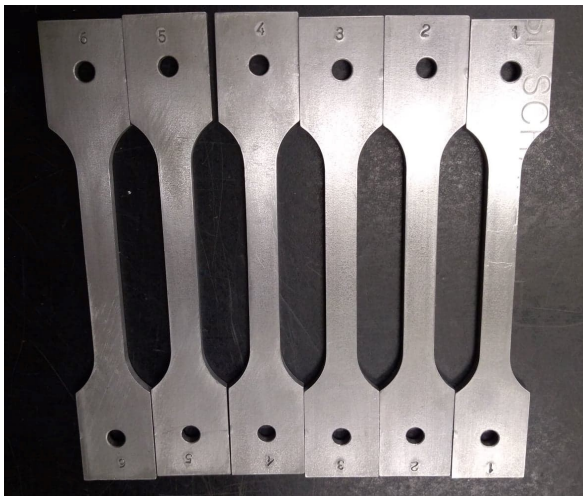


Figure 3.6: Machined samples from the Z-section profile on the longitudinal direction (before the tensile test).

The tensile tests were carried out in the *Laboratório de Ensaios Tecnológicos (FEUP)* on a servo-hydraulic machine with a load cell with 100kN of capacity at a test rate of 1 mm/min (figure 3.7). In order to measure the strain, a MTS strain gauge was applied to the profile sample.

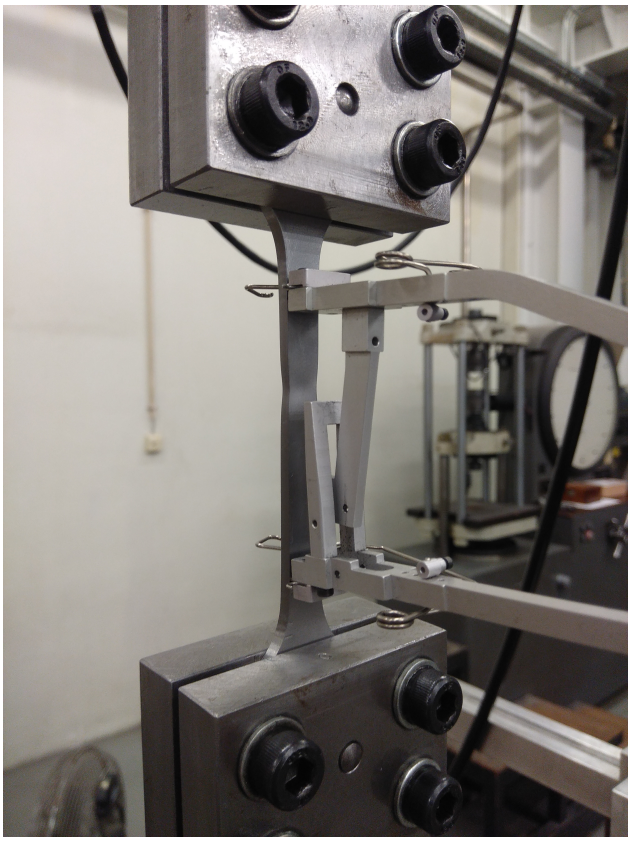


Figure 3.7: Setup for the tensile test.

The tensile tests were performed until material rupture. From the tensile test, an engineering stress-strain curve can be obtained. It should be noted that the engineering stress-strain curve only considers the specimen's initial size.

$$\sigma_{eng} = \frac{F}{A_0} \tag{3.1}$$

$$\epsilon_{eng} = \frac{l - l_0}{l_0} \tag{3.2}$$

Where:

- σ_{eng} is the engineering stress;
- ϵ_{eng} is the engineering strain;
- F is the applied load;
- A_0 is the initial area of the specimen's cross section;
- l_0 is the initial length of the specimen's gauge;
- l is the current length of the specimen's gauge.

The stress-strain curves seen in 3.9 show the results of the tests performed on the 9 specimens. Results of the specimens cut on the longitudinal direction are identified with an L and the ones cut on the transversal direction are identified with a T. The

results were very similar between the specimens of the same direction. However, when comparing the two directions, it is possible to verify that there is anisotropy, tranversal direction samples exhibit higher yield resistence but lower ductility when compared to the longitudinal ones. The elongation at break presents significant differences between the two directions: transversal specimens feature a mean value for elongation at break of 23,3 and longitudinal specimens of 28,3. The tested material (S355MC) also presents an yield plateau on both directions, opposed to what happened in tests performed on S350GD that did not feature an yield plateau in its engineeering stress - strain curves.



Figure 3.8: Specimens after tensile tests.

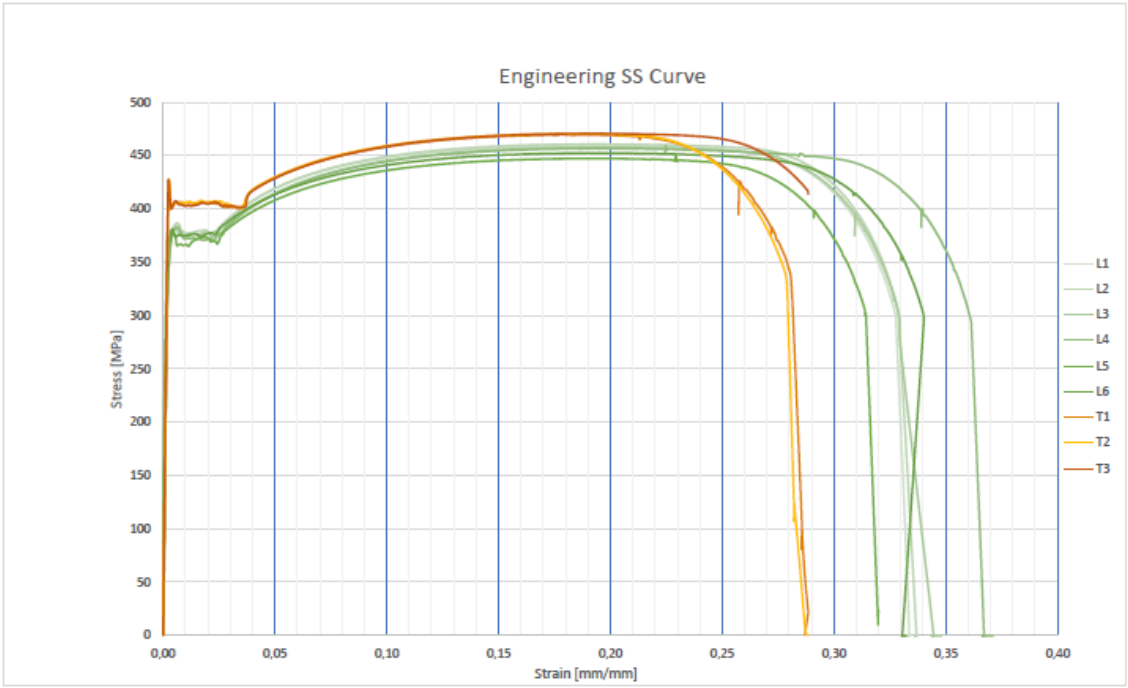


Figure 3.9: Results of the tensile tests on the longitudinal (L) and transversal (T) specimens.

The mean mechanical properties of the tested steel specimens for the longitudinal and transversal directions are shown in table 3.3 as well as the mechanical properties of S350GD

attained previously by Martins [2018]. Comparing these values with the ones required by the standard (see table 3.2), the yield strength presented by S355MC steel only totally complies with the standard in the tranversal direction, however its value of elongation at ultimate strength is slightly lower than the value required.

Table 3.3: Mechanical properties obtained experimentally of the two materials used.

Name	Yield Strength $R_{p0,2}$ [MPa]	Ultimate Tensile Strength R_m [MPa]	Elongation at Ultimate Tensile Strength A_{80} [%]
S350GD	430	611	22,3
S355MC (T)	385	471	18,6
S355MC (L)	331	457	20,3

The material presents an anisotropic behaviour, the mechanical properties in the tranversal direction differ from the ones in the longitudinal direction.

From the data collected from the experimental work, the true stress - true strain curves can also be obtained. The relationship between engineering stress and engineering strains and true stresses and true strains is given by Eq. 3.3 and Eq. 3.4:

$$\sigma_{true} = \sigma_{eng}(1 + \epsilon_{eng}) \tag{3.3}$$

$$\epsilon_{true} = \ln(1 + \epsilon_{eng}) \tag{3.4}$$

Equations 3.3 and 3.4 are true only for the region of uniform plastic behaviour of the material since it does not consider the variations that occur on the specimens section and in the elastic region there is no volume conservation. Despite all this, the errors associated with this approximation are small and will be disregarded.

The plastic behaviour of the material can also be defined using Swift's law 3.5:

$$\sigma = K(\epsilon_0 + \epsilon_p)^n \tag{3.5}$$

Where:

- σ is the true stress;
- ϵ_p is the true plastic strain;
- K, n and ϵ_0 are material constants determined from a uniaxial tensile test.

On the other hand, the elastic strain depends on the current stress and it is given by Eq. 3.6:

$$\epsilon_e = \frac{\sigma_{true}}{E} \tag{3.6}$$

σ_{true} being the true stress and E being the Young's modulus.

The sum of the plastic strain, ϵ_p and the elastic strain, ϵ_e results in the total strain, ϵ_t:

$$\epsilon_t = \epsilon_p + \epsilon_e \tag{3.7}$$

Knowing that Swift's Law characterizes the material behaviour in the plastic region, ϵ_0 can be assumed as the strain at yield. Given the dimension of this value (less than 0.01) it will be neglected and assumed as $\epsilon_0 \approx 0$.

Also,

$$n = \frac{\log(\frac{\sigma_1}{\sigma_2})}{\log(\frac{\epsilon_1+\epsilon_0}{\epsilon_2+\epsilon_0})} \tag{3.8}$$

Where:

- ϵ_i is the plastic strain at a given point of the stress-strain curve;
- σ_i is the stress at a given point of the plastic stress - plastic strain curve;

The strenght coefficient, K is the true stress for ϵ=1. The values for all the constants can be seen in 3.4.

Table 3.4: Swift's Law constants.

	K [MPa]	n	ϵ_0
Longitudinal Direction	734,8	0,17	0
Transversal Direction	750,9	0,17	0

Since the results from the experimental tensile tests were very similar in specimens of the same direction, values from one specimen of each direction (L1 and T1) were chosen to obtain the true stress - true strain curves and the curves using Swift's Law. As seen in figures 3.10 and 3.11, the proposed Swift curves adjust to the true stress - true strain curves only in the plastic region, ignoring the existence of the yield plateau.

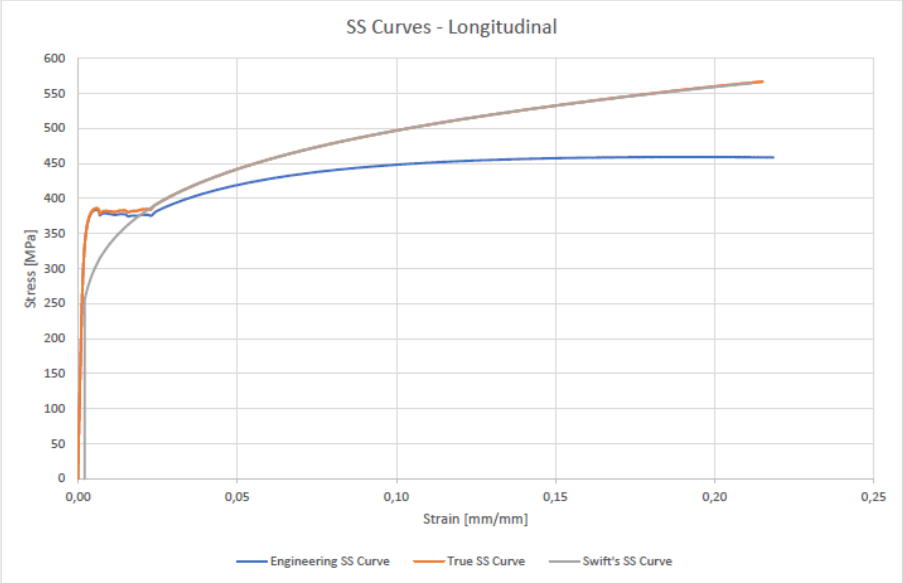


Figure 3.10: Comparison of stress-strain curves between the engineering curve, true curve and Swift's hardening law curve referring to the longitudinal direction.

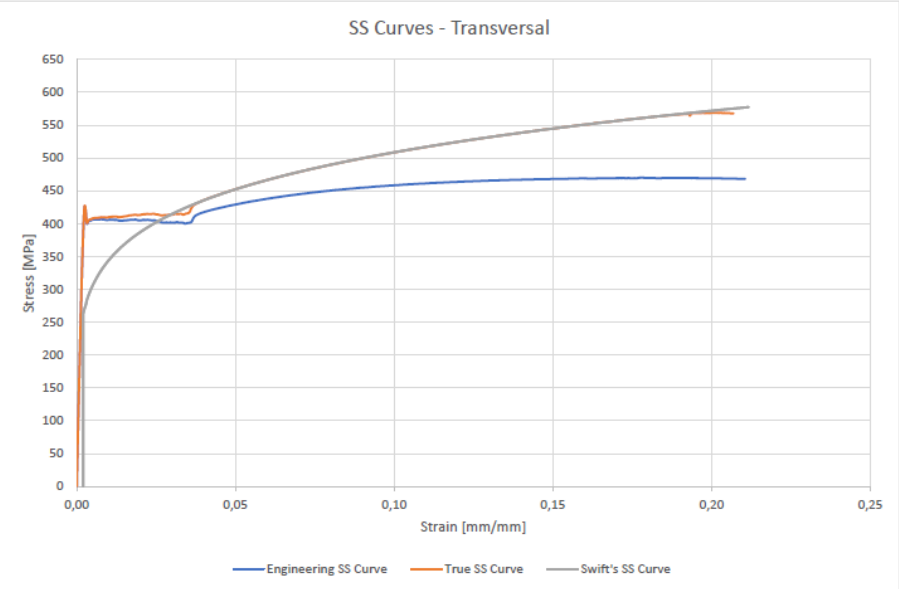


Figure 3.11: Comparison of stress-strain curves between the engineering curve, true curve and Swift's hardening law curve referring to the transversal direction.

3.2.2 Material microstructure analysis

The cold roll forming is characterized by the sheet metal deformation below the recrystallizing temperature of the material. Therefore, the material microstructure becomes deformed mostly in regions such as corners where an high strain is expected to be applied. One question that could arise is if some local material failure (cracking or microcracking) could occur in those corner locations. Therefore, in this section some samples were cut in the corners of the Z-rail profile and analysed using optical microscopy.

The microstructure analysis was performed in 5 samples of the Z-profile cross section. The samples were saw cut from the areas numbered in figure 3.12, the locations 1, 2, 3 and 4 were chosen for being the bending zones and location 5 for being the furthest from the bending zones.

The samples were mounted in resin and polished using silicon carbide abrasives with the following grit size: 360, 600, 1000 and 1200. The final polishment was performed with diamond abrasives of 3μm and 1μm. The analysis was executed using an optical microscope with a digital camera.

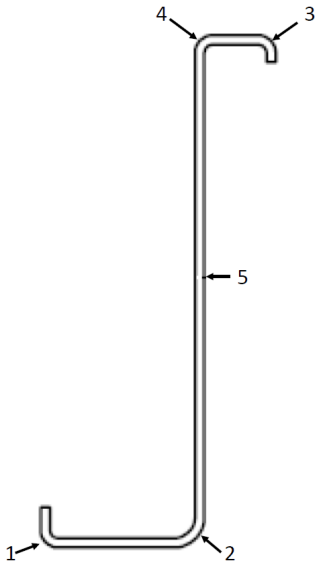
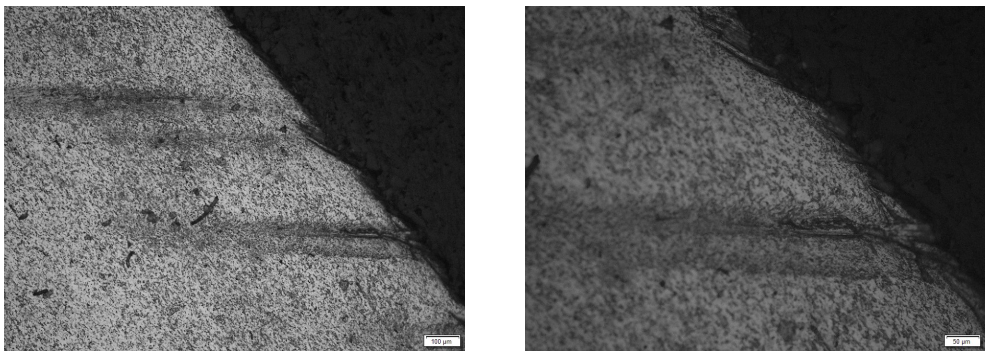


Figure 3.12: Locations of the samples cut from the Z-profile for the microstructure analysis.

Point 2

The material extracted from the point 2 has an interior radius of 4.5 mm and an exterior radius of 8.0 mm. According to figures 3.13, no cracking was observed. The micrographs quality was not the best since some scratches from the material saw cut were not fully removed polishing.



(a) (b)

Figure 3.13: Images obtained from the microstructure analysis of material from point 2, outer radius region.

Also, the region of the interior radius did not show any signs of cracks, the surface appearing smooth (figure 3.14).

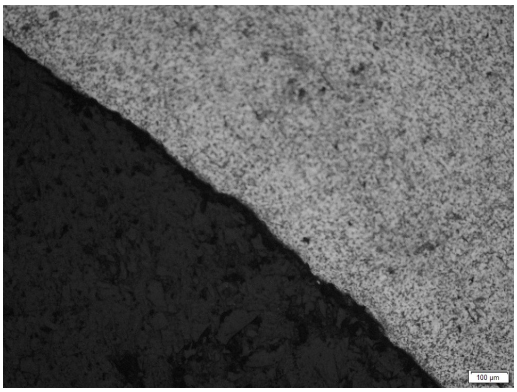
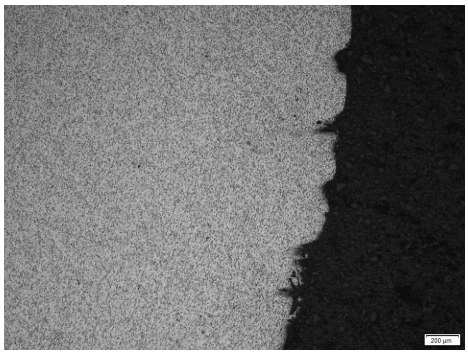


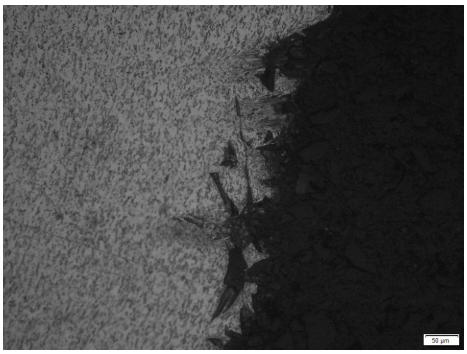
Figure 3.14: Point 2, interior radius: no sign of cracks.

Points 1, 3 and 4

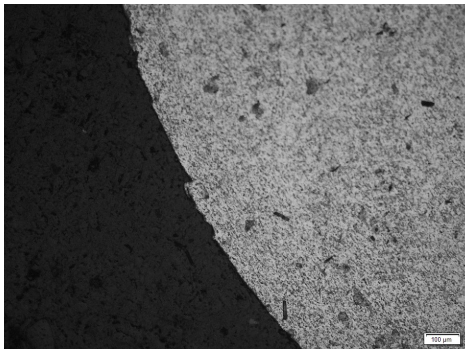
The samples extracted from the points 1, 3 and 4 have an interior radius of 3 mm and an exterior radius of 6.5 mm. It was possible to verify (see figures 3.15) that the exterior radius shows some important surface roughness but, from this study, it is not clear if that roughness is a result of the cutting process damaging of if it is original from the profile production.



(a) Point 1, exterior radius.



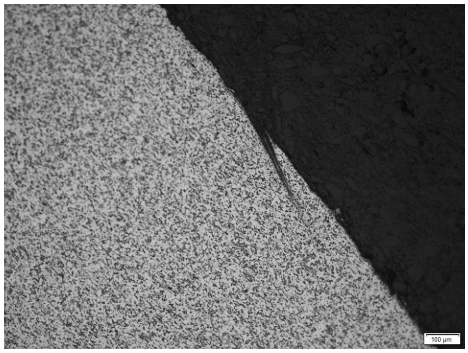
(b) Point 1, exterior radius.



(c) Point 3, exterior radius.



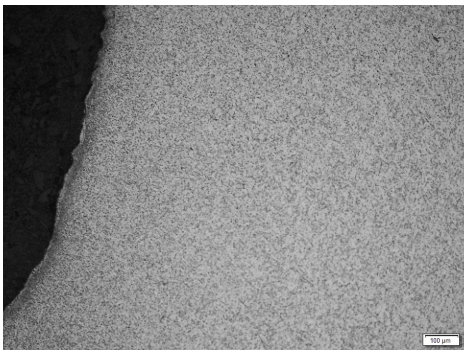
(d) Point 4, exterior radius.



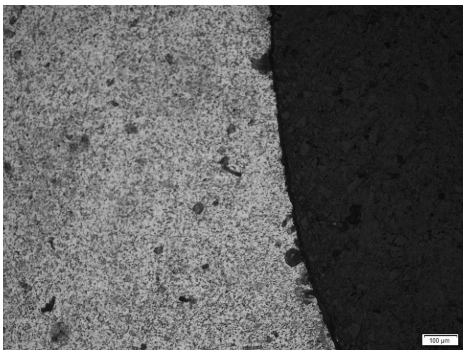
(e) Point 4, exterior radius.

Figure 3.15: Images obtained from the microstructure analysis of material from exterior radius of points 1, 3 and 4.

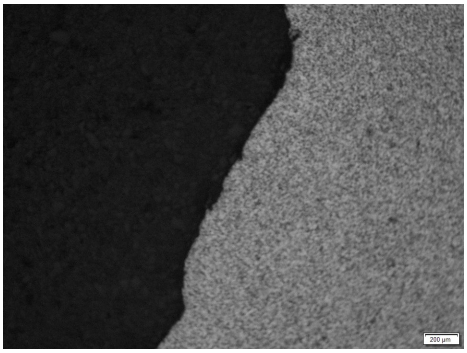
Similar to point 2, the surfaces on the interior radius (see figures 3.16) of points 1, 3 and 4 appear smooth with no sign of crack initiation.



(a) Point 1, interior radius.



(b) Point 3, interior radius.



(c) Point 4, interior radius.

Figure 3.16: Images obtained from the microstructure analysis of material from point 1, 3 and 4: smooth surface appearence.

Point 5

Figure 3.17 shows the image taken from the sample extracted from the middle of the web in point 5. The longitudinal lines visible are likely related to the rolling involved in the manufacturing process of the steel sheets that leads to elongated grains with a defined orientation (rolling direction) and explain the anisotropy verified in the tensile tests between the two directions.

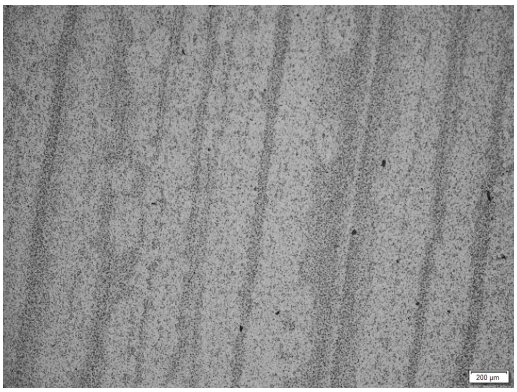


Figure 3.17: Sample extracted from point 5 exhibits longitudinal lines hut no visible signs of crack initiation.

Although the microstructure analysis revealed the existence of cracks in the exterior radius of the material, the process used to cut the samples from the profile could have caused some of this surface damage. However, the same effect was not observed in the inner radius which strengthens the idea that the surface quality of this profiles is poor at the outer surface corners. For that reason, in future works is advisable to use a non-invasive methodology to analyse the surface of the material such as scan electron microscopy or remove possible damage of the samples from the saw cut.

3.3 Geometrical Analysis

Geometrical characteristics of the profile were evaluated using two experimental methods: a contact method (LVDT) and an optical one (GOM).

3.3.1 LVDT Analysis

Shape defects were measured on a Z-section profile using a LVDT. The profile was mounted in the table of a milling machine and a LVDT was gripped to the head of the milling machine (see figures 3.20). Two metallic cylinders placed in the ends of the profile were used as a base (see figures 3.18). In one of the ends the profile was held on to the cylinder having the full surface of the large flange in contact with this element; in the other end, due to the prevailing torsion of the rail profile, the large flange contacted the cylinder in a single point. The profile was aligned along the milling machine table's longitudinal direction.



(a) Profile held on to the first cylinder. (b) Profile supported in the second cylinder.

Figure 3.18: Experimental setup and supports used to place the profile.

Measurements of 10 different paths were taken (Figure 3.19) using a LVDT with a range of 8 mm and the results were acquired using a SPIDER system and saved in a computer. This test revealed the variations and distortions of the surfaces along each path.

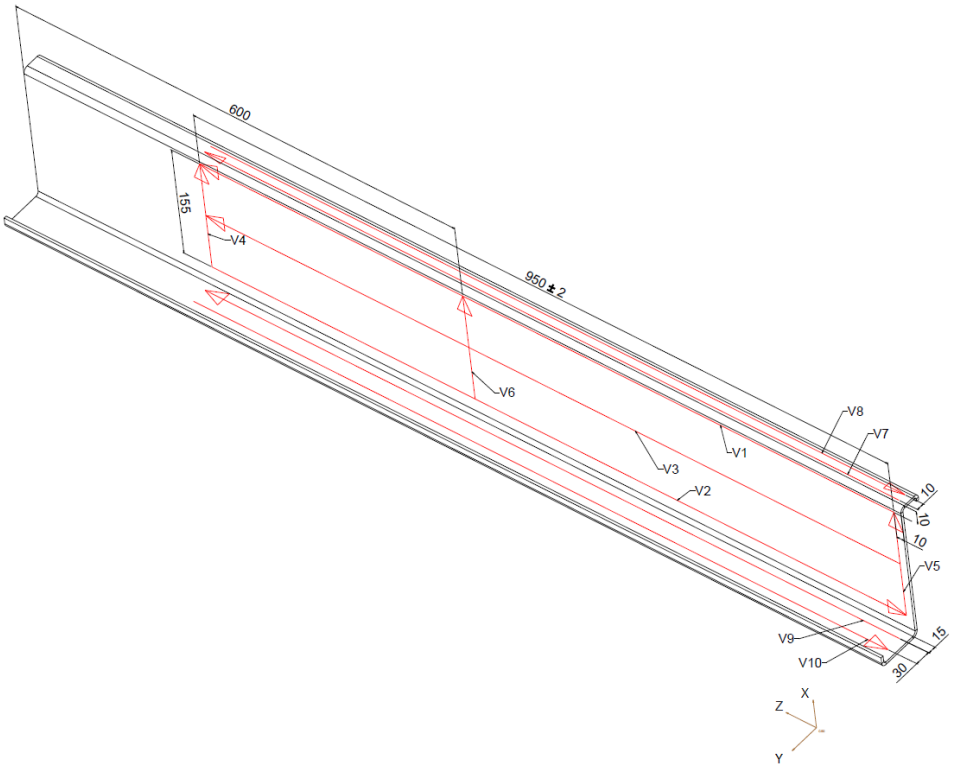
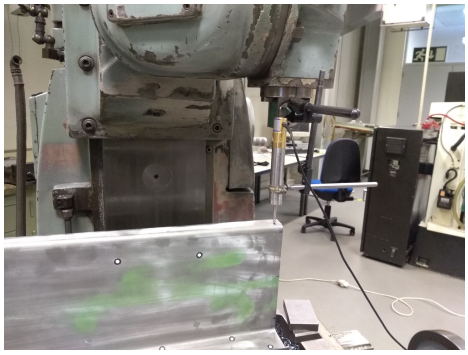


Figure 3.19: Paths used in the LVDT analysis.

The experimental setup can be seen in Figures 3.20a and 3.20b.



(a) LVDT attached to the head of the milling machine

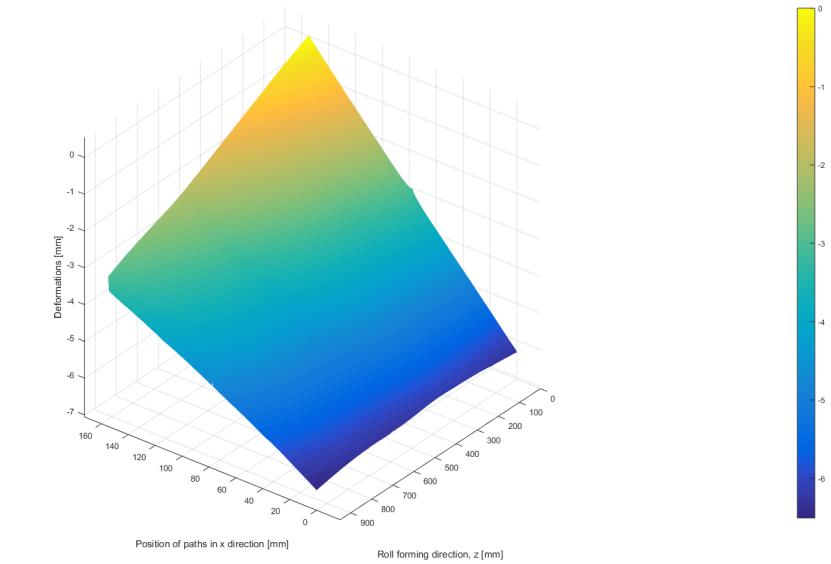


(b) Measurements of the LVDT along the paths.

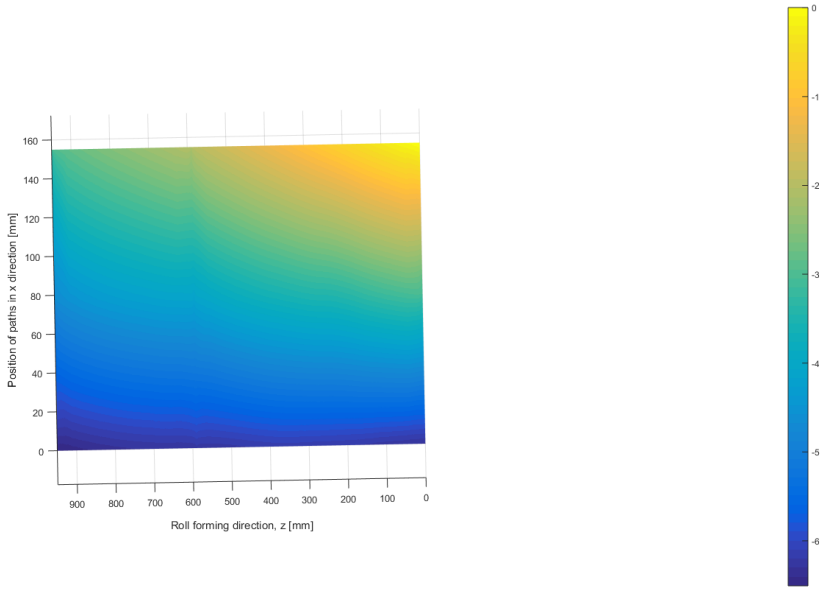
Figure 3.20: Experimental setup of shape deffects measurement with a LVDT.

For the paths V1, V2, V3, V7, V8, V9 and V10 the movement of the table occurred at a velocity of $800mm/min$. For the paths V4, V5 and V6 the velocity was $330mm/min$. The LVDT registered the values of displacement with intervals of $0,1s$. Knowing the velocity in each path and the starting and finishing points, it is possible to locate each measurement on the Z-section profile. Figures 3.21 - 3.23 show the experimental results.

Concerning the web, figures 3.21 show that deformation increases along the roll forming direction and it is higher in points closer to the large flange. The small flange reveals that deformations vary similarly in both measured paths, with deformations increasing along the roll forming direction. In the large flange, the deformation also increases along the roll forming direction and is higher for points furthest from the web.



(a)



(b)

Figure 3.21: Results with LVDT analsysis for the web using the values measured in paths V1, V2, V3, V4, V5 and V6 (displacements shown in mm).

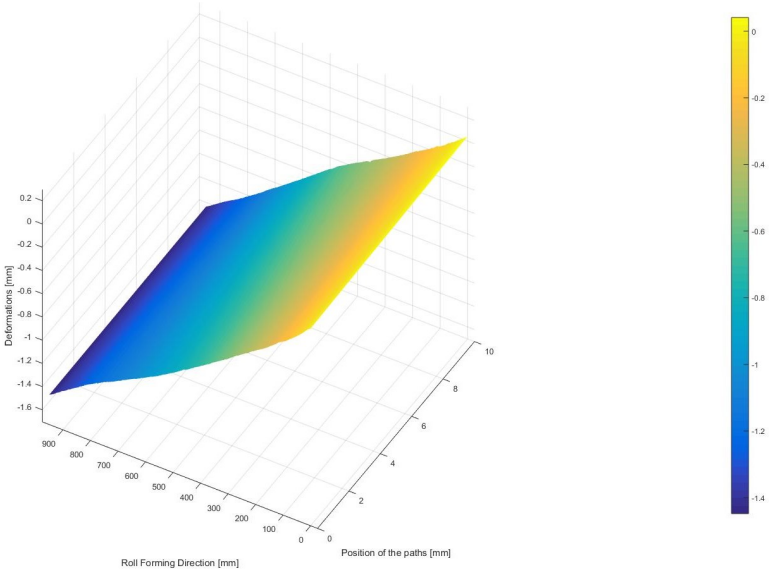


Figure 3.22: Results with LVDT analsysis for the small flange using the values measured in paths V7 and V8 (displacements shown in mm).

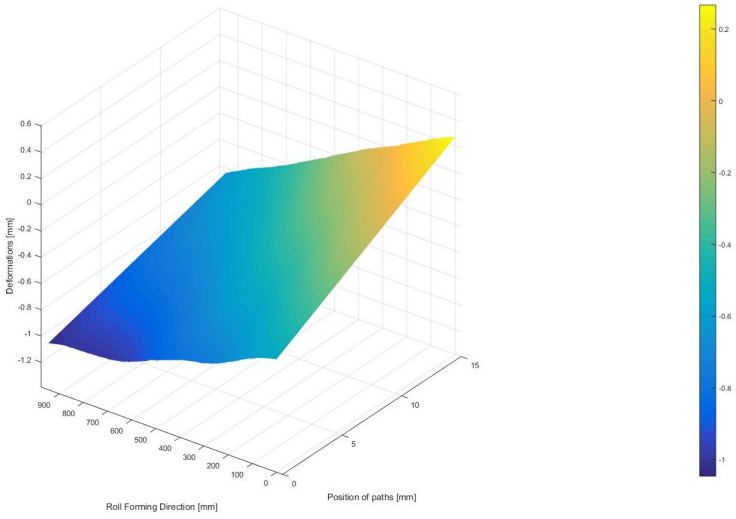


Figure 3.23: Results with LVDT analsysis for the large flange using the values measured in paths V9 and V10 (displacements shown in mm).

However, the results presented above do not take into consideration the misalignments in the placement of the profile. It would be necessary to determine those misalignments and exclude them to isolate the true distortions of the structure. In order to minimize the influence of these misalignments in the results, the scatter points collected were fitted to planes through a polynomial regression. The difference between the planes obtained and the location of the points can give a more truthfull information concerning the distortions of the profile. The data regarding the deviations for each section studied is presented in figures 3.24 - 3.26. In the web, deviations have maximum values in both ends of the profile as expected due to the flare in and flare out effect. The maximum amplitude of deviations in the web is, approximately, 1,50 mm. From the data collected, the small flange does not present any significant deviations from the plane created. Concerning the large flange, figure 3.26 shows that the peaks of deviation from the plane generated also occur in both ends of the profile having a maximum amplitude of 0,2 mm.

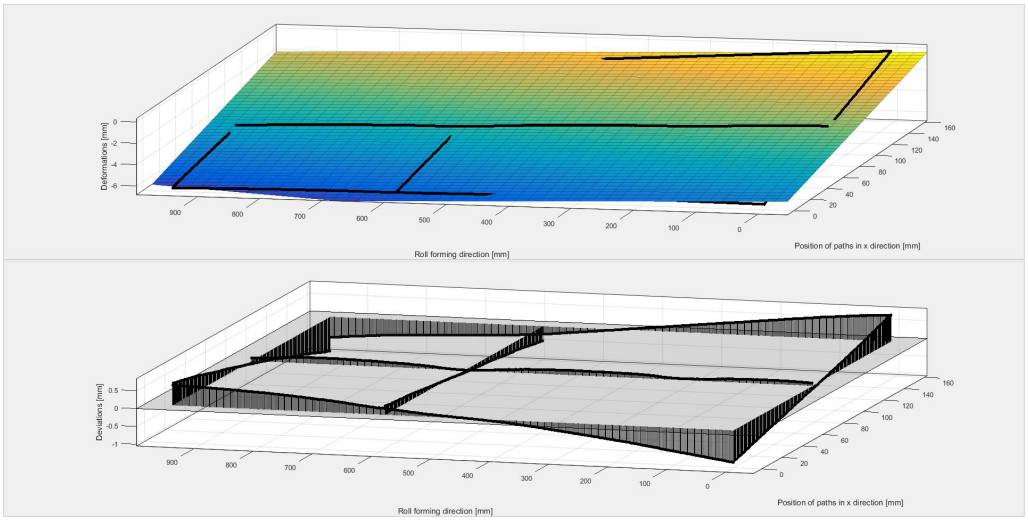


Figure 3.24: Comparison of the data points collected from the web region with the LVDT analysis with a plane created through polynomial regression. Deviations from the plane are presented.

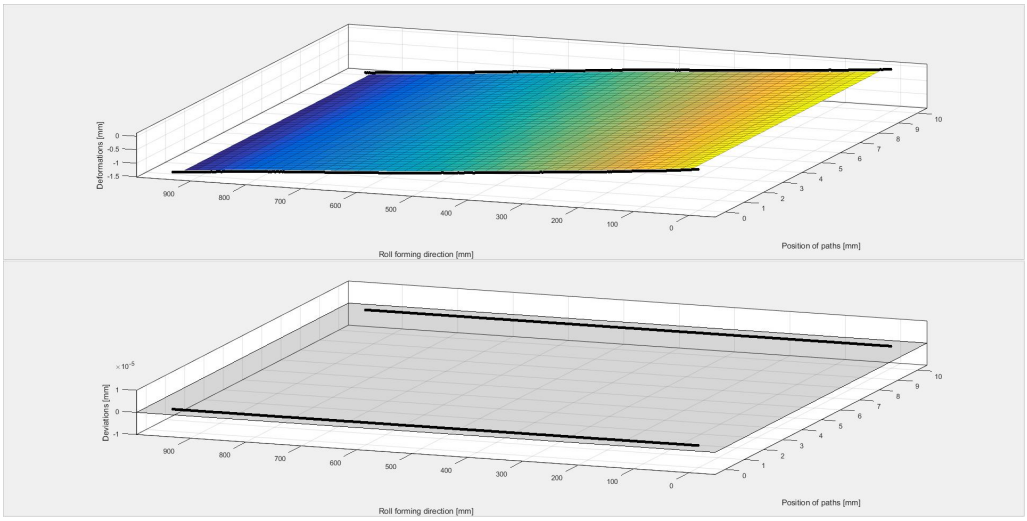


Figure 3.25: Comparison of the data points collected from the small flange with the LVDT analysis with a plane created through polynomial regression. Deviations from the plane are presented.

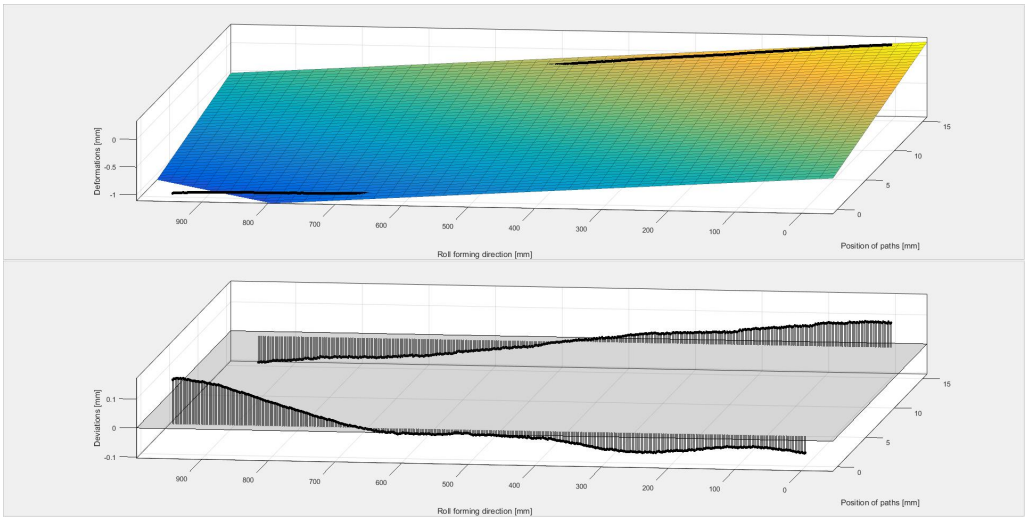


Figure 3.26: Comparison of the data points collected from the large flange with the LVDT analysis with a plane created through polynomial regression. Deviations from the plane are presented.

3.3.2 GOM Analysis

Analysis of the profile geometry was also performed using an optical method. This experiment was carried out at INEGI using GOM Inspect 2017, a 3D technology that inspected the Z-section profile by measuring all the surfaces in a three-dimensional analysis. The results of this experiment are processed by the machine software which compares the results with the nominal CAD geometry (results are shown in figures 3.27 - 3.30). It is important to notice that LVDT measurements were made for 950 mm and GOM analysis was performed for the full length of the profile (1200 mm), therefore the magnitude of distortion are not expected to have the same value.

It is verified that, as expected, distortions increase with the proximity to the ends of

the profile (see figure 3.27) due to the release of residual stresses that occur during the final cut of the rail (flair in and flair out). Both geometric analysis show that the web critical regions for deformation are the ones closer to the flanges and placed in both ends of the profile. The GOM analysis revealed that in the small flange, deformations are increasingly negative along the roll forming direction. Concerning the large flange, both analysis show that for points further from the web the deformation is higher.

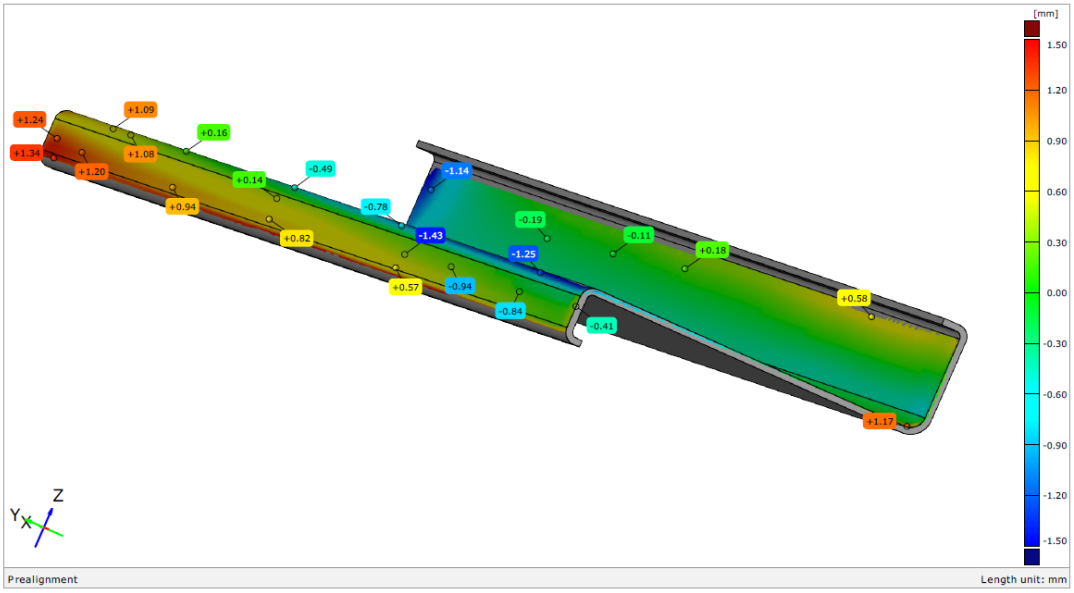


Figure 3.27: Results of the GOM analsysis, displacements (in mm) in the flanges .

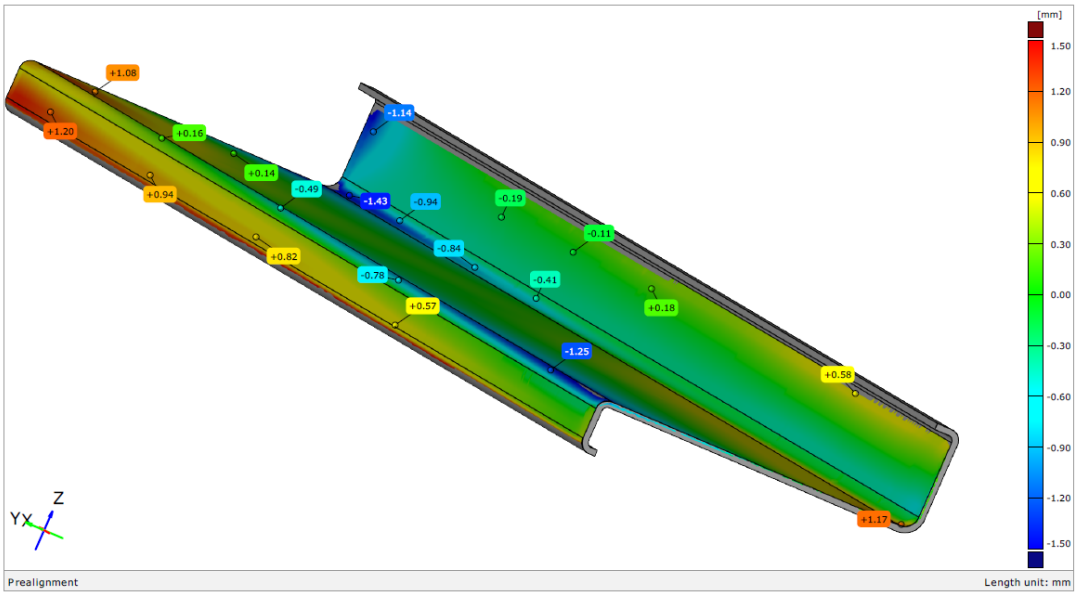


Figure 3.28: Results of the GOM analsysis for the Z rail profile (displacements shown in mm).

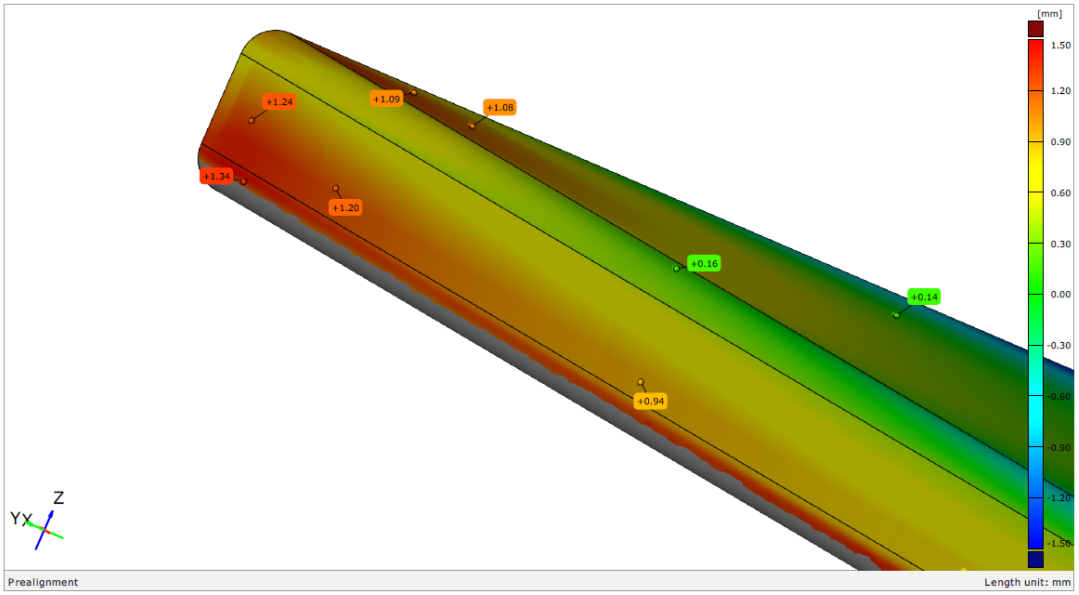


Figure 3.29: Results of the GOM analsysis, small flange with displacements shown in mm.

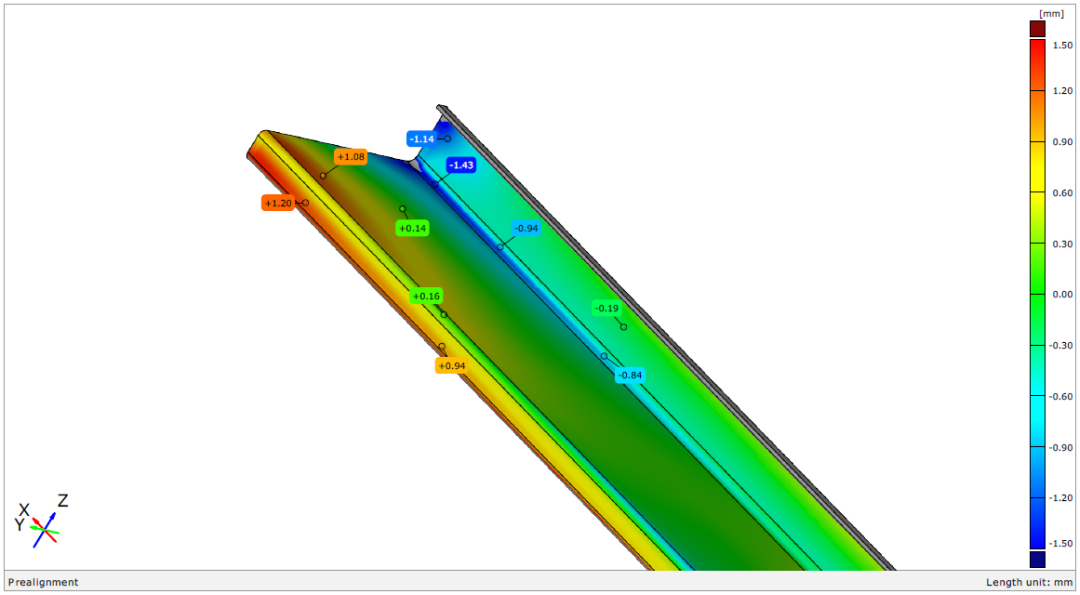


Figure 3.30: Results of the GOM analsysis (displacements shown in mm).

Chapter 4

COPRA FEA Simulations

The following chapter presents numerical simulation models generated for the Z-section profile using COPRA® FEA RF package. The material model, the results and conclusions drawn from the simulations will be presented. The main goal of this chapter is to study the influence of the roll forming process on three-dimensional geometry defects and on the residual stresses and strains of the profile. Parametric studies previously carried out by Martins [2018] will be used as reference for the definition of the simulation parameters. The results of a study on the influence of mechanical cyclic loads on local stresses of the profile as well as an estimative of the fatigue life of these components will also be included. One main aspect of this work which is distinctive from the work performed previously by Martins [2018] is the investigation of the influence of the kinematic hardening in the roll-forming and fatigue analysis. In the work carried out by Martins [2018] only isotropic hardening was explored.

4.1 Model definition

4.1.1 Modelling concepts

The forming rolls were modelled as rigid bodies while the strip was modelled as a deformable body. Due to the degree of difficulty to determine experimentally friction coefficients and since there are no available information in FASTCOLD project consortium about this parameter, friction was disregarded in the following simulations.

4.1.2 Geometry and flower

The roll design used was the same developed by Martins [2018] for her dissertation in COPRA® RF package and the simulation models were prepared automatically by the COPRA® FEA RF package from the roll design previously developed. The distance between stations is 400 mm and the strip length is 520 mm with a thickness of 3,5 mm. The forming line consists of thirteen stations (figure 4.1) and the flower diagram can be seen in figure 4.2.

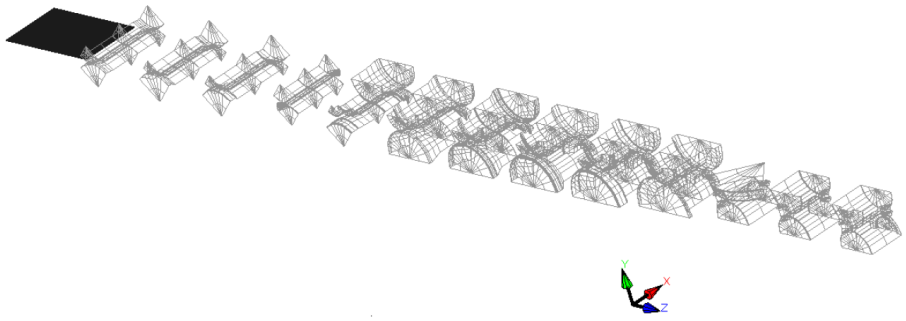


Figure 4.1: Stations and rolls used in the simulation of the Z-section profile [Martins, 2018].

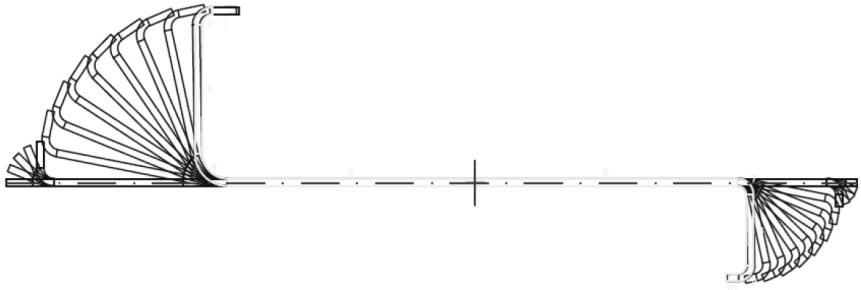


Figure 4.2: Flower diagram of the Z-section profile [Martins, 2018].

The standard global coordinate system used was:

- x for the horizontal direction perpendicular to the sheet direction;
- y for the thickness direction in the flat sheet (vertical);
- z for the sheet travel direction (roll forming direction).

4.1.3 Boundary conditions

Boundary conditions were used to prevent displacements in the x and y-directions of the last three nodes in the middle of the profile (see figure 4.3) in order to avoid strip rigid body motion. Only three nodes are selected to allow the movement of the strip in the remaining ones. In the end of the simulation, those three nodes will be cut off. These specific nodes were selected by default as a result of DataM previous experiments that proved that this location has the least influence in the roll forming process.

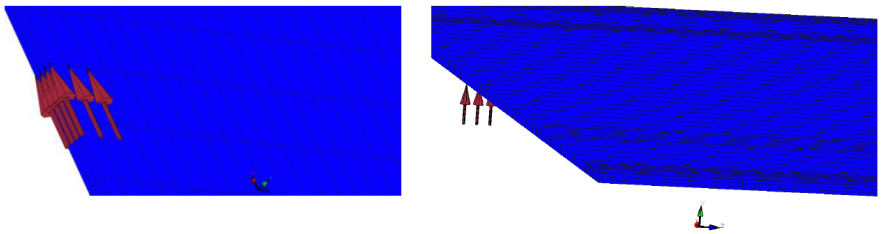


Figure 4.3: Boundary conditions in x and y-directions applied in three nodes in the middle of the tail end of the profile [Martins, 2018].

In industrial applications of the roll forming process, the strip is usually provided in a coil and the profile is cut in the end of the process to the required length. To assure a realistic simulation, all the nodes in the front and tail end were also restricted along the z-direction to simulate a continuous strip of material and assure that the strip maintains the same length.

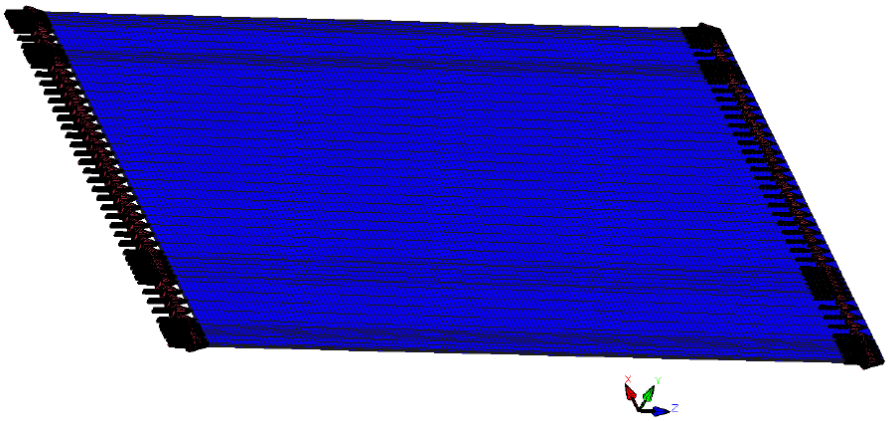


Figure 4.4: Boundary conditions to restrain the nodes in the extremities along z-direction to simulate the continuous existence of the strip [Martins, 2018].

After the cutting process, the strip must also be prevented from moving freely in space thus, Fs boundary conditions were also applied meaning both ends of the strip are locked along all directions.

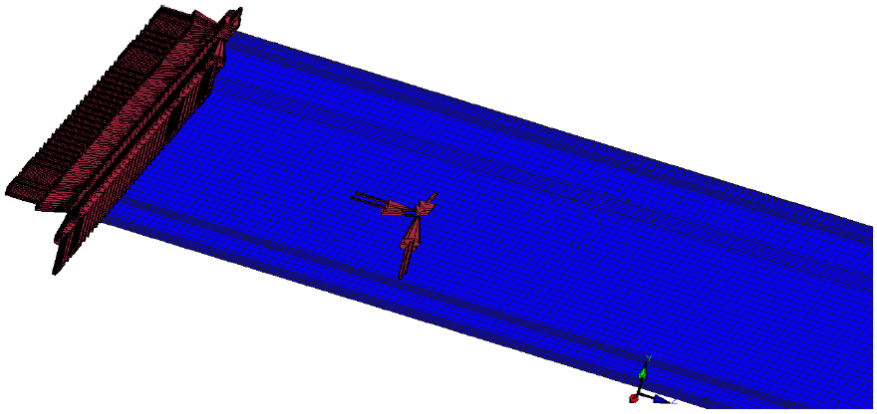


Figure 4.5: Boundary conditions related to the free cut process [Martins, 2018].

4.1.4 Element type

The element type chosen was element type 7 which is an eight node hexahedral solid element with trilinear interpolation. As stated by Ferreira [2016], this element is commonly used by DataM in their simulations because their accumulated experience has allowed them to understand that this element type provides a good representation of the roll forming behaviour of steel materials. DataM also concluded from previous studies that the use of shell elements is not appropriate for this type of analysis considering that the material behaviour through thickness is not uniform and must be represented with high accuracy. Eight-point Gaussian integration is used to determine element stiffness [Ferreira, 2016].

4.1.5 Mesh definition

Mesh definition was based on the parametric studies previously performed by Martins [2018]. In order to better compare and analyse the results with the ones obtained previously, the chosen mesh definition was the same used in the Z-section profile simulation and presented by Martins [2018] in her dissertation report.

The values used to define the mesh were the following:

- Number of subdivisions in straight entities of the section (for FEA calculation): 2,8;
- Number of subdivisions for arc entities: 1,8;
- Number of subdivisions in the rolling direction: 1,5;
- Number of elements along the thickness direction: 3.

This mesh definition results in a total of 29016 elements and can be seen in figure 4.6.

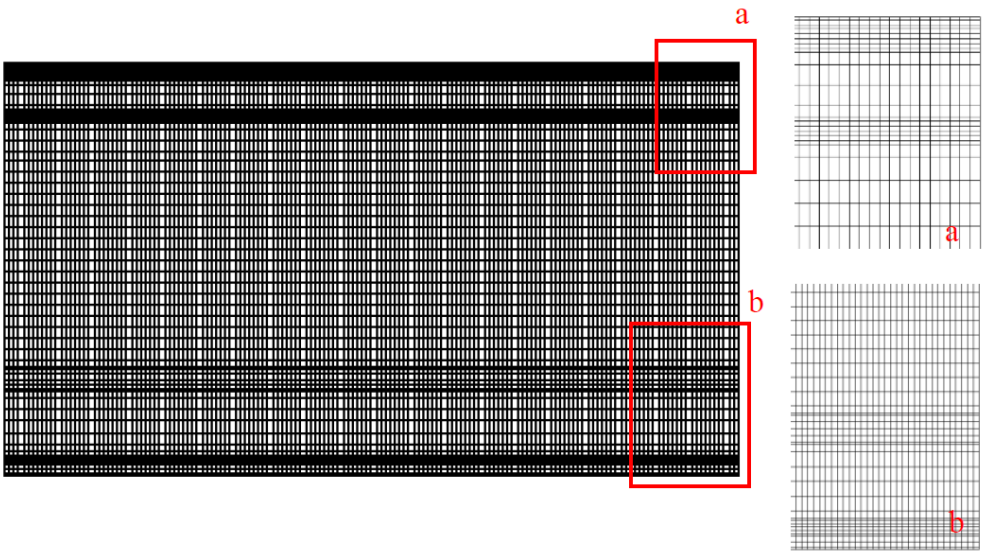


Figure 4.6: Mesh definition of the Z-section profile [Martins, 2018].

4.1.6 Material model

The effects of kinematic hardening will be the main subject of study. In order to do that, a comparison to the results published by Martins [2018] will be presented. The material used will be S350GD steel which was the material studied in the scope of her dissertation.

The material models for the Z-section profile were developed using the mechanical properties attained in tensile tests for S350GD. The profiles provided by Schäffer are, however, made of S355MC steel and that was the one analysed in the experimental work performed. Table 3.3 shows mechanical properties for both materials.

The values introduced for the elastic properties were: 210 GPa for Young's modulus and 0,3 for Poisson's ratio. The Von Mises yield theory with kinematic hardening was used to develop the model.

Since sheet metal industries usually use raw material in a coil, the sheet metal forming strategy used was the "coil" option which means that the forming process is continuous without any pre-defined length. With this option, the software assumes the model of a strip with infinite length to represent the continuous process. Because of this, boundary conditions on the z-direction are added to the model. To simulate the cut off that occurs in the process to produce the final product, the option "cutting (default 0.5*length)" was selected and the first and final quarter parts of the profile are inactivated when the workpiece leaves the final station. The cutting operation is responsible for stress relief that has to be taken into consideration in the numerical analysis.

4.2 Measurement of residual stresses along xx direction

For the measurement of residual stresses along xx direction of each element, five planes (figure 4.7) were created: plane i is at the front end of the profile, plane ii is located in the 20^{th} node counting from the front end, plane ii in the 40^{th}, plane iv in the 60^{th} and plane v on the tail end of the profile. For planes ii, iii and iv a top (yy=t/2) and a bottom (yy=-t/2) path located on the surfaces of the profile were considered in order to measure the residual stresses (figure 4.8). Path 1 is located in plane ii, path 2 in plane iii and path

3 in plane iv.

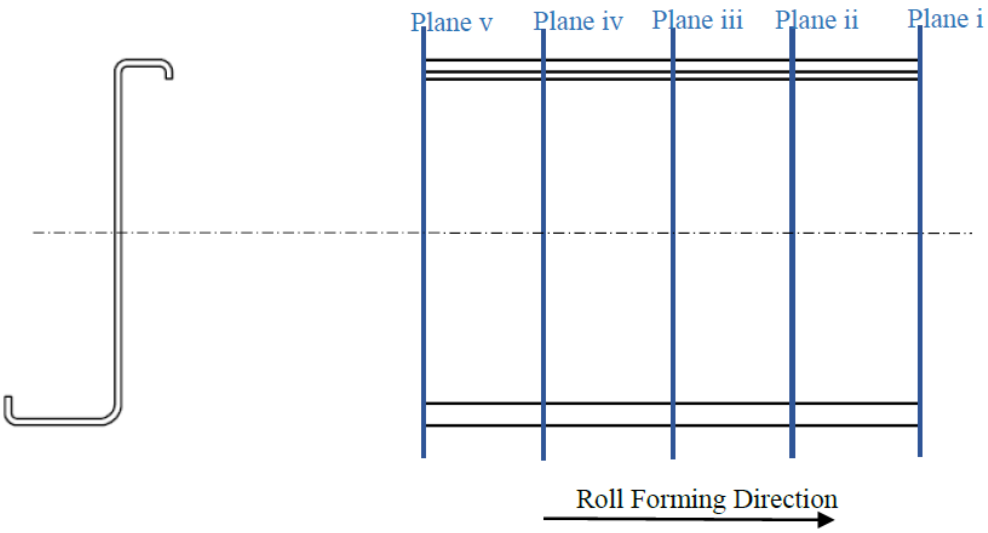


Figure 4.7: Location of the planes in the profile for residual stresses measurement [Martins, 2018].

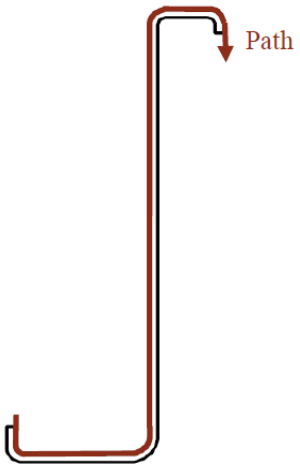


Figure 4.8: Representation of the top path [Martins, 2018].

To study the through thickness residual stresses along xx direction of each element, a curvilinear coordinate system that follows the elements along the bending trajectory was created. These stresses were measured in five paths of the large flange - web corner as shown in figure 4.9.

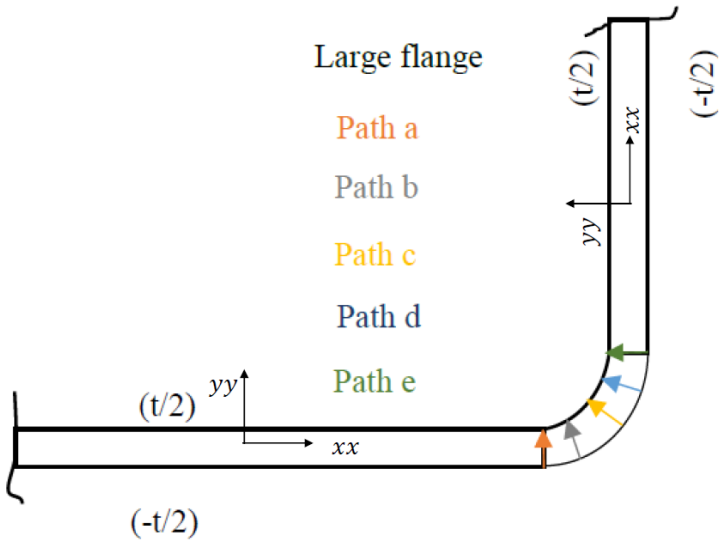


Figure 4.9: Location of the paths where through thickness residual stresses were measured [Martins, 2018].

4.2.1 Measurement of bow and springback

Longitudinal bow was measured in the middle of the web, in the bottom surface (-t/2) along the roll forming direction. Springback was measured in the large flange in the same five planes used for the residual stresses analysis. Springback was measured as an angular deviation.

4.3 Analysis of the effect of kinematic hardening

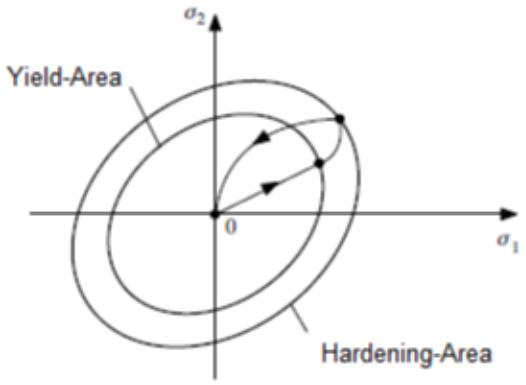
In this section, results of a numerical simulation using S350GD steel and kinematic hardening will be presented. A comparison to results previously obtained using the same material with isotropic hardening will be performed to understand the effects of the hardening rule on the results for stresses, strains and three-dimensional deffects after the cold-roll forming process as well as for fatigue life prediction.

In the plastic region, when a level of loading leads to a stress higher than yield stress, an increase in plastic strain corresponds to an increase of stress: hardening of the material. Hardening rules establish the conditions for a new plastic flow after the plastic state of the material has been reached.

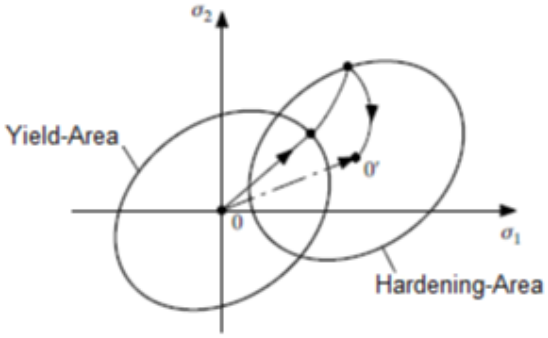
For isotropic hardening, the subsequent yield surface originated due to an increase in plastic deformation is an uniform expansion of the previous yield surface (figure 4.10a). The simplicity of this model is its main advantage, however some real aspects of material deformations like the Bauschinger effect cannot be reproduced with this model.

For kinematic hardening, the subsequent yield surface maintains its shape but translates in space (figure 4.10b). This model can represent the Bauschinger effect, a phenomenon that commonly occurs in materials subjected to cyclic loading.

The Bauschinger effect reveals the dependence of yield strength with the direction of loading. Figure 4.11 represents this effect: when a specimen is subjected to a tensile stress (higher than stress at yield) until point D is reached and, at this point, the load is removed, plastic strain corresponding to point G is verified; if a compressive stress is then applied,



(a) Isotropic hardening.



(b) Kinematic hardening.

Figure 4.10: Hardening models.

point D' is reached. The absolut values of yield strength for tensile (σ_{Y0}^T) and compressive (σ_{Y0}^C) stresses do not match, $\sigma_{Y0}^T > \sigma_{Y0}^C$ [Natal Jorge and Dinis, 2004].

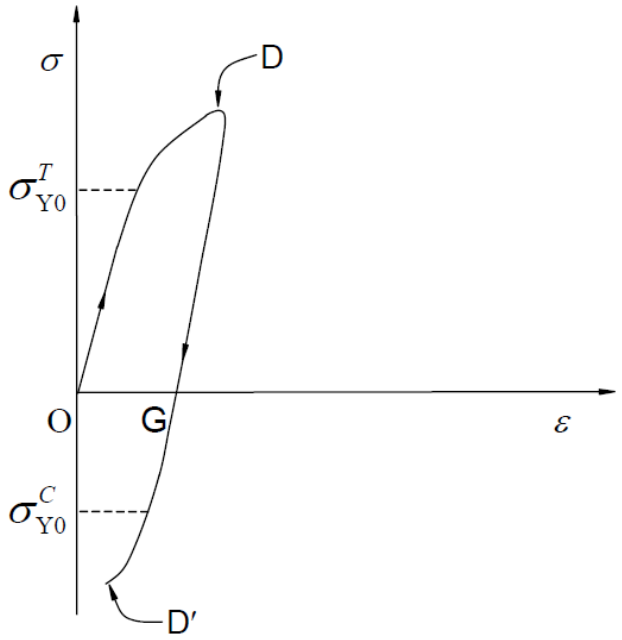


Figure 4.11: Bauschinger effect, σ_{Y0}^{T} is the tensile yield stress and σ_{Y0}^{C} is the compressive yield stress [Natal Jorge and Dinis, 2004].

4.3.1 Simulation results and discussion

Analysing the results concerning the distribution of transverse residual stresses along the xx direction of each element, it is verified in figures 4.12 and 4.13 that the magnitudes and distributions of residual stresses are similar for each path, for the top and bottom surfaces respectively.

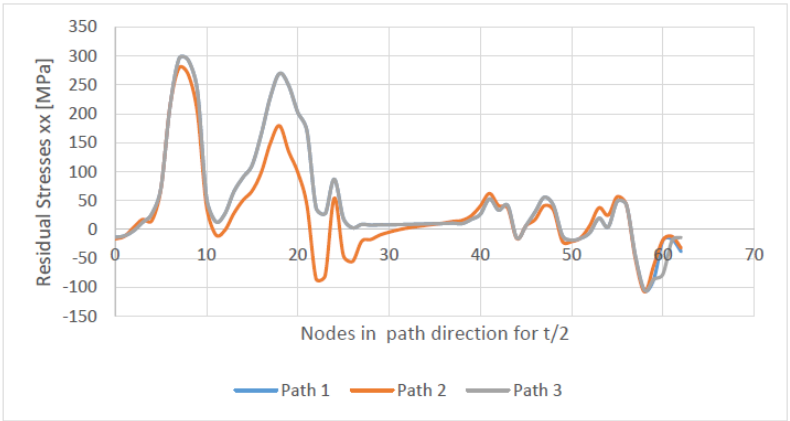


Figure 4.12: Comparison of results regarding residual stresses along xx direction in the top (t/2) surface between the 3 paths.

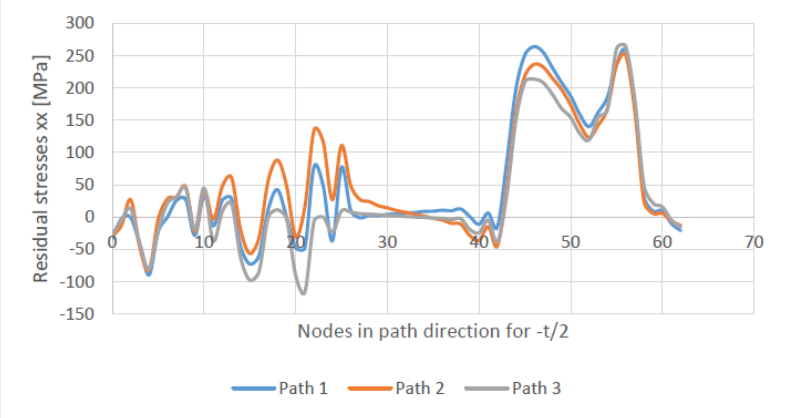


Figure 4.13: Comparison of results regarding residual stresses along the xx direction in the bottom (-t/2) surface between the 3 paths.

In the corner regions (pointed out in figure 4.14), residual stresses show a considerable increase in both surfaces. Considering that the large and small flange are bended in opposite directions, it is expected that they show opposite trends when it comes to residual stresses. In fact, the top surface of the large flange is under tension while the small flange is under compression. On the other hand, the bottom exhibits the opposite results of the top surface.

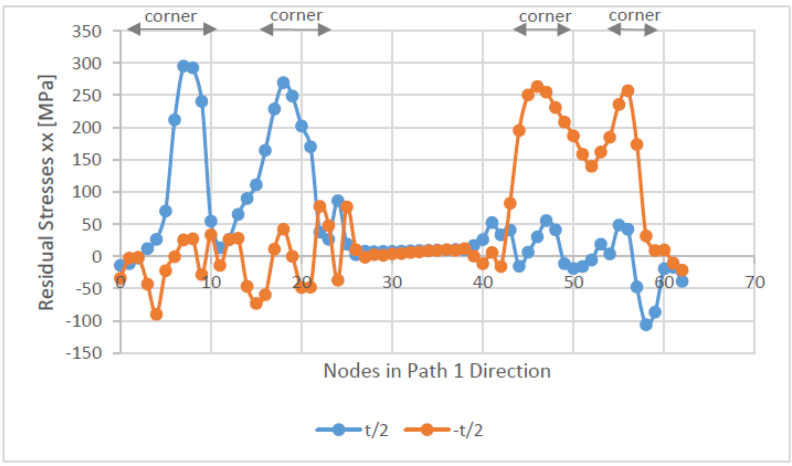


Figure 4.14: Comparison of results regarding residual stresses along xx direction between the top and bottom surface of path 1.

When comparing the results of this simulation with the one performed with isotropic hardening, we can see that there are no major variations in the results concerning the distribution of transverse residual stresses. The biggest difference appears on the magnitude of the stresses for the last corner (small flange) in the bottom surface (4.16). These results are somehow expected since the roll-forming configures a monotonic loading type, for which both hardening rules should provide same results.

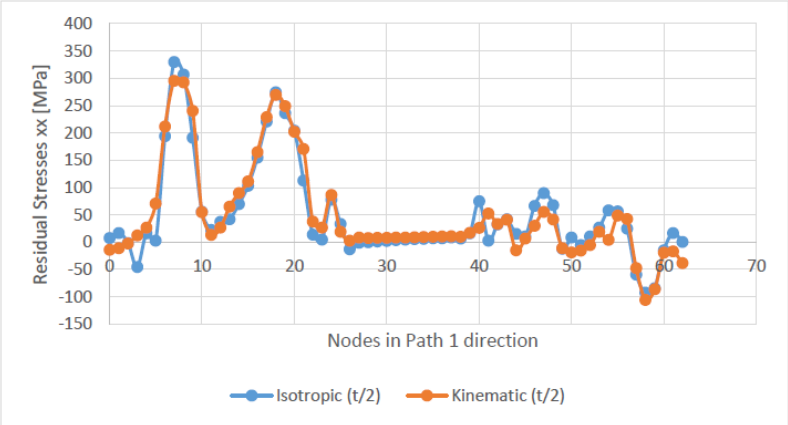


Figure 4.15: Comparison of results regarding residual stresses along xx direction for the top surface of path 1 between isotropic and kinematic hardening.

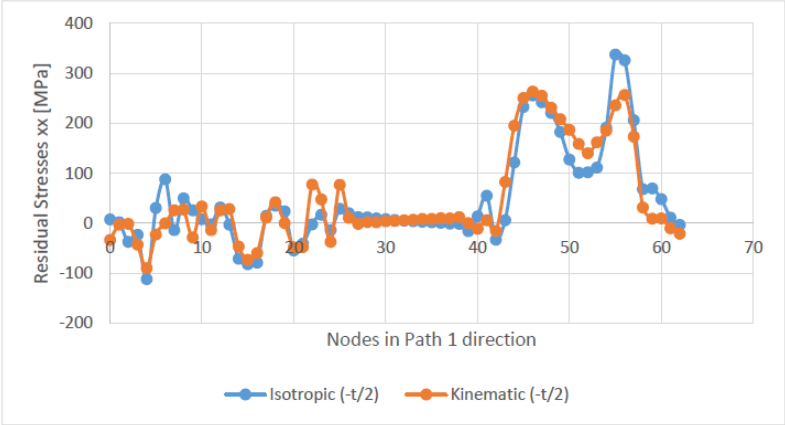


Figure 4.16: Comparison of results regarding residual stresses along xx direction for the bottom surface of path 1 between isotropic and kinematic hardening.

Plastic strains present similar trends to the residual stresses, with peaks appearing in the corner regions. When comparing the results between isotropic and kinematic hardening, plastic strains do not show any significant difference (figures 4.18 and 4.19).

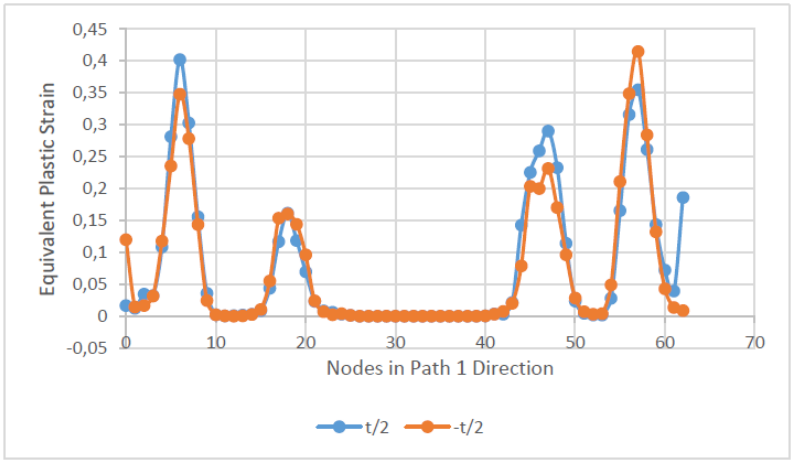


Figure 4.17: Comparison of equivalent plastic strain along xx direction between the top and the bottom surface for path 1.

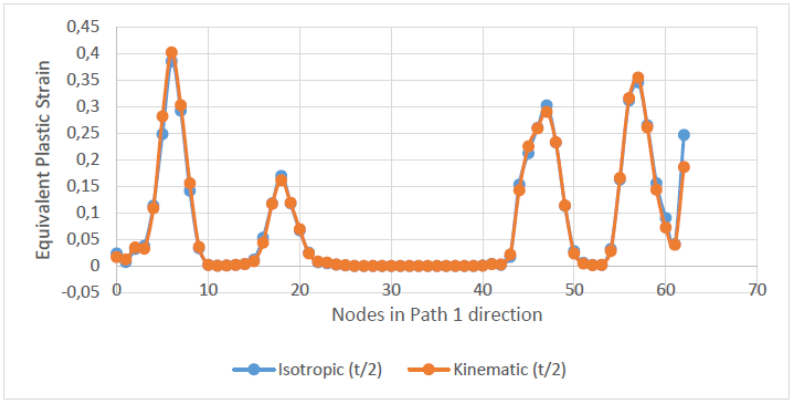


Figure 4.18: Comparison of equivalent plastic strain along xx direction for the top surface of path 1 between isotropic and kinematic hardening.

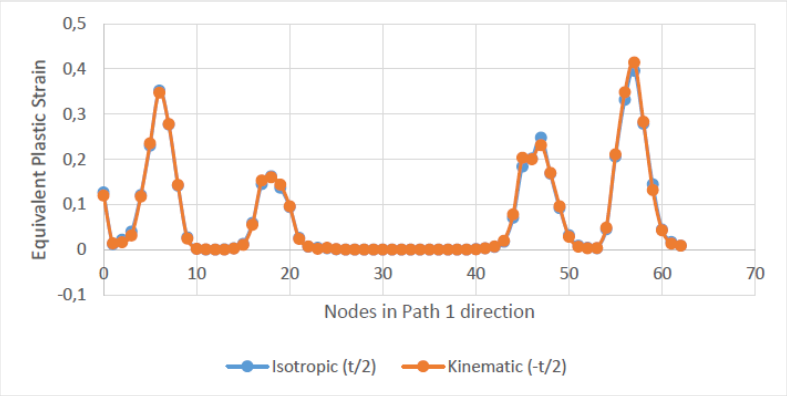


Figure 4.19: Comparison of equivalent plastic strain along xx direction for the top surface of path 1 between isotropic and kinematic hardening.

Regarding the results of through thickness residual stresses (see figure 4.20), the bottom and top surfaces are both under tension contrary to what was expected. However, "a less refined mesh could be a possible explanation, since the distribution of these stresses are widely dependent on the mesh size that is being used" [Martins, 2018]. Analysing the results from the simulation with isotropic hardening and comparing them to the one with kinematic hardening, for each path the results are very similar (figures 4.21a, 4.21b, 4.21c, 4.21d and 4.21e).

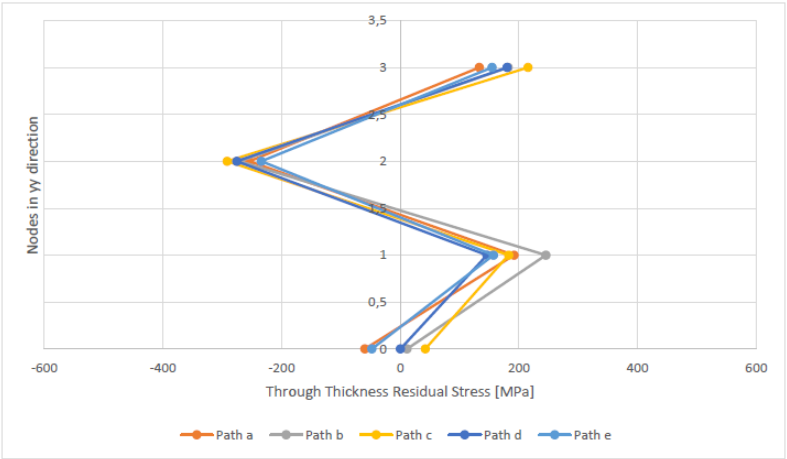
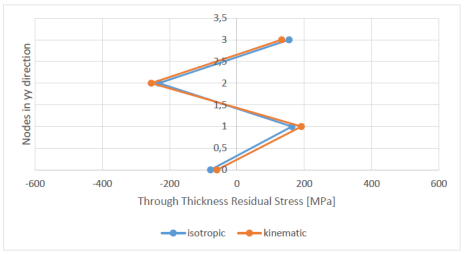
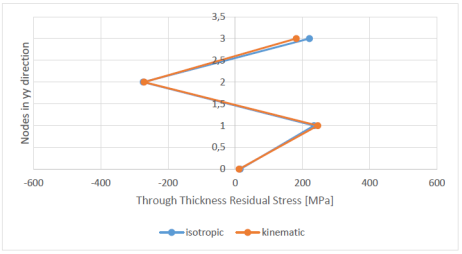


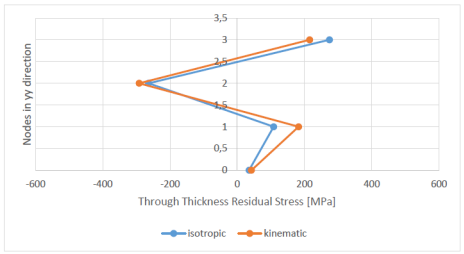
Figure 4.20: Through thickness resiual stresses between the 5 paths for plane ii.



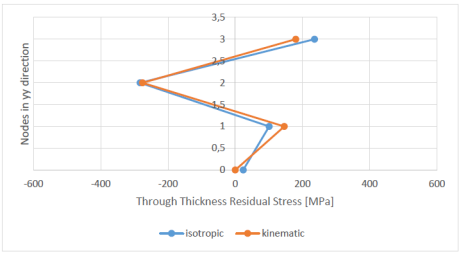
(a) Path a.



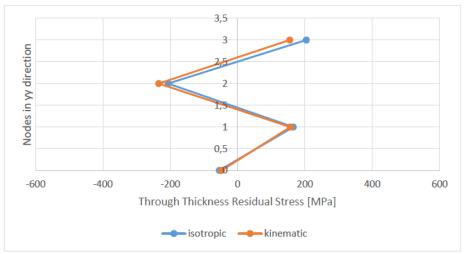
(b) Path b.



(c) Path c.



(d) Path d.



(e) Path e.

Figure 4.21: Comparison of through thickness residual stresses between isotropic and kinematic hardening for each of the five paths.

Figures 4.22 and 4.23 represent the edge position of the Z profile comparing the results between the two types of hardening. The large flange presents flare in both extremities and edge waviness is also present. The Z-section profile showed a different behaviour relative to flare when comparing the simulation using isotropic hardening with the simulation using kinematic hardening. The difference between the position of the ends is 0,69 mm for isotropic hardening and 0,22 mm for kinematic and the difference between minimum and maximum values of position in x is 0,84 mm for isotropic hardening and 0,49 mm for kinematic hardening.

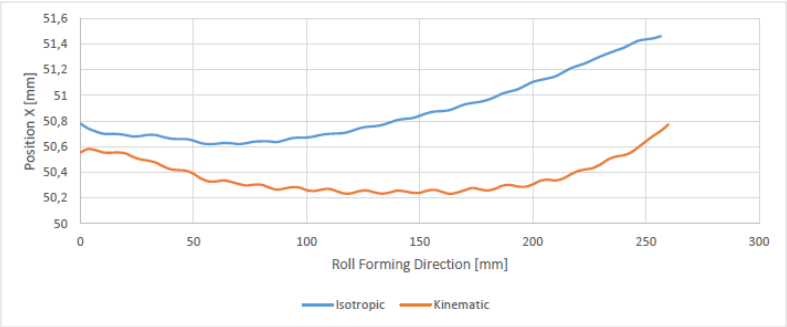


Figure 4.22: Edge position of the large flange for the top surface for both istropic and kinematic hardening.

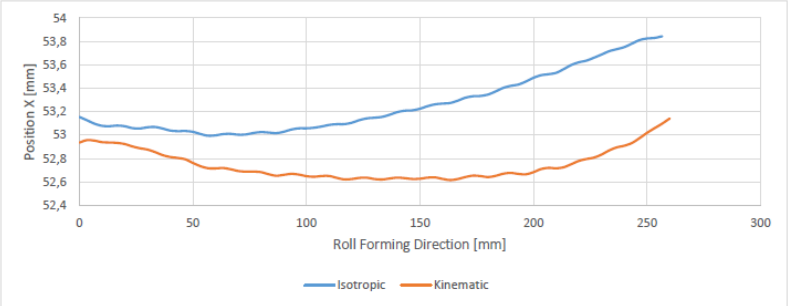


Figure 4.23: Edge position of the large flange for the bottom surface for both istropic and kinematic hardening.

Comparing the results for longitudinal bow in both simulations (see figure 4.24), the trends of both curves are very similar, however with isotropic hardening the maximum displacement verified was 1,37 mm while with kinematic hardening was slightly lower with 1,19 mm. Comparing this values with the results of the GOM analysis (see figure 3.28), it is verified that the numerical simulation provides greater values on longitudinal bow in the referred position.

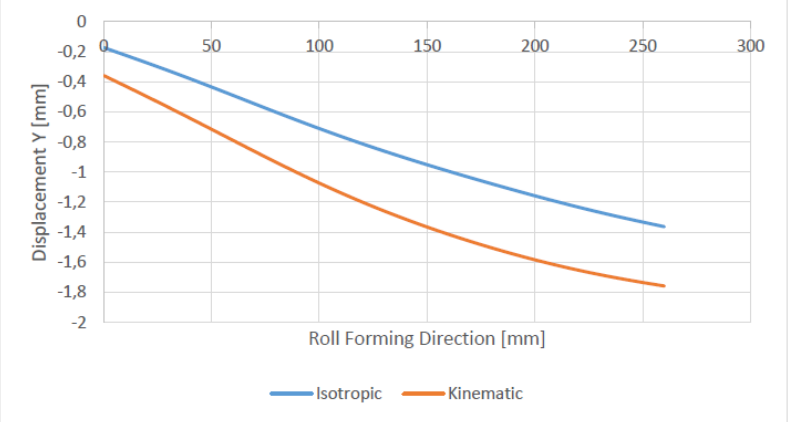


Figure 4.24: Comparison of longitudinal bow measured on the bottom surface of the web between isotropic and kinematic hardening.

The results for springback (see figure 4.25) were the ones that presented the most significant differences comparing the two simulations. The maximum springback occurred in different planes; using isotropic hardening the flange located in the tail end presented the most angular deviaton whereas with kinematic hardening the front end was the one with the higher springback value. Kinematic hardening also led to higher values of maximum springback.

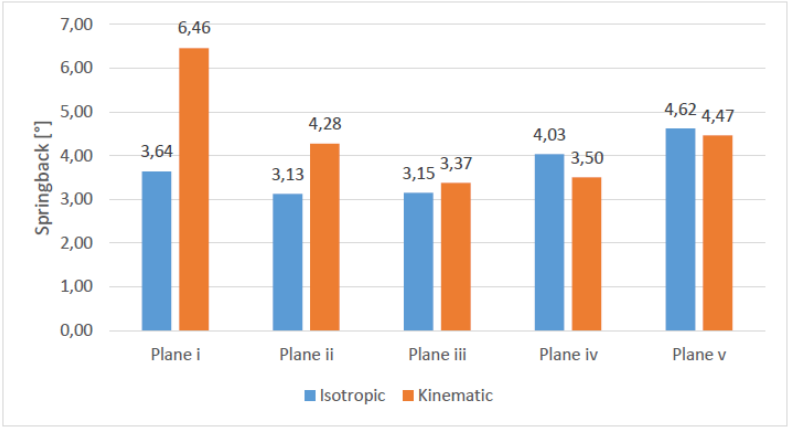
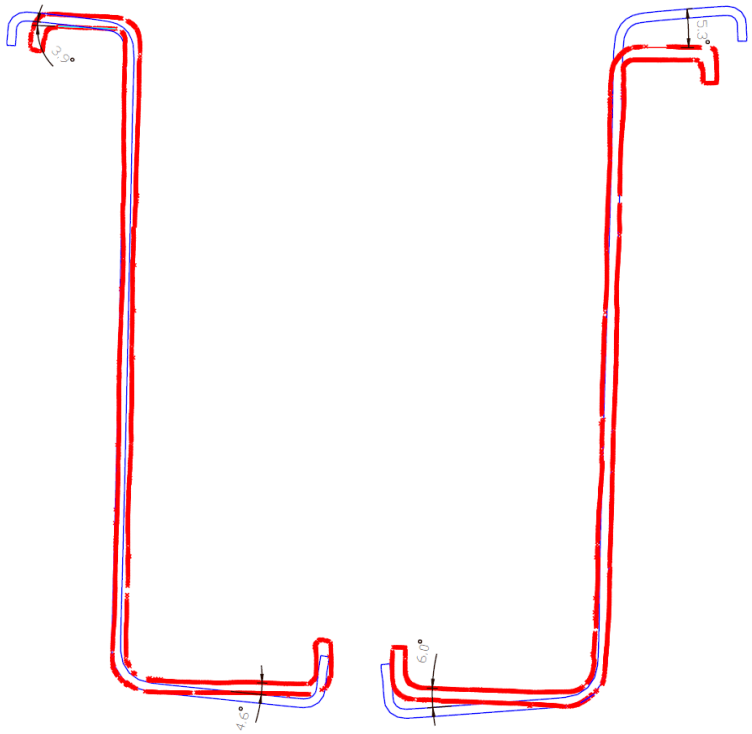


Figure 4.25: Comparison of springback in the large flange between simulations with isotropic and kinematic hardening.

In order to evaluate the results obtained, the shape of both ends of a profile sample provided by Schäffer were manually drawn. The drawings obtained were measured using a Mitutoyo optic system that collected various point coordinates, those coordinates were used to create a contour in AutoCAD. For the COPRA® RF model, two sections were made in order to get the geometry after the roll forming process in both ends of the profile as well. The first section is located in the 2nd node counting from the tail end and the second section in the 2nd node counting from the front end. Figures 4.26 show the geometry for both ends: the blue contour was originated from the simulation model and the red contour from the profile sample.

It is important to notice that the profile generated in the simulation model has a total length of 500 mm, while the sample has 1200 mm. It is verified that the software

overestimates the value of three-dimensional defects, that may be due to the fact that the roll forming machine used in the simulations is not the one used by Schäffer to produced the profiles. It is also noticed that, for the tail end, the differences shown are not only in angular deviations but also in the length of the web. For a strip length of 1200 mm, the values would be even greater.



(a) Front end. (b) Tail end.

Figure 4.26: Comparison between COPRA estimation for final geometry of the profile after the roll-forming process and the one verified in the profile samples.

4.3.2 Fatigue analysis of the Z-section profile

In order to understand the impact of kinematic hardening in fatigue life prediction, a similar analyis to what Martins [2018] did will be performed. External cyclic mechanical loads were applied to the cold roll formed profile to verify the resulting stress range and the critical area where fatigue cracks nucleation are more likely to occur. MSC Marc/Mentat Software was used to develop the finite element analysis and modifications to the initial model concerning boundary conditions, external loads, initial loads, etc. were also executed using the same software.

The loads applied to the profile were of 2 kN, 4,5 kN and 9 kN derived from information regarding the mass of the shuttle, given that the Z-profile rails have to withstand the passage of shuttles (empty or fully loaded).

The loads were applied in 6 nodes of the large flange (59^{th} to 61^{st} node counting from the front end of the profile) approximately in the middle of the length of the profile (neglecting the elements still in contact with the rolls) and as far as possible to the corner region so the worst scenario for fatigue damage could be simulated.

Each load was applied both in the top and bottom surfaces of the large flange. The increment used in this analysis was the one before the end cut of the profile (increment

Table 4.1: Information regarding shuttles and pallets typical masses [Martins, 2018]

Mass of the shuttle [kg]	Mass of the pallet [kg]	Number of wheels	Load for a wheel without pallet [kN]	Load for a wheel with pallet [kN]
300	1200	8	0,375	1,875

3540) and that is why part of the profile is still in contact with the rolls. This increment was chosen to make sure that the results were not influenced by the free cut. Nonetheless, when applying the boundary conditions all the elements still in contact with the rolls were deactivated.

The boundary conditions used were applied only in the web (not in the corner regions or flange), the elements of the extremities were restrained in the x, y and z directions. The large flange, as seen in figure 1.1a, is the region of the profile where the wheels of the shuttle move and, for that reason, have to be free.

The stresses in xx direction of the element coordinate system are the ones chosen to perform the fatigue analysis because the direction of these stresses are known for each position of the element and for each time increment. Using maximum principal values of stress would make the model a lot more complex since these values can change its direction several times. However, cold formed products applied in shelters with moving shuttles comprise multiaxial fatigue and transient loads.

The cyclic loads applied were composed of two cycles divided in 100 increments for a total time of 12.57 seconds (4π). The shape of the loads are governed by Eq. 4.1.

$$F(t) = a * sin(t - \frac{\pi}{2}) + a \tag{4.1}$$

where a is a constant that determines the maximum value of the applied load. Seing that the total load is the sum of the loads applied in each of the six nodes, for a total load of 2 kN $a = 166.667$, for 4,5 kN $a = 375$ and for 9 kN $a = 750$.

The first step taken to initiate the analysis was to identify the critical node where fatigue cracks might nucleate. Prelimary fatigue experimental tests performed by partners of the FASTCOLD revealed that crack initiation takes places at the corners regions as seen in figures 4.27. Four paths were created in the corner region (figure 4.28) where stresses are measured, these paths were defined by Martins [2018] that also identified this region as the critical one for crack nucleation through numerical studies. For loads applied in the top surface, the inner corner stresses are the only ones measured since the application of loads intensifies the tensile state of the inner corner and tensile stresses are detrimental to fatigue life of components (figure 4.29). Compressive stresses have the opposite effect and for loads applied in the bottom surface the same paths were used to measured the stresses but located in the outer corner, since for maximum load amplitudes the outter corner is under tension and the inner corner under compression (figure 4.30). Results were extracted and analysed at maximum load amplitude (steps 26 and 76 of the numerical simulation) and in the absence of load (steps 51 and 100 of the numerical simulation).



(a) (b)

Figure 4.27: Cracks in tested rails initiating in the inner corner regions.

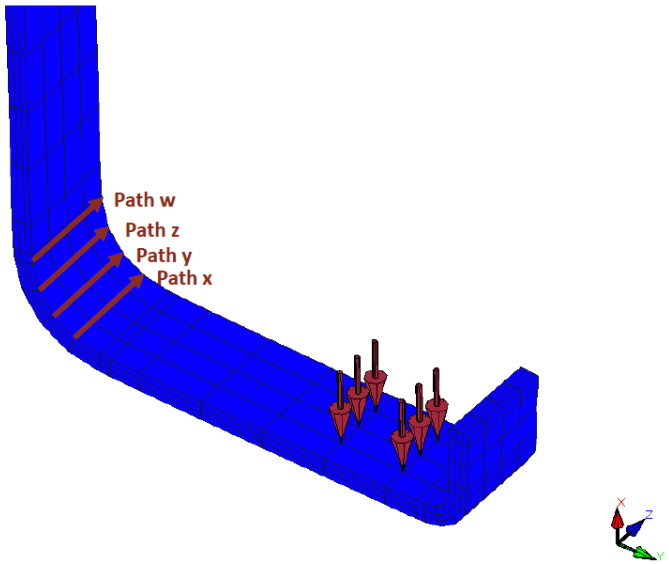
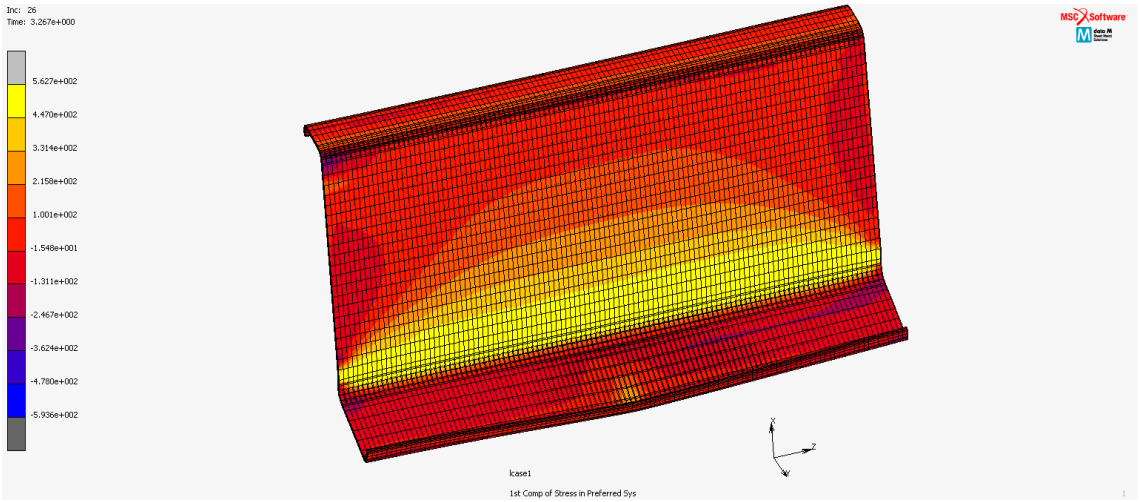
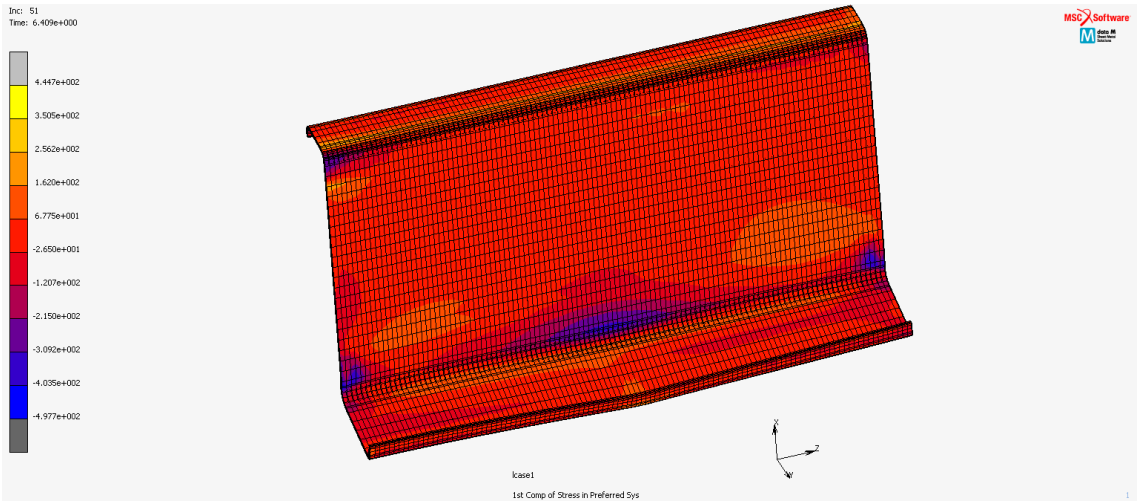


Figure 4.28: Paths used for fatigue analysis [Martins, 2018].

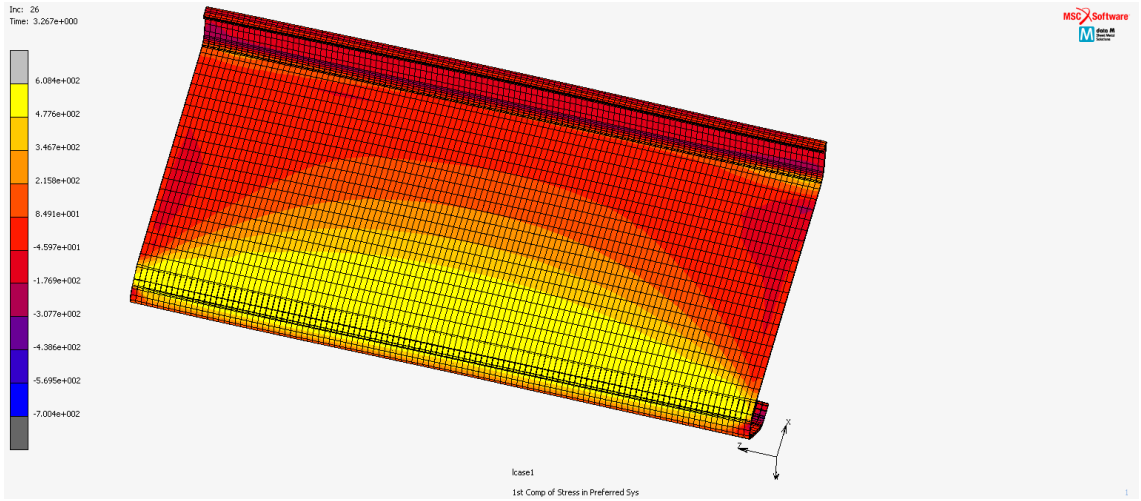


(a) Tensile stresses in increment 26.

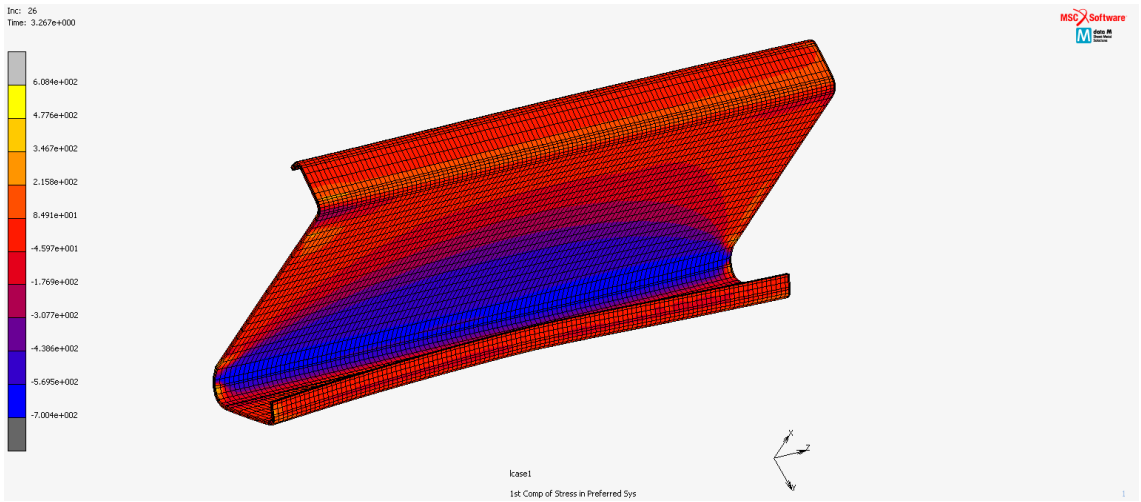


(b) Compressive stresses in increment 51.

Figure 4.29: Stresses in the inner corner of the Z-section profile for an applied load of 9 kN in the top surface.



(a) Tensile stresses in the outter corner.



(b) Compressive stresses in the inner corner.

Figure 4.30: Stresses for an applied load of 9 kN in the bottom surface of the Z-section profile.

Comparing the results between the simluation with isotropic hardening with the one with kinematic hardening, it is possible to verify that the material behaviour did not show considerable differences. Kinematic hardening resulted in slightly lower values for stresses. However, Martins [2018] identified the critical node as being the 5^{th} one in path w and for this simulation although the critical node is still located in path w it is not the 5^{th} but rather the 3^{rd} node. Resulting stresses history for every node can be examined in Appendix 1, figures 4.31-4.36 show the results for the critical node as well as a comparison to the results previously obtained with isotropic hardening.

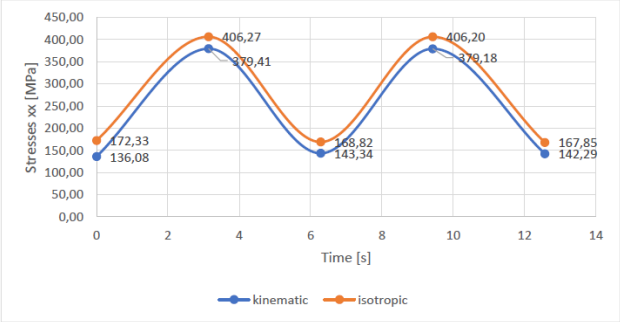


Figure 4.31: Comparison of stresses in xx direction for an applied load of 2 kN in the top surface for the critical node between isotropic and kinematic hardening.

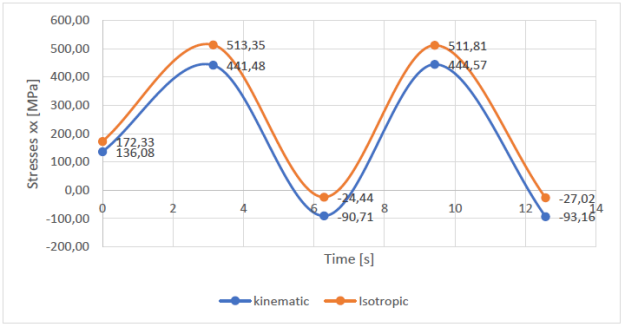


Figure 4.32: Comparison of stresses in xx direction for an applied load of 4,5 kN in the top surface for the critical node between isotropic and kinematic hardening.

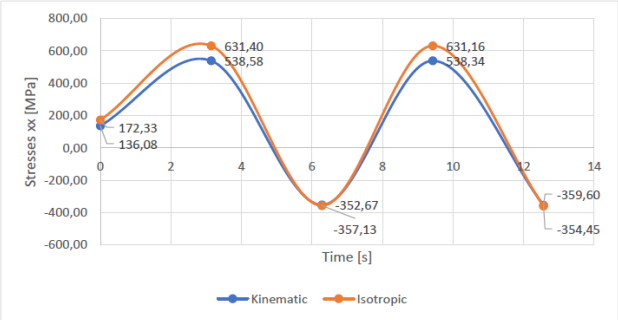


Figure 4.33: Comparison of stresses in xx direction for an applied load of 9 kN in the top surface for the critical node between isotropic and kinematic hardening.

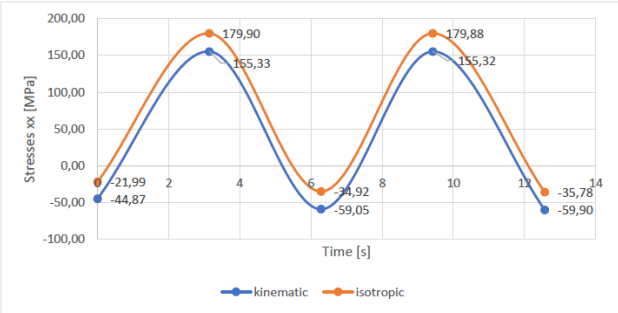


Figure 4.34: Comparison of stresses in xx direction for an applied load of 2 kN in the bottom surface for the critical node between isotropic and kinematic hardening.

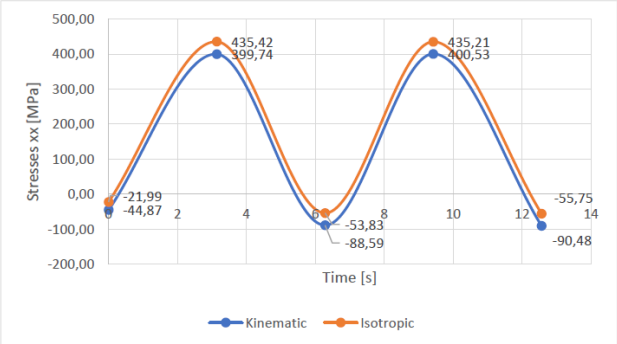


Figure 4.35: Comparison of stresses in xx direction for an applied load of 4.5 kN in the bottom surface for the critical node between isotropic and kinematic hardening.

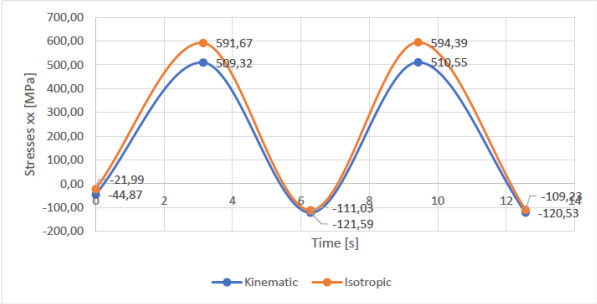


Figure 4.36: Comparison of stresses in xx direction for an applied load of 9 kN in the bottom surface for the critical node between isotropic and kinematic hardening.

The similarity of both stress-time histories seems to be justified by the fact that the load case does not cover reversed plasticity. After the application of mechanical loads, stresses in the corner differ from the ones in the initial state. This proves the existence of an elastoplastic effect of the material in the first cycle of the load. For the case of an elastic model, return to the original state should be observed. Values of stresses in the critical node were used for fatigue life estimation.

A local stress-based approach was used to estimate fatigue life of the profile. Parameters σ_m, $\Delta\sigma$ and N_f were calculated taking into account stress ranges from increments 76 and 100 and fatigue parameters σ'_f and b are the ones presented in table 2.1 obtained by Jesus et al. [2012] experimental fatigue tests on smooth specimens of S355 mild steel. The number of cycles until failure was estimated using Eq. 2.10 that takes into account the effects of mean stresses. The parameters values calculated for loads applies in top and bottom surfaces, can be seen in tables 4.2 and 4.3, respectively.

Table 4.2: Estimated number of cycles for three different cyclic loads applied in the top surface of the large flange of the Z-section profile using the local S-N based approach.

Load	σ_{max}	σ_{min}	σ_m	$\Delta\sigma$	N_f
2 kN	379,18	142,29	260,77	236,89	2,0E+08
4,5 kN	444,57	-93,16	175,70	537,73	7,5E+04
9 kN	538,34	-354,45	91,94	892,78	8,0E+02

Figure 4.37 shows the approximate linearity in log-log scales between the applied load

Table 4.3: Estimated number of cycles for three different cyclic loads applied in the bottom surface of the large flange of the Z-section profile using the local S-N based approach.

Load	σ_{max}	σ_{min}	σ_m	$\Delta\sigma$	N_f
2 kN	155,32	-59,90	47,71	215,23	1,2E+10
4,5 kN	400,53	-90,48	155,02	491,00	2,8E+05
9 kN	510,55	-120,53	195,01	631,08	9,3E+03

and the number of cycles until failure obtained from three points that correspond to the three applied loads. For loads applies in the top surface of the large flange, the number os cycles until failure is lower when compared with loads applied in the top surface.

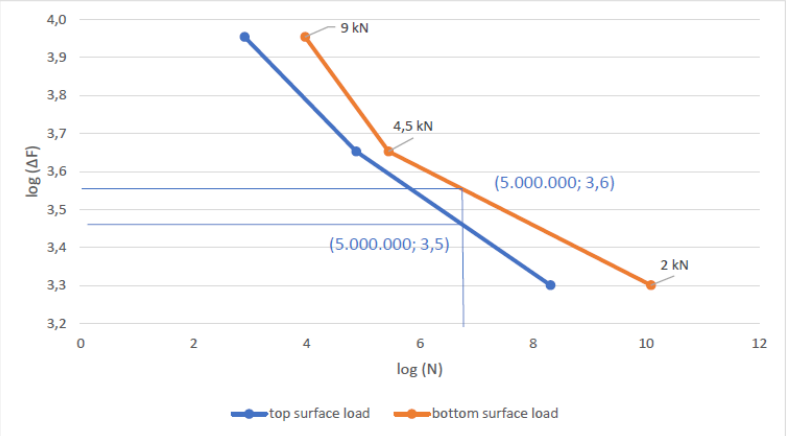


Figure 4.37: Number of cycles for maximum loads of 2 kN, 4,5 kN and 9 kN in a logarithmic scale, for simulations with kinematic hardening.

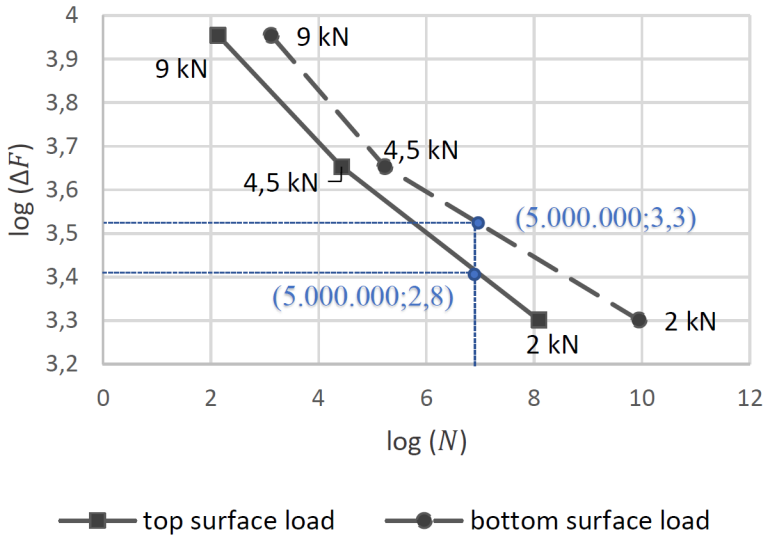


Figure 4.38: Number of cycles for maximum loads of 2 kN, 4,5 kN and 9 kN in a logarithmic scale, for simulations with isotropic hardening [Martins, 2018].

For fatigue strength curves with a slope $m = 3$, the number os cycles for which the structure is considered to have an inifinite life is 5 million according to EN 1993-1-9 (2005). Considering the same 5 million cycles for the studied profile, the maximum load that can be applied without compromising the structure is 3,5 kN for loads applied in top surface and 3,6 kN for loads applied in the bottom surface. Martins [2018] obtained different values with an isotropic hardening (see figure 4.38), she estimated that for 5 million cycles, the maximum load applied for the top surface would have to be 2,8 kN and 3,3 kN for the bottom surface.

Chapter 5

Conclusion

5.1 Conclusions

The growth of the Logistic Industry and its use of thin-walled cold formed steel sections in Racking & Shelving systems increased the requirements in performance of these structures. On the other hand, a lack of fatigue design rules in EN1993-1-9 regarding these steel structures generates uncertainty concerning fatigue failure. In order to fulfill the lack of design rules for cold rolled formed steel members, the FASTCOLD project proposes an extense set of tasks and investigations.

The structure analysed in the FASTCOLD project is a Z-section profile that is used as a rail for the passage of shuttles in the Logistic Industry. To accomplish the goals of the project, it is important to analyse the impact of applied external mechanical cyclic loads on stress range variations in the studied profile. Numerical simulations are nowadays an important tool to investigate the behaviour of materials and is important to optimize the numerical models in order to produce truthful information. Experimental tests are a great way to improve and validate the models.

Through the experimental and numerical work performed it was possible to draw the following conclusions:

- the material used in Z rail profiles production (S355MC) revealed stress-strain curves with a yield plateau and material anisotropy: specimens extracted from a direction transversal to the movement of the strip during the roll forming process presented higher yield strength but lower ductibility than specimens extracted from a longitudinal direction;

- the analysis performed to the microstructure analysis of the material from Z rails revealed that the outer surface corners present poor quality when compared to the inner corner surfaces. It would be advisable to further investigate the state of the profile surface in those critical areas after the roll forming process;

- LVDT and GOM analysis performed to the geometry of the profiles presented results in the same order of magnitude, differences in the results may be mainly due to the difference in lengths analysed in the two methods;

- the roll forming process leads to three-dimensional distortions on the profile. The distortions measured through experimental methods revealed that the numerical models tend to overestimate the geometric defects induced during the roll forming process; it is advisable to use a more refined mesh that could lead to better results and simulations with the actual roll-forming machine are mandatory;

- the use of kinematic hardening rule instead of an isotropic one, did not have significant impact on the residual stresses measured after the roll forming process, something expected since the roll-forming configures a monotonic loading type for which both hardening rules should provide same results;
- Edge position of the large flange, longitudinal bow and springback presented differences when a comparison to the results of the simulation using isotropic or kinematic hardening is done;
- Fatigue analysis revealed that the bend surface represents the critical area, a prediction verified by experimental tests conducted in the rail profile by partners of the FASTCOLD project;
- The number of cycles until failure estimated for an applied of 9 kN were 800 and 9300 for loads applied in the top and bottom surface, respectively;
- Regarding infinite life of components, the use of kinematic hardening rule led to higher values of allowed maximum loads (3,6 kN for the loads applied in the bottom surface and 3,5 kN for loads applied in the top surface) than the use of isotropic hardening (3,3 kN for the loads applied in the bottom surface and 2,8 kN for loads applied in the top surface).

5.2 Future Work

FASTCOLD project has a great extent of proposed goals and tasks, recommendations for future investigation and work are listed below:

- Design the COPRA RF model with information about the roll forming machine;
- Perform the simulations using S355MC steel;
- Design a model with a strip length after end cut of 1200 mm;
- Use a friction coefficient and study its impact on the results;
- Conduct a new analysis to the microstructure of the material using a non-invasive methology such as scan electron microscopy;
- Use a more refined mesh to simulate the roll forming process and explore the usage of an anisotropic plasticity model such as Hill's criterion.

References

(2010). Development of new 3d roll forming applications by means of numerical analysis as a part of a quality control methodology. *CBM Metal Matters*, 18:21–24.

(2018). Industrial validation of strain in cold roll forming of uhss. *Procedia Manufacturing*, 15:788–795.

Abeyrathna, B. N. (2014). *In-line shape compensation for roll forming through process parameter monitoring*. Deakin University.

Abvabi, A., Mendiguren, J., Rolfe, B., and Weiss, M. (2014). Springback investigation in roll forming of a v-section. *Applied Mechanics and Materials*, 553:643 – 648.

Abvabi, A., Rolfe, B., Hodgson, P., and Weiss, M. (2015). The influence of residual stress on a roll forming process. *International Journal of Mechanical Sciences*, 101-102:124 – 136.

Aceally (2018). *https://www.aceshelving.com/radio-shuttle-racking/radio-shuttle-racking-pallet-storage-system.html*. Aceally Racking Systems.

Amouzegar, H., Schafer, B., and Tootkaboni, M. (2016). An incremental numerical method for calculation of residual stresses and strains in cold-formed steel membes. *Thin-Walled Structures*, 106:61 – 74.

Basquin, O. H. (1910). *The exponential Law of Endurance Tests*. American Society for Testing and Materials Proceedings.

Bhat, S. and Patibandla, R. (2011). Metal fatigue and basic theoretical models: A review. *Alloy Steel: Properties and Use*.

Boardman, B. (1990). Fatigue resistance of steels. *ASM International*, 1:673 – 678.

Coffin, L. *A Study of the Effects of the Cyclic Thermal Stress on a Ductile Metal*. The American Society of Mechanical Engineers Journal.

DataM (2018). *http://www.datam.de/en/products-solutions/simulation-with-fea/copraR-fea-rf/*. DataM Products & Solutions.

Ellyin, F. (1997). *Fatigue Damage, Crack Growth and Life Prediction*. Champan & Hall, 2 - 6 Boundary Row, London SE1 8HN, UK.

FASTCOLD (2018). *https://fastcold-rfcs.com/*. FASTCOLD Home.

Ferreira, P. B. (2016). *Roll Forming - a study on machine deflection by means of experimental analysis and numerical developments*. Faculdade de Engenharia da Universidade do Porto.

Güner, A. (2007). *Assessment of roll-formed products including the cold forming effects*. The Graduate School of Natural and Applied Sciences of Middle East Technical University.

Gustavsson, A., Larsson, M., and Melander, A. (1997). Fatigue life of pressed steel sheet components. *Int. J. Fatigue*, 19(8-9):613–619.

Halmos, G. T. (2006). *Roll Forming Handbook*. Taylor Francis Group, Boca Raton, Florida.

Jesus, A. M., Matos, R., Fontoura, B. F., and Rebelo, C. (2012). A comparison of the fatigue behavior between s355 and s690 steel grades. *Journal of Constructional Steel Research*, 79:140–150.

Kato, B. and Aoki, H. (1978). Residual stresses in cold-formed tubes. *The Journal of Strain Analysis for Engineering Design*, 13(4).

Klippstein, K. (1980). Fatigue behavior of sheet-steel fabrication details. *International Specialty Conference on Cold-Formed Steel Strcutres*, 5th.

LaBoube, R. A. and wen Yu, W. (1999). Design of cold-formed steel structural members and connections for cyclic loading (fatigue). *Center for Cold-Formed Steel Strcutres Library*.

Löhe, D., Lang, K., and Vöhringer, O. (2002). *Handbook of residual stress and deformation of steel*. ASM International.

Lindgren, M. (2009). *Experimental and Computational Investigation of the Roll Forming Process*. Lulea University of Technology.

Ma, J.-L., Chan, T.-M., and Young, B. (2015). Material properties and residual stresses of cold-formed high strength steel hollow sections. *Journal of Constructional Steel Research*, 109:152 – 165.

Manson, S. (1954). *Behaviour of Materials under Conditions of Thermal Stress*. NACA TN-2933. USA: National Advisory Committee for Aeronautics.

Martins, A. (2018). *Simulation of cold rolling process of steel profiles for shelter applications*. Faculdade de Engenharia da Universidade do Porto.

Miner, M. (1990). Cumulative damage in fatigue. *Journal of Applied Mechanics*, 67:A159–A164.

Moen, C. D., Igusa, T., and Schafer, B. (2008). Prediction of residual stresses and strains in cold-formed steel members. *Thin-walled Structures*, 46:1274–1289.

Morrow, J. (1965). Cyclic plastic strain energy and fatigue of metals. *International Friction, Damping and Cyclic Plasticity, ASTM, STP*, 378:45–87.

Natal Jorge, R. and Dinis, L. (2004). *Teoria da Plasticidade*. Faculdade de Engenharia da U.PORTO, PORTO, 2004 edition.

Oñate, E. (2009). *Structural Analysis with the Finite Element Method - Linear Statics: Volume 1.* Springer.

Paris, P. C., Gomez, M. P., and Anderson, W. E. (1961). A rational analytic theory of fatigue. *Trend Engng.*, 13.

Pereira, H. F. S. G. (2006). *Comportamento à fadiga de componentes estruturais sob a acção de solicitações de amplitude variável.* Faculdade de Engenharia da Universidade do Porto.

Polyzois, D., Morris, G., and Hassan, S. K. (1994). Fatigue behavior of cold-formed steel sections. *Twelfth International Specialty Conference on Cold-Formed Steel Structures.*

Quach, W., Teng, J., and Chung, K. (2004). Residual stresses in steel sheets due to coiling and uncoiling: a closed-form analytical solution. *Engineering Structures*, 26:1249 – 1259.

Reddy, J. (1993). *An introduction to the finite element method.* McGraw-Hill, Inc.

Schafer, B. and Peköz, T. (1998). Computational modeling of cold-formed steel: characterizing geometric imperfections and residual stresses. *Journal of constructional steel research*, 47:193 – 210.

Smith, K., Topper, T., and Watson, P. (1970). A stress–strain function for the fatigue of metals (stress-strain function for metal fatigue including mean stress effect). *J Materials*, 5:767–778.

Stephens, R. I., Fatemi, A., Stephens, R. R., and Fuchs, H. O. (2001). *Metal Fatigue in Engineering.* John Wiley & Sons, Inc.

Tavares de Castro, P. M. (2017). *Apontamentos de Órgãos de Máquinas I.* Faculdade de Engenharia da U.PORTO, PORTO, 2017 edition.

Weng, C. and Pekoz, T. (1990). Residual stresses in cold-formed steel members. *Journal of Structural Engineering*, 166(6).

Appendix A

Appendix 1

Table A.1: Stresses [MPa] along the xx direction of the element coordinate system for the inner corner of the profile. Comparison between the initial state and results (in step 26 and 76) after application of 2 kN, 4,5 kN and 9 kN.

		Inner corner Step 26			Inner corner Step 76		
	Initial State	2 kN	4,5 kN	9 kN	2 kN	4,5 kN	9 kN
path x	-137,102	-151,39	-93,0299	38,6829	-151,345	-94,4717	39,6301
	-136,796	-151,867	-91,7225	35,1922	-151,818	-93,2291	36,1286
	-136,803	-152,51	-91,9945	33,5224	-152,46	-93,4623	34,5275
	-140,204	-152,942	-90,6364	33,7991	-152,89	-92,1252	34,8188
	-142,43	-154,626	-88,9332	36,7313	-154,571	-90,4314	37,748
path y	-8,41335	52,8105	126,924	239,653	287,28	127,34	243,14
	-8,40799	53,4693	128,852	239,719	288,29	129,226	243,533
	-8,50058	51,9211	129,674	240,032	285,534	130,09	243,857
	-3,95565	52,1062	131,733	240,972	285,484	132,151	244,449
	1,3014	53,9759	134,279	242,678	287,453	134,694	245,503
path z	102,727	287,473	354,26	471,368	52,7502	357,019	470,505
	100,506	288,488	354,569	471,933	53,409	357,378	470,928
	102,631	285,73	355,983	472,172	51,8621	358,768	471,153
	115,197	285,678	358,246	472,381	52,0478	361,004	471,492
	130,463	287,647	360,301	472,649	53,9184	363,071	471,981
path w	139,233	380,081	444,592	538,992	379,867	447,537	538,762
	134,715	382,354	442,92	539,072	382,134	446,025	538,795
	136,076	379,41	441,479	538,575	379,18	444,566	538,335
	143,323	376,204	441,178	538,523	375,975	444,331	538,292
	163,016	378,04	441,835	539,574	377,817	444,993	539,373

Table A.2: Stresses [MPa] along the xx direction of the element coordinate system for the inner corner of the profile. Comparison between the initial state and results (in step 51 and 100) after application of 2 kN, 4,5 kN and 9 kN.

		Inner corner Step 51			Inner corner Step 100		
	Initial State	2 kN	4,5 kN	9 kN	2 kN	4,5 kN	9 kN
path x	-137,102	-139,137	-65,7107	93,1674	-35,8457	-65,2483	-351,518
	-136,796	-139,73	-64,6787	89,5603	-36,1488	-64,2287	-353,871
	-136,803	-140,519	-65,2746	87,3669	-38,169	-64,8015	-354,448
	-140,204	-141,148	-64,4015	86,7903	-37,9672	-63,9316	-351,196
	-142,43	-143,038	-63,1779	88,6692	-35,5977	-62,7135	-344,021
path y	-8,41335	-35,4454	-72,8791	-84,0451	-35,8457	-73,5553	-269,945
	-8,40799	-35,744	-72,877	-85,1229	-36,1488	-73,5979	-272,57
	-8,50058	-37,7636	-72,9573	-85,7345	-38,169	-73,662	-272,346
	-3,95565	-37,5628	-70,8371	-85,551	-37,9672	-71,5328	-269,258
	1,3014	-35,1959	-67,2113	-84,2986	-35,5977	-67,9107	-263,74
path z	102,727	93,5354	-84,0612	-268,24	92,6594	-85,9882	-83,6055
	100,506	93,2664	-86,2399	-270,764	92,3817	-88,1714	-84,5056
	102,631	90,1403	-85,4108	-270,538	89,2556	-87,3511	-85,0986
	115,197	90,586	-81,9016	-267,552	89,7041	-83,8441	-85,073
	130,463	93,8228	-76,9736	-262,19	92,9463	-78,9027	-84,1075
path w	139,233	145,262	-85,3958	-349,718	144,222	-87,8312	93,7236
	134,715	146,536	-88,8555	-352,074	145,488	-91,2983	90,1128
	136,076	143,344	-90,7098	-352,668	142,293	-93,1616	87,963
	143,323	140,874	-89,14	-349,439	139,823	-91,5598	87,4073
	163,016	144,277	-84,8404	-342,331	143,232	-87,2399	89,2791

Table A.3: Stresses [MPa] along the xx direction of the element coordinate system for the outter corner of the profile. Comparison between the initial state and results (in step 26 and 76) after application of 2 kN, 4,5 kN and 9 kN.

		Outter corner Step 26			Outter corner Step 76		
	Initial State	2 kN	4,5 kN	9 kN	2 kN	4,5 kN	9 kN
path x	136,428	131,634	100,254	67,2548	131,634	98,8411	67,9359
	136,362	131,531	96,599	66,2725	131,531	95,4622	66,9515
	135,698	130,909	94,8284	65,988	130,909	93,7366	66,6666
	135,058	130,372	98,7802	65,8971	130,373	97,3304	66,5771
	137,303	132,738	105,573	66,5124	132,738	104,237	67,1949
path y	90,5149	158,745	233,94	212,966	158,744	233,999	212,846
	91,495	161,472	235,845	213,314	161,471	235,613	213,186
	89,8572	161,29	236,532	214,072	161,289	236,169	213,94
	86,0443	158,512	234,526	215,621	158,511	234,578	215,489
	78,9234	151,921	232,838	217,264	151,92	232,882	217,135
path z	51,7274	202,131	371,077	413,481	202,129	371,785	412,483
	48,2984	202,085	373,621	413,632	202,083	374,182	412,633
	49,0976	205,509	376,99	414,964	205,508	377,509	413,958
	44,6079	202,984	374,603	416,582	202,982	375,24	415,598
	24,4205	183,931	367,592	419,321	183,929	368,197	418,351
path w	-48,4715	145,329	387,899	510,087	145,326	388,794	511,09
	-48,4715	152,916	394,655	509,531	152,913	395,474	510,597
	-44,8667	155,327	399,737	509,323	155,324	400,525	510,55
	-45,4206	150,503	397,217	511,348	150,501	397,911	512,682
	-52,448	160,784	405,574	515,112	160,781	406,251	516,542

Table A.4: Stresses [MPa] along the xx direction of the element coordinate system for the outter corner of the profile. Comparison between the initial state and results (in step 51 and 100) after application of 2 kN, 4,5 kN and 9 kN.

		Outter corner Step 51			Outter corner Step 100		
	Initial State	2 kN	4,5 kN	9 kN	2 kN	4,5 kN	9 kN
path x	136,428	137,377	112,038	78,1355	137,406	111,916	78,8632
	136,362	137,224	108,522	76,75	137,253	108,41	77,4783
	135,698	136,476	106,518	76,0458	136,505	106,402	76,7747
	135,058	135,75	109,775	75,6162	135,778	109,622	76,3461
	137,303	137,916	116,246	75,8617	137,944	116,101	76,5914
path y	90,5149	84,6534	63,7541	-25,8931	84,368	63,0482	-25,2803
	91,495	86,6622	63,7235	-27,6492	86,3735	62,9635	-27,043
	89,8572	86,0033	63,1661	-28,2754	85,7122	62,3976	-27,6705
	86,0443	83,1154	61,2639	-27,1241	82,8239	60,5407	-26,5178
	78,9234	76,8732	60,4355	-24,3003	76,5834	59,7058	-23,6895
path z	51,7274	37,8454	-3,93512	-75,5853	37,2048	-5,47453	-74,9745
	48,2984	36,6866	-4,06024	-78,2693	36,0413	-5,6406	-77,6766
	49,0976	39,6373	-1,77379	-78,08	38,9902	-3,37913	-77,4935
	44,6079	37,1816	-3,86561	-76,145	36,5336	-5,44881	-75,5501
	24,4205	18,9362	-9,08029	-71,3185	18,2909	-10,6037	-70,7038
path w	-48,4715	-67,8512	-97,4912	-118,303	-68,6995	-99,3358	-117,274
	-48,4715	-61,2814	-93,181	-121,136	-62,1338	-95,048	-120,111
	-44,8667	-59,0484	-88,5885	-121,594	-59,9022	-90,4785	-120,527
	-45,4206	-63,4316	-90,1483	-118,44	-64,2825	-92,0531	-117,332
	-52,448	-52,1806	-79,6324	-112,001	-53,0249	-81,3703	-110,838